Development of improved metal matrix composite via the control of interface and matrix microstructure

Smith, Joel Edmund

Award date:
1995

Awarding institution:
University of Bath

DEVELOPMENT OF IMPROVED METAL MATRIX COMPOSITE VIA THE CONTROL OF INTERFACE AND MATRIX MICROSTRUCTURE

Submitted by Joel Edmund Smith

for the degree of PhD

of the University of Bath

1995

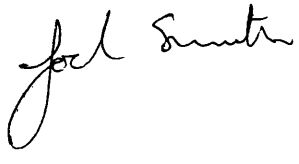

Joel Edmund Smith

ProQuest LLC
789 East Eisenhower Parkway
P.O. Box 1346
Ann Arbor, MI 48106-1346

SUMMARY

Literature has been reviewed on fibre reinforced metal matrix composites, with particular reference to aluminium and aluminium alloy based systems.

A liquid metal infiltration method has been used successfully for producing composites containing Altex and Nicalon fibres (volume fraction ~ 0.5) with less than 1% porosity. However, the method was unsuccessful for Sigma reinforced composites due to problems with the removal of a polymeric tape binder and difficulties in producing preforms.

Two aluminium alloys have been investigated as the matrix material, A201 (4 wt.% Cu-0.3 wt.% Mg-0.7 wt.% Ag) and ARE415 (4 wt.% Cu -1 wt.% Mg-0.5 wt.% Ag). The cast composites were cored and showed interdendritic $CuAl_2$ segregating to the surface of the fibres. During the infiltration stage magnesium was found to have diffused into surface regions of the fibres.

The solution treatment reduced further the level of magnesium in both matrices as a consequence of diffusion into the fibres. For both matrices solution treatment was effective for the Altex composites but not for the Nicalon composites, where silicon containing intermetallic phases were present in the matrix. The Nicalon composites showed, additionally, reaction in the outer 200nm of the fibre which led to the formation of needles of aluminium carbide, Al_4C_3. This is attributed to reaction with the silicon oxycarbide constituent of the fibre.

ARE415 alloy based composites formed widespread porosity on solutionising due to the release of hydrogen gas from the matrix. This prohibited further use of the alloy for composite fabrication and therefore only A201 matrix composites were studied further.

The presence of fibres caused an accelerated ageing response in the composites compared with unreinforced A201 alloy due to the high dislocation density in the composites. The depletion of magnesium from the matrix resulted in θ' precipitates forming instead of the desired Ω precipitates. The precipitates in the composites over-aged faster than those in unreinforced alloy.

Mechanical properties for the composites were measured by tensile testing in directions parallel to (longitudinal) and normal to (transverse) the fibres. The chemical reaction at the fibre/matrix interface led to the development of a strong interfacial bond for both Altex and Nicalon composites. Thus the measured longitudinal modulus was in accordance with 'rule-of-mixtures' (ROM) calculations. However the measured transverse modulus was lower than ROM calculations, being governed by the presence of voids and the touching of fibres.

Longitudinal stress-strain curves from the composites showed the development of a knee-point which was consistent with the onset of yielding in the matrix. The yield strengths of all composites were lower than the respective unreinforced alloys. This may be attributed to two factors. Firstly the effects of residual stress which were tensile in the longitudinal direction. Secondly in the peak-aged condition the composite contained θ' precipitates which produce a lower hardening response than the Ω precipitates present in the unreinforced alloy. The longitudinal strengths fell below ROM calculations. This was considered to be a combination of low fibre strength and a lack of resistance to crack propagation owing to a strong interfacial bond and low matrix ductility. The transverse strength was also low, being governed by the presence of voids and touching fibres.

ACKNOWLEDGEMENTS

I would like to thank Professor V. D. Scott and Mr. M. G. Phillips for their guidance and supervision, all of the technical staff, particularly Mr. M. Devon for his assistance with specimen preparation and Mr. H. Perrott and Dr. G. Love for their help with electron microscopy.

I would also like to thank the other members of the MMC group including Dr. R. Bushby, Dr. A. Chen, Dr. J. O'Rourke, Dr. K. Hicks and Dr. S. Bleay for their continual assistance.

I thank the EPSRC and DRA for their financial support.

Finally I would like to thank my family and friends.

CONTENTS

1.0 INTRODUCTION

This literature review covers metal matrix composites (MMCs), focusing particularly on unidirectional continuous fibre composites. First the need for MMCs is demonstrated and some applications are presented. The roles of the constituent materials and some examples are then described, followed by a summary of the different composite fabrication routes. The characteristics of the fibre/matrix interface and the factors determining the mechanical properties are then considered. The review concludes by stating the aims of this investigation and the proposed programme of work.

1.1 Composite Materials

As many traditional materials fail to meet the performance demands of modern engineering applications and tougher legislation governing safety is introduced, attention is increasingly turning towards composite materials as a solution to an ever-broadening range of design problems. The term composite encompasses a wide range of materials including: glass reinforced plastics (GRPs), steel reinforced concrete, metal matrix composites and ceramic matrix composites (CMCs) and even wood.

In simple terms a composite material can be considered as a combination of two or more materials, which takes advantage of the more favourable properties of the materials whilst moderating the less desirable properties. Generally a reinforcing phase is distributed throughout a matrix phase. The reinforcing phase can be particles, whiskers, short fibres or continuous fibres, and is commonly ceramic, whilst the matrix phase is usually a polymer, ceramic or metal. The microstructure of the composite and hence its mechanical properties, are governed by the nature of the reinforcement, the matrix, and the interface between them. The principles of composite properties are largely derived from a 'rule-of-mixtures' approach which will be described in a later section.

Whilst the reinforcement confers stiffness and strength, the matrix plays many important roles in a composite. It acts to transfer stress into the reinforcing fibres; it provides protection for the reinforcement against abrasive damage and environmental attack; it confers a degree of toughness to an otherwise brittle fibre and provides resistance to shear and compressive forces where the fibre alone is capable of only sustaining tensile loads. In the case of unidirectional continuous fibre reinforced composites, the matrix dominates all off-axis properties.

Composite materials are competitively placed with regards to more common engineering materials, this is highlighted in Figure 1.1, which shows a material selection chart of Young's modulus, E, versus density, ρ. The criterion for the lightest beam of requisite stiffness is given by the material with the greatest value of $E^{1/2}/\rho$.

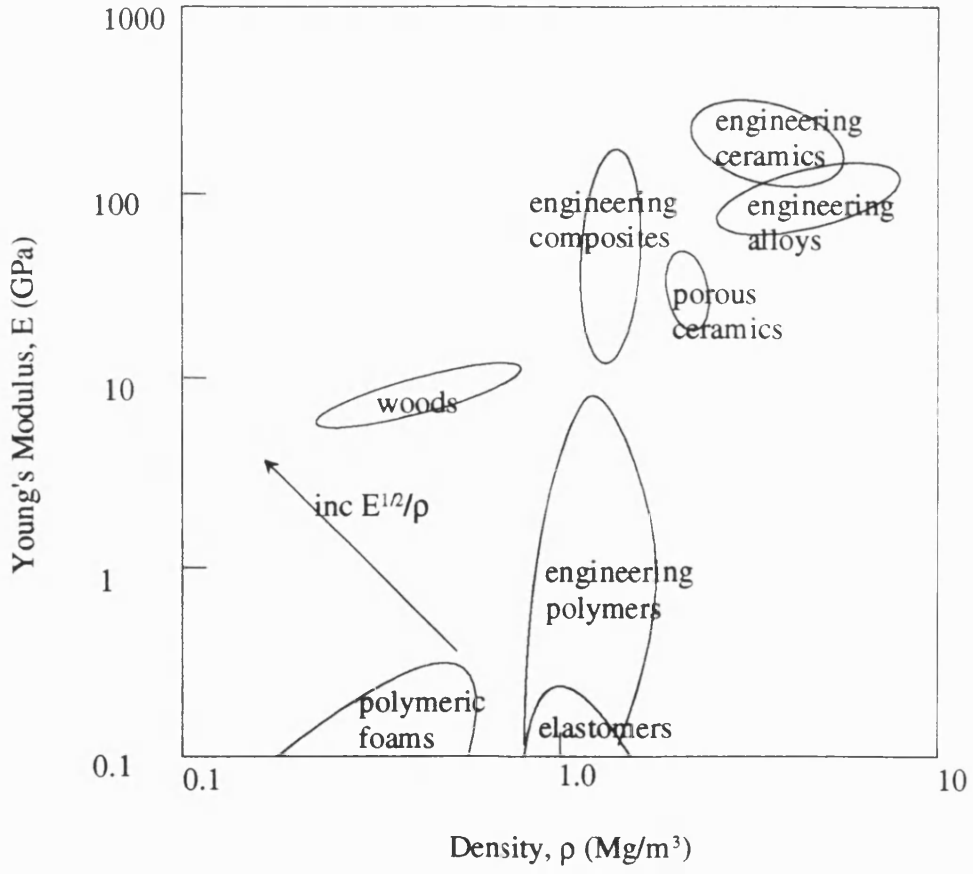

Figure 1.1 Modulus versus density performance chart. After Ashby [1].

Reinforced plastics have long been established in the field of composites. They have good physical properties, mouldability, high specific strength and are cost effective. In many respects they are almost ideal and it might be argued that little is gained when switching from polymer to metal matrix composites. However, metal matrix composites come into their own in higher service temperature applications and in hazardous environments. In these cases high coefficient of thermal expansion, dimensional instability, low thermal conductivity and sensitivity to hygrothermal and radiation degradation of resins mean that metal matrix composites are significantly better than polymer matrix composites.

1.2 Metal Matrix Composites

Metal matrix composites can be classified into three distinct types according to the reinforcement used, particulate reinforced, short fibre or whisker and continuous fibre or sheet reinforced. Discontinuously-reinforced MMCs (particulate, whisker and short fibre) are less expensive than continuous fibre reinforced composites and can be fabricated by conventional metallurgical methods, but continuous fibre reinforced composites offer the greatest potential for increases in strength and stiffness.

The applications for MMCs are widespread [2-5] and generally depend upon financial constraints and reinforcement type. In the automotive industry MMCs are used for connecting rods, driveshafts and piston crowns. In aerospace they find use as panels and long beams, waveguide booms on the Hubble telescope, electronic equipment racks in aircraft, high heat flux applications in rocket engine thrust chambers and in replacing toxic beryllium in the US Trident missiles. Electronic uses derive from properties such as; high thermal conductivity and dimensional stability and applications include cores, substrates, carriers, housings and heat sinks. Filamentary super-conductors (Nb-Ti/Cu matrix) can be used for high energy physics applications such as particle accelerators (they also offer the potential for magnetically levitated train projects of the future). Other applications cover; power semiconductor devices,

military tank tracks and torpedo hulls, golf clubs and racing bikes. The current market for MMCs is quoted as $40 million each for, the US, Europe and Japan with an expected 12-15% market growth rate per annum over the next 5 years [6].

1.3 The Fibre Reinforcement

The determining factors in selection of reinforcement are application and cost, the advantages and disadvantages of each having been widely documented [7-12]. In general particulate materials are used when weight saving and wear resistance are required, whilst fibres are used where stiffness and strength are important.

Fibres can be incorporated into the matrix to form a series of directional laminae, the orientation of which strongly influences the properties. The greatest improvements in strength are achieved using unidirectional continuous fibre composites, and it is this class of MMC with which this report is concerned. This section covers the manufacture and properties of the fibres utilised in this project.

In the fibrous form a material approaches its theoretical shear strength. This can be attributed to one or more of the following [13]:

a reduced concentration of critical flaws with respect to the bulk material,

a very fine microstructure developed due to the manufacturing process,

the development of crystallographic or molecular texture,

high internal stresses in the structure.

Fibrous materials also exhibit enhanced stiffness, and a distinct anisotropy.

Various fibre types are available and their properties are summarised in Table1.1. Ceramic fibres [14] are the most widely used in MMCs. In conjunction with improved strength and stiffness, fibres can impart enhanced fatigue resistance as well as improved high temperature performance. However, any high temperature application may result in mechanical properties being degraded by a fibre/matrix reaction.

The effectiveness of a fibre as a reinforcement is therefore governed by three key factors: longitudinal fibre tensile strength, σ_f, Young's modulus parallel to the fibre axis, E_f, and the fibre/matrix interfacial shear strength, τ_i.

Table 1.1 Mechanical properties of various reinforcing fibres [15]

Fibre type	Tensile strength (GPa)	Young's modulus (GPa)
Glass	3.5-4.0	70-90
Carbon	2.1-2.7	230-830
Polymeric	2.7	90-120
Ceramic	3.0-3.5	200-450

1.3.1 Fibre Fabrication Methods

There are two common methods for the fabrication of continuous ceramic fibres [13, 15, 16]

1.3.1 (a) Chemical Vapour Deposition

This involves the decomposition of a gaseous compound onto a heated core fibre. The core fibre is commonly tungsten or carbon (as used in BP Sigma fibre and Textron SCS fibre respectively). This method of production can be used for boron and silicon carbide fibres. The technique produces fibres of the order of 100μm diameter or greater, referred to as monofilaments. The process is also suitable for the deposition of a surface layer or coating to modify the fibre behaviour, and thereby aid matrix compatibility and interface strength.

1.3.1 (b) Melt Spinning of an Organic Precursor

This technique can be used to produce fibres of 10 - 20 μm diameter, and is used by Nippon Carbon in the formation of their Nicalon fibre [17]. An organic precursor,

generally a polymer, is melt spun, to give a continuous fibre. This is then given a post spinning treatment, i.e. pyrolysis or calcination, to give the ceramic form.

For the best mechanical properties in load-bearing applications, ceramic fibres require a combination of high purity, high density, low porosity and small grain size.

1.3.2 Fibres & Monofilament Used in the Study

The fibres most commonly used in MMCs are alumina, and silicon carbide. Carbon fibres are also used due to excellent strength and modulus, but their high cost precludes them from most uses. The following three commercial fibres were utilised in this project.

1.3.2 (a) Altex (Sumitomo Chemicals, Japan)

Altex is a continuous 10-15μm diameter polycrystalline aluminosilicate fibre of nominal composition 85 wt.% Al_2O_3, 15 wt.% SiO_2, and <0.05 wt.% impurity [18]. It consists of 10nm γ-alumina crystallites and has a tensile strength of 1.8 GPa and a Young's modulus of 210 GPa.

1.3.2 (b) Nicalon (Nippon Carbon, Japan)

Nicalon is a continuous fibre of ≈ 13 μm diameter [17]. This fibre has been extensively characterised [17, 19-34] and the results of Bleay et al are summarised here. Although considered to be a silicon carbide fibre, the fibre also incorporates silicon oxycarbide and free carbon. Electron-probe microanalysis (EPMA) has suggested the composition to be 54.9 wt.% silicon, 32.1 wt.% carbon, and 11.6 wt.% oxygen, giving 46 vol.% SiC, 34 vol.% $SiOC_{0.5}$ and 20 vol.% C_{free}. SiC exists substantially in the form of β microcrystallites of several nanometres in diameter. Much of the fibre is, however, amorphous and a fine amorphous network surrounds the SiC microcrystallites. The oxycarbide is considered to make up most of the amorphous phase. The stoichiometry of this oxycarbide layer is considered to change such that the O:C ratio is increased

towards the fibre surface, promoting a 200 nm layer of oxygen enrichment. The fibre has a reported strength and modulus of 2.8 GPa and 200 GPa respectively [13].

1.3.2 (c) Sigma (B.P. Metal Composites Ltd., United Kingdom)

Sigma fibre is manufactured by BP Research, and is a continuous monofilament of 100μm diameter consisting of silicon carbide deposited by CVD onto a tungsten core. The fibre is available uncoated, or with a carbon or carbon-titanium boride coating. The coating is designed to increase the fibre strength and reduce the strength variation, reduce abrasive damage during handling, and act as a compliant layer isolating the SiC from embrittling reaction products [35] The carbon/titanium-diboride coated fibre has an ultimate tensile strength of 3.75 GPa and a Young's modulus of 400 GPa.

1.4 The Metal Matrix

The metals listed below offer the best rewards for use as matrix materials, the choice generally being governed by cost and availability.

1.4.1 Metals

Magnesium and its alloys are very light and offer excellent potential for weight savings, $\rho = 1740\ Kgm^{-3}$. They have already found use in aerospace structures where exposure to temperatures of up to 500°C may arise. A disadvantage is that magnesium is difficult to form at room temperature.

Titanium is one of the most important aerospace materials. It has a low density, $4540\ Kgm^{-3}$, high specific strength and modulus, good corrosion resistance and excellent oxidation resistance. It also has a high melting point, 1672°C.

Copper is an excellent electrical conductor and has good thermal conductivity. It has high strength and can be cast and worked easily. It is used as the matrix for niobium-based superconductors.

Aluminium alloys have a low density, 2800 Kgm^{-3}, and good strength and corrosion resistance. They have a market share of 65-70% (in composites), mainly due to availability, cost, and the wide range of properties for its alloys (e.g. castability, corrosion resistance, heat-treatable). Of particular importance are the precipitation hardening alloys, some of which will now be addressed.

1.4.2 Aluminium Alloys

Aluminium alloys are classified according to alloying elements and wrought or cast state [36], over the years a number of these have been investigated as matrix alloys, some of which are now described. Aluminium itself has good casting properties but a low strength, aluminium silicon alloys are also common matrix materials as they show excellent castability. Silicon in particular is added as it gives a high fluidity and low shrinkage [37]. These alloys do not exhibit an age-hardening response and so magnesium is often added to promote this, but its effects often disappear since the small amount of magnesium is removed due to the presence of the reinforcement. This may lead to the use of a specific age-hardening alloy such as 6061, which gives a good precipitation response (more magnesium than Al-Si alloys, and therefore still precipitation hardens) and infiltration [38]. Another series of age-hardening alloy widely researched are the 2000 series of copper-containing alloys (2014, 2024 etc.), one system which has received considerable attention in recent years is the Al-Cu-Mg-Ag alloy [39-53]. This has the nominal composition 4 wt.% Cu, 1 wt.% Mg and 0.5 wt.% Ag (similar to the Avior alloy, A201 US standard) and it is claimed to have high tensile strength (up to 500MPa), good castability, a substantial age-hardening response with good long-term stability at elevated temperature.

1.5 Composite Fabrication

There are two different fabrication routes employed in the manufacture of MMCs [9, 10, 54], solid state processing and liquid state processing. This section gives a

summary of some of the different manufacturing routes and highlights the important technique of liquid metal infiltration.

The choice of fabrication route for MMCs depends on the combination of matrix and fibre selected. Fibres are often coated prior to incorporation into the matrix. This is done for a number of reasons: to prevent degradation of fibre strength and stiffness, to increase the wettability of the fibre by the matrix and to aid compatibility (that is to reduce the chance of a fibre matrix reaction). The fibres can then be preformed into sheets or tapes, often held together by a polymeric binder.

1.5.1 Solid State Methods

Solid state processing involves the consolidation of metal sheets or powders, usually at an elevated temperature.

1.5.1 (a) Diffusion Bonding

This involves the consolidation of preformed materials, by the interdiffusion of atoms from metal surfaces in contact at elevated temperature [55]. The basic steps are, apply metal foils to the reinforcement, cut to shape, lay up plies in desired orientation, vacuum encapsulate, heat to fabrication temperature, apply pressure and hold for consolidation cycle, cool, remove and clean. The advantages of this method are that a variety of metals may be used, and control of volume fraction of reinforcement and its orientation are obtained. The disadvantages include: a processing time of several hours, the cost of high temperature and pressure, possible fibre damage due to the high pressure, limitations in component size, and the requirement of clean surfaces for interdiffusion.

1.5.1 (b) Hot Isostatic Pressing

In this method the composite is sealed in a can, and then an applied gas pressure pushes against the can to consolidate. The high pressures and temperatures (200 MPa

and 2200°C) used may cause fibre damage or reaction, but a variety of geometries can be formed.

1.5.1 (c) Powder Processing

First the reinforcement and matrix are mixed to give a homogeneous distribution. The mixture is then cold pressed to give a green body, which is subsequently canned and degassed. The can is then hot pressed (uniaxial or isostatic) below or above the matrix alloy solidus.

1.5.2 Liquid State Methods

Liquid state fabrication [9, 56-58] has the obvious advantage over solid state processing in that complex components can be formed to near net shape. This is highly attractive for MMCs where post machining is expensive (high tool wear rates), time consuming and can induce reinforcement damage. The process is also easily automated to provide high production rates. The main fabrication methods are liquid metal infiltration (LMI) and stir casting (also known as rheo or compocasting).

1.5.2 (a) Stir Casting

The reinforcement is incorporated into a molten alloy mixture and then vigorously agitated and allowed to solidify. This method can result in excessive fibre damage, and is only suitable for particulate or short fibre composites.

1.5.2 (b) Infiltration Under Inert Gas Pressure

In this method the reinforcement is infiltrated by molten metal under gravity and an applied inert gas pressure. To avoid oxidation infiltration may be performed under a vacuum. This also gives better wetting. Yang and Chung [59] report using a pressure of 17 MPa and a temperature of 720°C, this gives less preform compression. They report the disadvantage of low cooling rates which may enhance grain growth and possibly interfacial reaction.

Although this method is suitable for producing complex parts to a high standard, the high temperature employed may cause an adverse reaction between the fibre and the matrix, resulting in the segregation of brittle intermetallics around the fibres, and a reduction in strength. There are also problems with the wetting of the fibre by molten alloys. Some of these problems may be reduced by the application of a coating to the fibre. Low pressures are used with these methods and so the risk of fibre damage is reduced compared with solid state processing.

1.5.2 (c) Liquid Metal Infiltration

This method, similar to the squeeze-casting technique, is long established in industry for producing alloy components, where its advantages over traditional casting techniques are the reduction of porosity, shrinkage, hot tearing and residual stress. The process also produces near net shape components. Short fibre and particle-reinforced composites have been produced by this method [6, 60, 61], but there is limited information on its use for making continuous fibre MMCs [62-64]. The technique has been widely documented [65-72], and has the following basic steps.

(1) The fibre preform is heated to several hundred °C, but below the melting point of the matrix metal.

(2) The preform is set in a preheated die (250 - 350°C).

(3) Molten alloy at a temperature, T_a, above the melting point, is squeezed into the preform by hydraulic pressure.

(4) The mixture is forced to solidify in a short time due to rapid heat transfer under pressure.

The critical processing variables are the alloy and preform temperatures, T_a and T_f, respectively. If they are too high, fibre degradation will result, leading to a low strength composite. If they are too low, problems with liquid metal flow will result in non-infiltrated areas. If the die is not preheated, too much solidification will arise on pouring.

The infiltration pressure is also vital, and must not exceed the strength of the preform, but a high enough pressure must be applied to allow complete infiltration. Typical pressures can be as high as 50-100MPa [65, 73]. The final squeeze pressure must be high enough to compensate for solidification shrinkage, and to provide a high coefficient of heat transfer at the molten metal/metal die interface. If the final pressure is too low, defects such as pinholes are likely to occur. The application of pressure is a way to improve the interface bonding for those fibres difficult to wet (molten aluminium is non wetting for many ceramics) and of rough surface.

The infiltration speed has no effect on the compressive or tensile strength of the composite, and is typically 1 - 5 cm/s [65]. The solidification time is a factor affecting the microstructure [74], short times lead to a greater dispersion of mechanical properties than longer times. Solidification is more rapid in reinforced areas than in unreinforced areas of a comparable thickness. Other factors to consider include wettability, direction of infiltration, alloy additions and external cooling. Failure to control the process can bring about oxide inclusions, porosity and segregation [66].

A fine equiaxed grain structure results in the matrix, due to undercooling below the equilibrium solidification temperature, and a rapid rate of heat extraction. The resulting alloy tensile strength is comparable to forgings. The advantages of LMI are near net shape, potential automation and high productivity, efficient use of raw materials, densification, heat transfer and a considerable improvement in properties when compared to hot pressing. The disadvantages can be fibre displacement, segregation, reactions between the matrix/fibre and or the binder/liquid metal (these should both be minimal due to short solidification times), as well as possible reinforcement damage due to the pressure.

A related process is vacuum squeeze casting [65, 75, 76]. The fibre preform includes a volume of air, which can be displaced without the turbulence experienced during

squeeze casting. The preform and cavity are evacuated, removing the air that may give porosity. Degassing the molten metal also prevents the evolution of gas on solidification. Vacuum squeeze casting results in an increased bending strength and less scatter, as inherent cavities formed during infiltration are decreased in size and number, by exhausting air prior to infiltration [65].

1.6 Characteristics of the Fibre/Matrix Interface

The interface is recognised as an important factor governing composite properties, and can be considered as a bounding surface between two phases (fibre and matrix). At this boundary is a discontinuity between some material properties, such as elastic and thermodynamic properties, which can lead to thermal stresses and chemical reactions. The interface is a high energy, incoherent site, and provides a rapid path for diffusion, it can also act as a site for heterogeneous nucleation or a precipitate free zone. This section discusses the types of bonding, thermal stresses and chemical reactions at the interface.

1.6.1 Bonding

For a composite there must be effective load transfer between the matrix and the reinforcement, the efficiency of which is dependent upon the quality of the interfacial bond between the fibre and the matrix. In general load transfer is improved with increasing bond strength, although this can reduce the toughness of the composite by decreasing the amount of fibre pull-out which occurs at failure. For load transfer to occur some bonding must exist, chemical, mechanical, thermal and structural factors must be considered.

1.6.1 (a) Mechanical Characteristics

Mechanical bonding is easily described as mechanical interlocking between the matrix and the fibre. This provides an effective contribution in the longitudinal direction, but only a minor effect in the transverse direction. In addition to rough surfaces,

mechanical keying may also be achieved by differential contraction. For example aluminium alloys have a coefficient of thermal expansion of 23.6 x 10^{-6} per °C, while ceramic reinforcements have a value in the range of 2-9 x 10^{-6} per °C. Thermal stresses result on cooling during processing [77, 78] due to this mismatch and can produce strains in the order of 1%. These may be large enough to exceed the yield stress of the matrix, causing plastic deformation, and a build up of dislocations and vacancies, which in turn may lead to faster ageing kinetics for an age-hardenable matrix.

A simple estimate for these residual stresses is given by Shetty [79] and Phillips [80].

$$\sigma_{axial} = \frac{E_f V_f (\alpha_m - \alpha_f)\Delta T}{1 + V_f\left(E_f / E_m - 1\right)}$$

$$\sigma_{radial} = \frac{E_m (\alpha_m - \alpha_f)\Delta T}{(1 + \upsilon_m)}$$

where α_m and α_f, are the coefficients of thermal expansion for the matrix and fibres respectively, ΔT, is the temperature change, and υ_m, the Poisson ratio of the matrix. Using Nicalon as an example, E_f = 200 GPa, E_m = 70 GPa, υ_m = 0.34, α_f = 4.5 x10^{-6} K^{-1}, α_m = 23.6 x$10^{-6}K^{-1}$, V_f = 0.5 (values of thermal expansion and Poisson ratio taken from Tennent [81]), and assuming ΔT = 200K, the following results are obtained. $\sigma_{axial} \approx$ 200 MPa, and $\sigma_{radial} \approx$ 200 MPa. Data from Brown [82] using x-ray diffraction on aluminium/graphite composites found a volume average longitudinal residual stress of 200 MPa. Further work using Raman microprobe analysis on aluminium quartz composites found a residual tensile strength of 250 - 350 MPa at the interface.

Using a simple two-element model the following stress distribution, Figure 1.2, can be obtained, where r, θ and z, refer to the radial, circumferential and axial directions respectively. Note that the axial stress remains constant, while the radial and circumferential stresses fall off away from the interface.

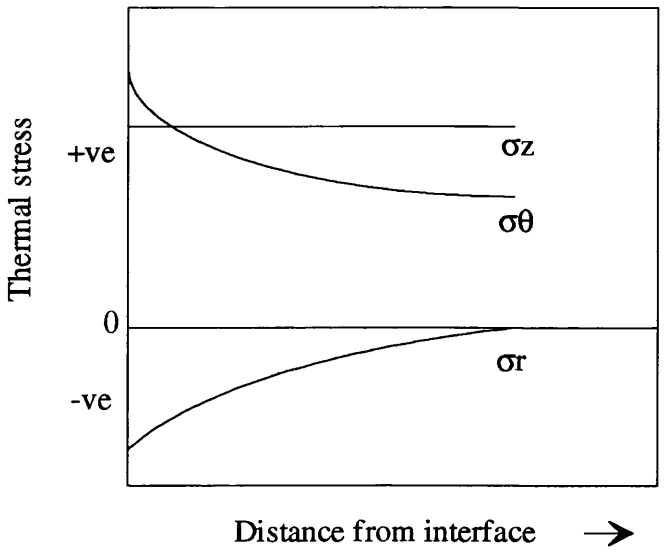

Figure 1.2 Schematic showing variation of residual stress away from interface. After Chawla [10].

1.6.1 (b) Chemical Characteristics

Ceramic reinforced metal matrix composites can be regarded as non-equilibrium systems, such that a chemical potential gradient exists across the fibre/matrix interface. Under certain conditions (high temperature for long times) this difference in potential provides a driving force for diffusion and/or chemical reaction to occur.

A diffusion bond results when there is no reaction, but mutual solubility between components, and providing there are no defects such as voids present, it can result in a good quality bond. For a chemical reaction bond, the matrix and fibres react to form a new compound at the interface, termed a reaction zone. In some cases a little reaction (e.g. a few Å) may provide a strong bond between the fibre and matrix, but in many

cases a thick, brittle reaction layer is deleterious in nature, being detrimental to load transfer. If the reaction layer reaches a critical thickness, a crack in the brittle interface may propagate through the fibre or composite. The critical thickness is determined by the interfacial bond strength and reaction layer morphology.

The likelihood of a chemical reaction may be ascertained by looking up the standard free energy change, ΔG°, for the reaction at a specific temperature. The driving force for a reaction is greater the more negative the number, whilst a positive value means that there will be no reaction. The speed of any reaction is then governed by the diffusion kinetics at that specific temperature. As mentioned, a small reaction layer is often beneficial for interfacial strength. Some common reactions are now considered.

Aluminium is highly reactive, and has the potential to reduce most oxide and carbide reinforcements [83-86]. However, the presence of a protective layer, such as alumina, will substantially reduce the reaction kinetics and consequently any reaction layers formed are only a few nm. The addition of magnesium to aluminium alloys has a great effect on the interfacial activity. Magnesium is highly reactive, particularly towards oxides (silica for example), and may form magnesium oxide, MgO, or a magnesium aluminate spinel, $MgAl_2O_4$ [87]. Magnesium does not form any stable carbides, but aluminium may react to form Al_4C_3. Two common examples are aluminium-magnesium alloys reacting with Saffil and silicon carbide fibres. In the first case Saffil, which has silica present at its surface and grain boundaries, is penetrated to a depth of a few nm by the magnesium during infiltration. In the second case Al_4C_3 particles form during heat treatment.

1.7 Composite Mechanical Properties

The mechanical properties of composites depend upon the matrix, the reinforcement and the interface. This section looks at relationships describing modulus and strength, and reviews the data available for these properties. The predicted modes of failure for

strong and weak interfaces are also presented. The geometry used in this report is shown in Figure 1.3, where direction 1 is parallel to the direction of the fibres (longitudinal direction), and direction 2 is perpendicular to the fibre direction (transverse).

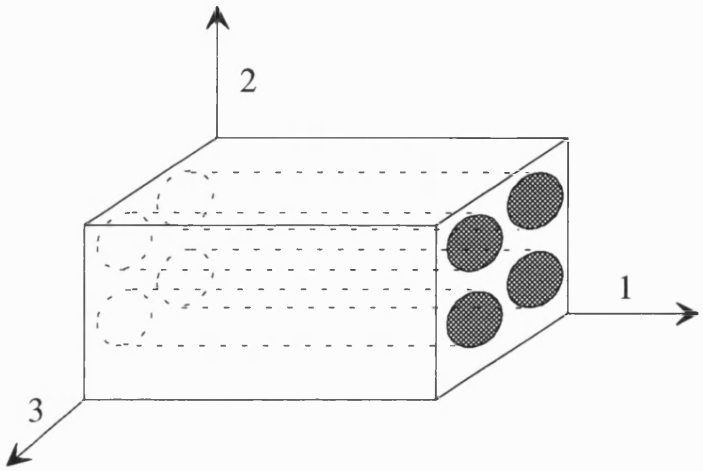

Figure 1.3 Schematic of fibre geometry for mechanical testing.

1.7.1 Young's Modulus

One of the main attractions of using composite materials is the potential to increase the stiffness of the matrix alloy, with little weight penalty. Particles and whiskers offer some improvement but the greatest benefits are from continuous fibres. Before an estimate of the elastic properties can be made, some assumptions must be made about the properties of the fibre/matrix interface [88].

(1) The fibre and matrix behave as elastic materials.

(2) The interface is infinitesimally thin.

(3) The bond between the fibre and matrix is perfect (no strain discontinuity across the interface).

(4) The material close to the fibres has the same properties as the material in the bulk form.

(5) The fibres are arranged in a regular repeating way.

Whilst (1) and (5) may be correct up to a point, none of (2)-(4) are strictly true.

1.7.1 (a) Longitudinal Modulus, E_1

If the bond between the fibres and matrix is perfect, when a load is applied to a unidirectional composite equal strains, ε_1, will be developed in the fibres and matrix. If the fibres and matrix behave elastically then the stresses developed may be described by

$$\sigma_f = E_f \varepsilon_1 \, , \sigma_m = E_m \varepsilon_1 \qquad \text{Eqn. 1.1}$$

where σ_f is the fibre strength, σ_m is the matrix strength, E_f is the fibre modulus and E_m is the matrix modulus.

For a composite of cross-sectional area, A, under a load, P, the average stress, σ_1, is

$$P = \sigma_1 A$$

$$P = P_f + P_m$$

then $$P_f = \sigma_f A_f \text{ and } P_m = \sigma_m A_m$$

therefore $$P = \sigma_f A_f + \sigma_m A_m$$

substituting $$P = \sigma_1 A \text{ and } \sigma_1 = E_1 \varepsilon_1$$

$$E_1 = \frac{E_f A_f}{A} + \frac{E_m A_m}{A}$$

consider $$v_f = \frac{A_f}{A} \text{ and } v_m = \frac{A_m}{A}$$

then $$E_1 = E_f V_f + E_m V_m$$

since $V_m = 1 - V_f$

$$E_1 = E_f V_f + E_m (1-V_f) \qquad \text{Eqn. 1.2}$$

which is known as the 'Rule-of-Mixtures' (or Voigt parallel model).

Eqn. 1.2, is based on the assumption of equal strains, which is not true since the fibre and matrix have different Poisson contractions (υ_f and υ_m) which lead to additional stresses. In practise however the error in E_1 is less than 1 or 2 %, and a close match is observed between theory and experiment for many composites. The equation also implies a linear relationship with the volume fraction of reinforcement V_f, Figure 1.4.

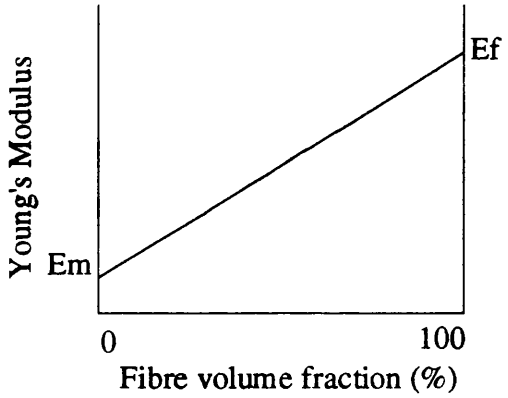

Figure 1.4 Schematic showing effect of V_f on modulus.

1.7.1 (b) Transverse Modulus, E_2

The behaviour of unidirectional fibre composites transverse to the fibre direction is harder to predict. The model proposed by Reuss (plates in series) assumes that the stress in the matrix, σ_m, and fibres, σ_f, are equal when a load is applied to the composite. The resulting strains are given by

$$\varepsilon_f = \frac{\sigma 2}{E_f}, \quad \varepsilon_m = \frac{\sigma 2}{E_m} \qquad \text{Eqn. 1.3}$$

The strain, ε_2, is therefore given by

$$\varepsilon_2 = V_f \varepsilon_f + V_m \varepsilon_m$$

and by substitution of Eqn. 1.3

$$\varepsilon_2 = \frac{V_f \sigma_2}{E_f} + \frac{V_m \sigma_2}{E_m}$$

substituting, $\sigma_2 = E_2 \varepsilon_2$,and rearranging

$$E_2 = \frac{E_f E_m}{E_f (1 - V_f) + E_m V_f} \qquad \text{Eqn. 1.4}$$

This model is not a good fit with reported experimental data, as it consistently underestimates the modulus. A closer fit to experimental data is obtained by incorporating Poisson contraction effects [88] to give

$$E_2 = \frac{E_f E_{m'}}{E_f (1 - V_f) + E_{m'} V_f} \qquad \text{Eqn. 1.5}$$

where $E_{m'} = \frac{E_m}{1 - \upsilon_m^2}$

and υ_m is the Poisson's ratio of the matrix.

Unfortunately the assumption of equal stress does not hold for equations 1.4 and 1.5. It is also wrong to assume uniform stresses within each phase, which is the case when fibres are represented as sheets in this model. Consider the treatment by Hull [88]. For an hexagonal array, Figure 1.5, subject to uniform strain. In XX' the majority of the strain is taken up by the matrix as $E_f >> E_m$. However, in YY' the strain will be more uniform and much lower than in XX'. This shows that there is a strain magnification in

the matrix between the fibres. The different strains in different parts of the matrix will give rise to additional stresses and therefore a non-uniform stress distribution.

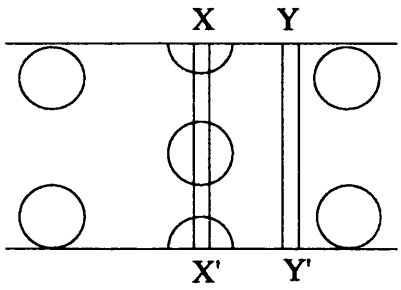

Figure 1.5 Cross-section through hexagonal packed fibre array.

Another method for predicting the transverse modulus is to use the Tsai-Halpin equations [89].

$$\frac{M}{M_m} = \frac{(1+\xi\eta V_f)}{(1-\eta V_f)} \qquad \text{Eqn. 1.6}$$

$$\eta = \frac{\left(\frac{M_f}{M_m}\right)-1}{\left(\frac{M_f}{M_m}\right)+\xi} \qquad \text{Eqn. 1.7}$$

where, M, is the composite modulus, M_f and M_m, the modulus of the fibre and matrix respectively, and, ξ, depends on the packing geometry, loading conditions. The disposable parameter, ξ, can be adjusted to agree with the experimental measurements, however its significance, if any, may not always be evident.

A further model proposed by Phillips [90], follows a geometrical approach developed from the model used by Kiess [91]. In this treatment the model defines upper and lower bounds on the transverse modulus of a fixed volume fraction. The model assumes a uniform square array, with fibres of square cross-section. This gives

$$\frac{E_2}{E_m} = \left[\frac{X}{\{1-X(1-R)\}+(1-X)}\right] \qquad \text{Eqn. 1.8}$$

Where

$R = \frac{E_m}{E_f}$, and X, is the side of the square fibre, as shown in Figure 1.6.

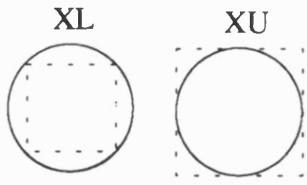

Figure 1.6 Representation of square fibre upper and lower limits

$$X_L = \frac{d}{\sqrt{2}} = \sqrt{\frac{2V_f}{\pi}}$$

$$X_U = d = \sqrt{\frac{4V_f}{\pi}}$$

The maximum value of X is unity, occurring at $4V_f / \pi = 1$. This gives $V_f = 0.785$, i.e. touching fibres. Applying this to the lower bound, $X_L = 0.707$. Errors also arise when entering $V_f = 1$, which does not give the value appropriate to a pure fibre. Girardi and Phillips [92] found an acceptable measure of agreement for the equation with their work on polymer matrix composites.

It has been shown that there are numerous models to describe the transverse modulus, none without some failing. Often an empirical combination is used [89]

$$E_2 = E_{REUSS} + C\,(E_{VOIGT} - E_{REUSS})$$

where C, is a contiguity factor between 0 and 1, commonly 0.2.

1.7.2 Strength

The strength of a metal matrix composite is very structure sensitive. Processing may induce thermal stresses and chemical reactions, which makes a simple ROM prediction difficult. In general the longitudinal strength is fibre dominated, whilst the transverse strength is determined by the matrix.

1.7.2 (a) Longitudinal Strength, σ_1

Assuming fibres of a uniform strength and equal strains,

$$\varepsilon_1 = \varepsilon_m = \varepsilon_f$$

$$\sigma_1 = E_f \varepsilon_1 V_f + E_m \varepsilon_1 (1-V_f)$$

Providing the fibre and matrix remain elastic, when the fibres break at the fibre tensile strength, σ_f, the strength will be

$$\sigma_1 = \sigma_f V_f + \sigma_{m'} (1-V_f) \qquad \text{Eqn. 1.9}$$

Where $\sigma_{m'}$, is the matrix stress level at the fibre failure strain. The response of the composite has been predicted by several authors [88, 89], Figure 1.7, fibre strengthening only occurs above a critical level of volume fraction. Below this critical level of reinforcement when the matrix fails the fibres cannot support the load and the composite fails.

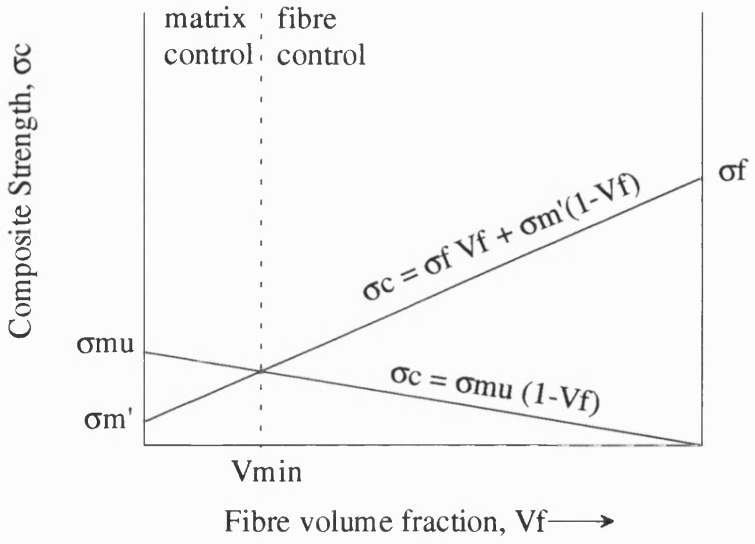

Figure 1.7 Effect of V_f on composite strengthening.

As mentioned previously ROM predictions are often unsatisfactory and frequently significantly higher than experimental values. Embrittlement by solute segregation is also a problem [93]. It should also be noted that the fibre strength is not uniform, and there will be significant variations from fibre to fibre as well as a distribution of flaw sizes present along each fibre. The reasons for this include processing and chemical reaction. Residual stresses arising during manufacture or subsequent processing may also alter the apparent strength of a composite.

1.7.2 (b) Transverse Strength, σ_2

The anisotropic nature of unidirectional composites is such that the transverse strength will be much less than the longitudinal strength, and at best equal to the strength of the unreinforced matrix alloy. Many factors such as: the nature of the interfacial bonding, fibre distribution, the presence of voids and internal stress distribution must be considered.

Cooper and Kelly [94] defined two limiting cases for the treatment of transverse strength: (1) a strong interface and (2) a weak interface. In the first instance they

reported that in a metallic matrix conditions of plane strain were supposed to develop between the fibres such that

$$\sigma_2 = 1.15\ \sigma_m$$

where σ_m is the strength of the matrix. This estimate is considered high, the maximum transverse strength for unidirectional composites being accepted as that of the matrix. For a weak interface the fibres are effectively treated as a series of holes, and the effective load bearing cross-section of the matrix is calculated.

Thus $$\sigma_2 = \sigma_m\left(1-\sqrt{\left[\frac{4V_f}{\pi}\right]}\right) \qquad \text{Eqn. 1.10}$$

Cooper and Kelly stated that σ_2 becomes zero at $V_f = 0.79$ not 0.91 as expected for close packed cylinders. This is true, but the equation is satisfactory for a square array of fibres where $V_f = 0.79$ is the limiting case. Modification of the equation leads to

$$\sigma_2 = \sigma_m\left(1-\sqrt{\left(\frac{2\sqrt{3}V_f}{\pi}\right)}\right) \qquad \text{Eqn. 1.11}$$

where $\sigma_2 = 0$ at $V_f = 0.91$, which is satisfactory for an hexagonal array of fibres (close packed). Further treatment of these models is difficult as fibres are rarely uniformly spaced and often touching. A lack of infiltration of touching fibres may also lead to stress concentration effects and further reduce strengths. Cooper and Kelly did modify their equation slightly, to account for the interface strength.

$$\sigma_2 = \sigma_m\left(1-\sqrt{\left[\frac{4V_f}{\pi}\right]}\right)+\sigma_i\left(\sqrt{\left(\frac{4V_f}{\pi}\right)}\right) \qquad \text{Eqn. 1.12}$$

Where σ_i', is the average tensile strength required to part the fibre from the matrix under transverse loading.

Greszczuk [95] takes the fibre and matrix properties, fibre-matrix bond, voids and the internal triaxial stress concentration and stress interactions due to fibres and voids into account for the prediction of σ_2.

$$\sigma_2 = \sigma_m \left(\begin{array}{l} (X_x K_x^* + Y_x K_y^*)^2 + (Y_y K_y^* + X_y K_x^*)^2 + (Z_z K_z^*)^2 \\ -\left[\begin{array}{l} (X_x K_x^* + Y_x K_y^*)(Y_y K_y^* + X_y K_x^*) + (Z_z K_z^*)(X_x K_x^* + Y_x K_y^*) \\ + Z_z K_z^* (Y_y K_y^* + X_y K_x^*) \end{array} \right] \end{array} \right)^{-\frac{1}{2}}$$

Where Xx, Yx, Xy, Yy and Zz are the internal triaxial stress concentrations in the matrix due to voids, and Kx*, Ky* and Kz* are the internal triaxial stress concentrations in the matrix due to fibres. Small terms Xz, Yz, Zx and Zy are neglected. Test results presented for a number of composites show reasonable agreement with the theory.

More recently Girardi and Phillips [92] have studied the properties of unidirectional glass-fibre composites. They found that additional matrix ductility did not improve the transverse tensile ductility, but did improve the shear properties of the composite. They also found that the reduction in strength associated with the introduction of fibres was less pronounced in matrices of lower initial strength and stiffness. Relating σ_2 to the matrix strength, σ_m, via a stress concentration factor

$$S = \frac{\sigma_m}{\sigma_2},$$

they defined a stress reduction factor.

$$\frac{1}{S} = \frac{\sigma_2}{\sigma_m}$$

Analysis of previous models (Keiss / Gresczcuk) which used a common matrix and varied the volume fraction, found them unable to predict the stress reduction factor for composites with similar volume fraction but with matrices of widely differing strength and stiffness.

The Cooper Kelly model was then examined and modified from their original equation (Eqn. 1.12).

$$\sigma_2 = \sigma_m (1-x) + \sigma_i' x$$

where $x = (PV_f)^{1/2}$, and P is the empirical relative volume fraction , that is volume of equivalent square fibre to volume fraction of actual fibre.

In terms of stress reduction factor the Cooper Kelly equation becomes

$$1/S = 1 - x + fx$$

where $f = \sigma_i'/\sigma_m$

This model proved unsatisfactory and was modified to account for residual shrinkage stress in the matrix. Thus for a constant shrinkage strain, e_s, in the matrix between the fibres and hence stress σ_s, the modified Cooper Kelly equation becomes,

$$\sigma_2 = (\sigma_m - \sigma_s) (1 - x) + \sigma_i' x$$

For modulus E_m, $\sigma_s = E_m e_s$

thus $$\frac{1}{S}=\left(1-\frac{E_m e_s}{\sigma_m}\right)+\left[\left(f-\left(1-\frac{E_m e_s}{\sigma_m}\right)\right)\right]x$$

This gives the limiting cases where f=0 for the lower bound and f=1 for the upper bound. Again this model is not ideal, but offers a logical step further in the analysis of transverse strength.

1.7.3 Modes of Failure

The modes of failure for unidirectional composites can be described in terms of loading orientation and interfacial bond strength. The treatment by Schulte [96] is considered here.

1.7.3 (a) Longitudinal Failure

Three cases can be considered. (1) When there is weak interfacial bonding the fracture surface is irregular and there is much fibre pull-out. There is no stress transfer as debonding is immediate. (2) In the case of intermediate interfacial bonding, there is less fibre pull-out and extensive matrix deformation. The matrix is observed to form dimples around the broken fibres, and the crack jumps from fibre to fibre. (3) When there is very good bonding, multiple fibre fracture occurs due to the stress field around the crack. These cases are presented schematically in Figure 1.8. Work by Hu et al [97] has shown that failure occurs at low strains due to flaw propagation within fibre bundles.

1.7.3 (b) Transverse Failure

In tension the stress concentration at the interface and the bond strength influence composite failure. (1) When the bonding is weak fracture occurs at the interface, stress concentration normal to the fibre also influences fracture. (2) In the case of intermediate bonding there is some debonding and the formation of dimples on fibres. Fibre shear failure is observed. (3) For a strong bond the failure can be either in the

matrix or fibre. Failure in the matrix is either by shear or associated with the formation of dimples. Failure in the fibre is by longitudinal splitting. These cases are shown in Figure 1.9. High hydrostatic stresses in the matrix and the nucleation of voids at the interface means that the ductile failure of the matrix occurs at relatively low strains [97].

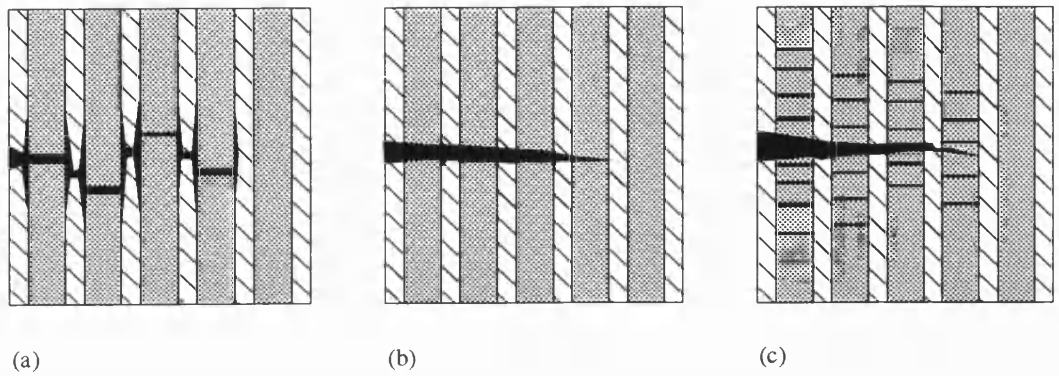

Figure 1.8 Schematic of failure mode for longitudinal tension. (a) Weak bonding, (b) intermediate bonding, (c) strong bonding. After Schulte [96].

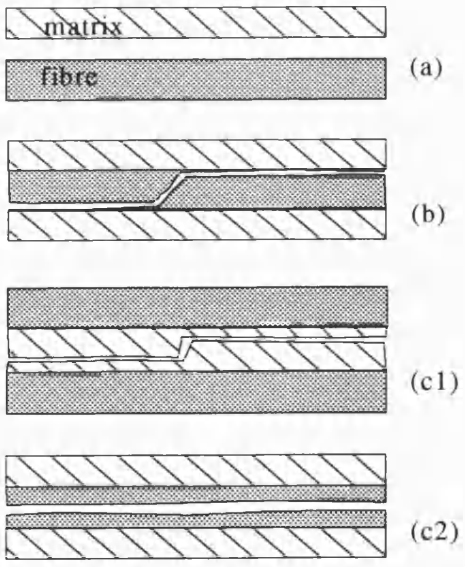

Figure 1.9 Schematic of failure modes for transverse tension. (a) Weak bonding, (b) intermediate bonding, (c) good bonding, 1 - matrix failure, 2 - fibre splitting. After Schulte [96].

1.7.4 Comparison of Longitudinal & Transverse Properties

Table1.2, presents the mechanical properties for a variety of composites as reported in the literature. From this it is clear that there are improvements in the longitudinal properties, but not for the transverse strength when compared with the matrix properties. For example, Al-5 wt.% Cu (T6) reinforced with alumina fibres, has longitudinal and transverse strengths of 860 MPa and 230 MPa respectively, which compare to a strength of ~400 MPa for the unreinforced alloy [101].

1.8 The Use of Heat Treatable Matrix Alloys

In the case of unidirectional MMCs the transverse strength is inferior with respect to the unreinforced metal. To improve the transverse strength a higher strength matrix can be used such as a heat treatable alloy. This section describes the principles behind precipitation hardening, and looks at some of the most important alloy systems.

1.8.1 Precipitation Hardening

The principle of precipitation hardening is to produce an optimum dispersion of fine precipitates which hinder dislocation movement and increase the strength of an alloy. The greatest resistance to dislocation motion is achieved when the precipitates are large enough to resist shearing by dislocations, yet distributed with a spacing which is too small to be by-passed. For an alloy to be amenable to precipitation hardening it must contain element(s) whose solid solubility in increases with increasing temperature.

Hardening is achieved via the following steps:

-the sample is taken to a sufficiently high temperature to dissolve the solute elements completely,

-the sample is quenched from the solution treatment temperature to give a supersaturated solid solution of the dissolved elements,

Table 1.2 Composite mechanical properties in longitudinal and transverse tension.

Fibre	Matrix	V_f	E_L (GPa)	E_T (GPa)	σ_L (MPa)	σ_T (MPa)	Reference
boron/borsic	Al-6061 (T6)	0.6	225	130	1400	100	[98]
α-alumina	Al-Li (T6)	0.6	230	150	600	196	
γ-alumina	Al-5Cu (T6)	0.6	150	110	860	230	
carbon (HM)	Al	0.6	235	135	550	70	
SiC (Nicalon)	Al	0.6	135	77	780	140	
alumina	Al-4Mg	0.44	190	120	570		[97]
alumina	Al-4Mg	0.3	150	100	400	140	
alumina	Al	0.3				75	
SiC (Tyranno)	Al	0.43	125	102	920	168	[96]
α-alumina	Al-2.5Li	0.34	181	126	538	177	
SiC (Textron)	Ti-6Al-4V	0.3-0.4	190-230		1800-2400		
SiC (Nicalon)	Al-6061	0.35	98		780	60	[99]
SiC (Nicalon)	Al-1100	0.3			800	70	
γ-alumina	Al-6061	0.4	130	95	245	160	[100]

-the sample is heated at an intermediate temperature (ageing) to promote controlled decomposition of the supersaturated solid solution and give a fine dispersion of precipitate.

The increases in strength and hardness produced by precipitation hardening are due to the extra stress required for dislocations to shear the precipitates that are formed. The precipitates form first by adopting coherency, or lattice matching between the precipitate and parent lattice, Figure 1.10. As a precipitate grows, strain builds up due to the difficulty in maintaining coherency, and the matrix distorts at or near the interface. The precipitates become more difficult to shear and the resultant hardness increases with time. A peak in the hardness versus ageing time is associated with a critical dispersion of coherent or semi-coherent precipitates. With further ageing the precipitates coarsen and dislocations are able to bow around the precipitous, by a mechanism known as Orowan bowing. The hardness decreases and continues to do so as both the precipitate size and the interparticle distance increase. The alloy is then said to be over-aged. The effects of alloy composition and ageing temperature on hardness versus ageing time are represented in Figure 1.11. They show that in the case of the aluminium-copper system increasing the solute content increases the hardness at a given ageing time, and decreases the time to reach peak hardness. Raising the ageing temperature also decreases the time to reach peak hardness.

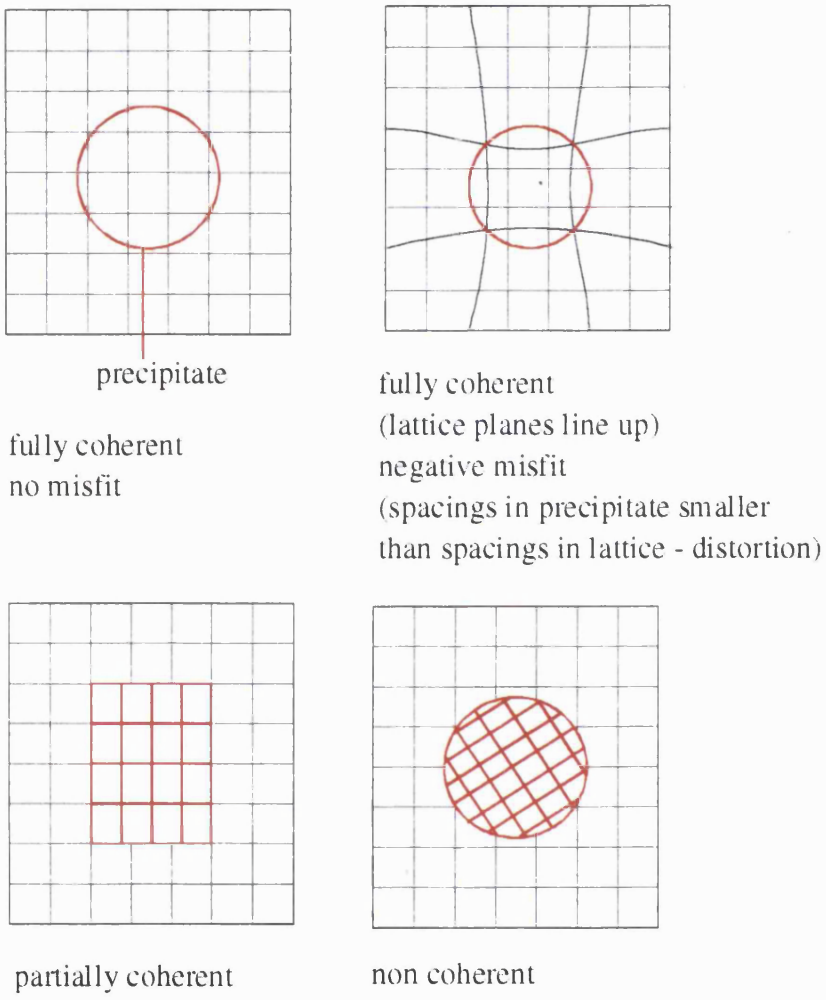

Figure 1.10 Schematic showing degrees of precipitate coherency.

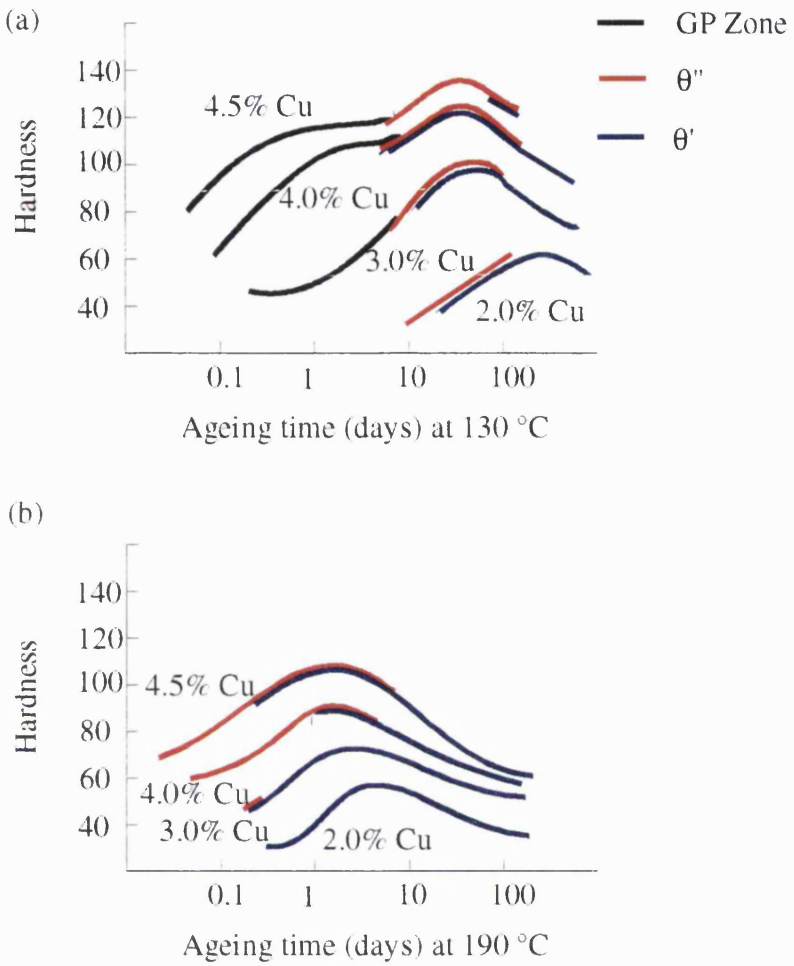

Figure 1.11 Schematic showing hardness versus ageing time at (a) 130°C and (b) 190°C for an aluminium-copper alloy. After Smallman [102].

1.8.2 The Aluminium-Copper Systems

The precipitation process for the binary Al-Cu system is one of the most widely studied systems [36, 102] and follows a series of intermediate transition stages before the equilibrium form of the precipitate is reached, Figure 1.12.

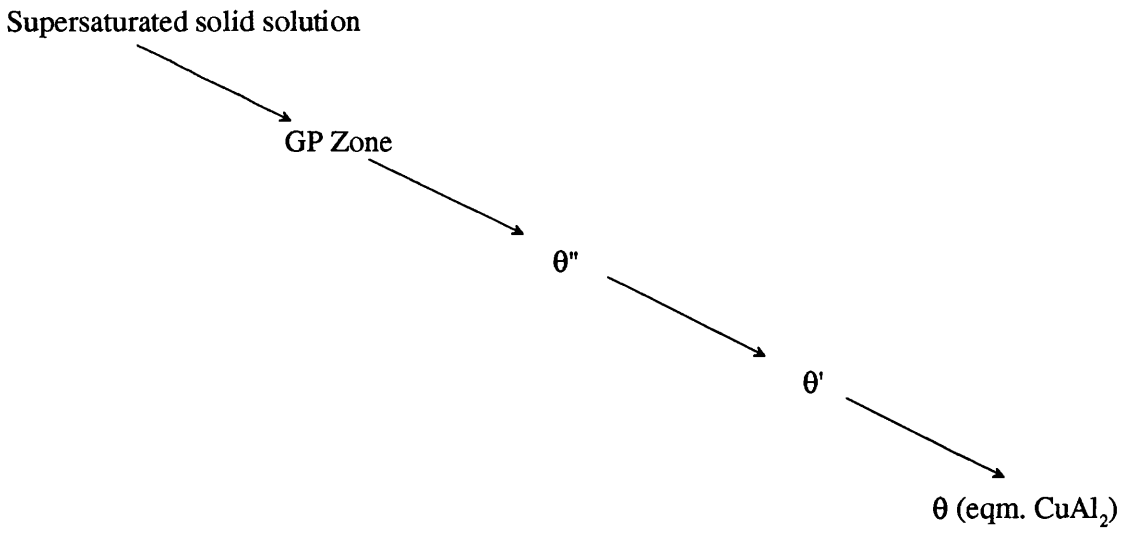

Figure 1.12 Precipitation sequence for aluminium-copper alloys.

Plate-like clusters of copper rich solute atoms, Guinier-Preston zones (GP zones), are recognised as the first stage in the precipitation process. They are metastable and coherent and form as plates ~ 3 Å thick, ~ 100 Å diameter on the {100} planes of the aluminium lattice. The next structure to form is θ", this is a fully coherent, metastable precipitate with a tetragonal structure, lattice parameters a = b = 4.04 Å, c = 7.8 Å. Elastic coherency strains are observed in the matrix, and these increase as the precipitate grows in the c direction. The precipitate dimensions are ~ 20 Å thick, and ~ 300 Å diameter. This structure is usually associated with peak hardness, its proposed structure is a central plane of 100% copper atoms, the next two planes consist of a mixture of copper and aluminium, while the other two basal planes are pure aluminium, giving an overall composition of $CuAl_2$. The next structure observed, also tetragonal, is θ', it is only partially coherent, and so the lattice strains are reduced in comparison with θ". The phase occurs as large rectangular or octagonal platelets, ~ 50 Å thick, and ~ 500 Å diameter with lattice parameters a = b = 4.04 Å, c = 5.8 Å. The final structure observed is the equilibrium phase θ, a body centred tetragonal phase, with a = 6.066 Å, and c = 4.87 Å, which is incoherent with the matrix. Softening

occurs as the coherency strains disappear. The precipitate has the composition of $CuAl_2$.

The precipitation process is influenced by the addition of further elements [102], for example iron or magnesium. In the case of the ternary Al-Cu-Mg alloy GPzones rich in Mg and Cu atoms form on the {100} planes in the aluminium, and S' platelets form on the {021} planes of the aluminium. These are both transitional structures, the equilibrium phase is the S precipitate, Al_2CuMg, which has an orthorhombic structure.

One alloy of particular interest is the quaternary Al-Cu-Mg-Ag alloy. This has a greater age-hardening response than other Al-Cu alloys. The structure of this precipitate has been greatly debated for over two decades. Initially workers postulated a monoclinic structure [40, 45] but this was disputed by Kerry et al who proposed a hexagonal structure [43]. Further workers revealed Auld's structure was more correctly described as orthorhombic [47], which is supported by the work of Muddle [48]. Reinterpretation of Kerry's work has found it to be consistent with that of Auld. Recent reports [49, 50], using convergent beam electron diffraction (CBED), refer to a tetragonal phase with $a = b = 6.07$ Å, $c = 4.87$ Å , with four-fold symmetry in a $<112>\alpha$ zone axis, giving the orientation relationship of:

$(001)\Omega \parallel (111)\alpha$, $[010]\Omega \parallel [10\bar{1}]\alpha$, and $[100]\Omega \parallel [\bar{1}2\bar{1}]\alpha$ After Fonda [49].

Garg [50], considered that due to the similarity of the lattice parameters, diffraction patterns along different zone axes can be consistently indexed as either orthorhombic or tetragonal. Although no definitive solution has been produced regarding the structure of Ω, it is generally believed to be a distorted form of the equilibrium θ phase, which is tetragonal.

The composition of Ω is also unresolved, with much inconsistency between reports. Chang and Howe [52] report the following compositions:

Ω enriched with Ag, but Mg not detected

63Al, 30Cu, 5Mg, 2Ag (atomic %)

85.2Al, 12.3Cu, 1.4Mg, 1.1Ag (atomic %)

25-35Cu, 1.2-6.4Mg, 1.0-1.5Ag (atomic %)

It has been reported [40, 42, 43, 48] that small additions of Ag (≈ 0.1 At.%) and Mg , and the value of the Cu:Mg ratio [40], were vital factors in determining the precipitation sequence and whether or not Ω formed. Recent reports, however, claim that Ω may be formed without Ag being present [49], which if the phase is Ω casts further doubt over its chemical composition. Chang and Howe [52] found no Ag or Mg in Ω, reporting 66.1 ± 3.2 Al, 33.9 ± 3.3 Cu (atomic %), close to the composition of stoichiometric $CuAl_2$, whilst Hono et al [53] report that Ag and Mg are found at the Ω/α interface (where α represents the aluminium lattice) in levels 1-5 at.% Ag and 1-6 at.% Mg.

Further questions are why Ω forms on the {111} planes of the aluminium lattice rather than the {100} mode which characterises θ' phase, and the importance of Mg and Ag. It has already been mentioned that Ω has been reported without Ag in the alloy. Fonda [49] reports that Ag acts to enhance the density of Ω precipitation. Scott et al [43, 46] proposed that Mg and Ag lower the stacking-fault energy of aluminium. They suggest that {111} is preferable to {100}, as close packed planes are crystallographically more favourable. They also suggest that the high degree of coherency between Ω and the aluminium lattice implies a low interfacial energy to promote nucleation. It is also known that the stacking-fault energy is lowered by solute atoms in aluminium and that the stacking-fault energy of aluminium decreases to accommodate segregation of solute on the close packed planes.

Hono et al [53], suggest that the addition of Ag to reduce the stacking fault energy promoting nucleation sites on the {111} planes is comparable to Al-Mg alloys, which form γ' precipitates on the {111} planes. Another theory reported is that the precipitation of the Ω phase is dependent on the formation of a precursor phase. Mg and Ag segregate to {111}α planes leading to the precipitation of Mg_3Ag which acts as a nucleating agent for Ω, although no evidence exists to support this. Hono et al [53] continue further stating that the nucleation of Ω is separate to GPZ and θ" and is also unrelated to the heterogeneous sites of dislocations. It is also reported that expansion of the lattice in the c-axis direction by 1.8% leads to the θ phase matching the {111}α plane perfectly. Substitution of Mg and Ag for Al and Cu respectively in the θ phase near its interface would cause the lattice of the θ phase to elongate significantly, possibly to match {111}α. Mg alone is sufficient but the addition of Ag gives improved matching.

The relationship between θ' and Ω has been investigated by Scott et al [46], who show that the volume fraction of Ω varies with that of θ' over time during ageing, such that Ω increases as there is a decrease in θ', Figure 1.13. This work highlights the long term stability of Ω and shows that control of ageing time is critical in order to obtain the optimum mode of precipitation.

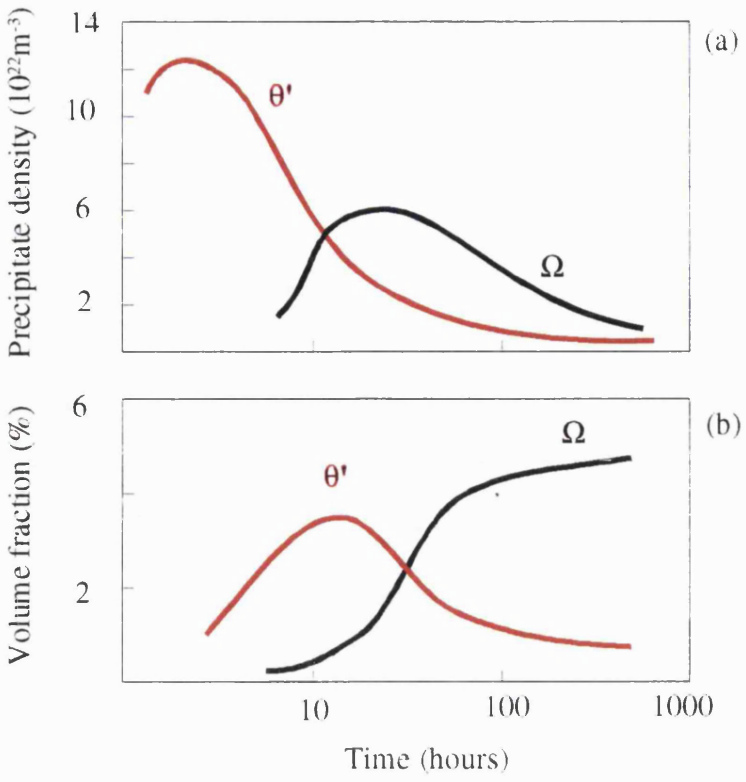

Figure 1.13 Variation in (a) precipitate density and (b) volume fraction of θ' and Ω with ageing time at 140°C. After Scott et al [46].

Much of the recent work employs entirely different heat treatments to the initial work, and it must be questioned whether the same precipitate is being studied or if there is a family of similar phases. At temperatures below 200°C, Ω is approximately 3nm x 100nm and does not increase much on over ageing [46], subsequent studies using different heat treatments report the precipitate to be up to 50nm thick with an aspect ratio between 10 and 100. It is generally accepted that Ω is a metastable variant of the θ phase, and exhibits hexagonal and octagonal morphology [49, 52], but it is clear that although many researchers have investigated the Ω precipitate for a number of years, there is still no definitive structure or composition.

1.9 Aims of the Investigation

From this review it is clear that much work has been done on the microstructure of MMCs, but reliable mechanical test results are in limited supply. This is primarily due to the difficulty of manufacturing unidirectional MMCs of high integrity and of a suitable size to test. Advances in processing, such as liquid metal infiltration, have made manufacture more reliable and the production of specimens for mechanical testing easier. Evaluation of unidirectional metal matrix composites has shown that although the reinforcement improves the longitudinal strength, the transverse strength is inferior with respect to the unreinforced metal. The effect of the reinforcement on the microstructure and ageing behaviour are also important, and must be related to the mechanical properties. From this the following project aims have been formulated.

A major aim of this work is to develop lightweight composites with improved transverse properties by the use of a precipitation hardening Al-Cu-Mg-Ag alloy matrix. Processing of the alloy/composite will involve three stages: melting and solidification, solution treatment, and ageing. Identical processing conditions will be employed for each of several systems to provide a basis for comparison. The systems considered were two different alloys, ARE415 and A201 reinforced with three different fibres, Altex, Nicalon and the Sigma monofilament, although problems meant that a full characterisation was not possible for the ARE415 matrix systems, and the Sigma monofilament systems.

Initial research will be focused on the physical and chemical effects of the reinforcing fibres on the matrix alloy. Primary objectives are to identify any second phases and interfacial reaction products formed, and to determine the influence of each processing stage on these products. Constitutional changes such as matrix composition, microstructure, and thermal strain due to the reinforcing fibres are expected to cause the solution treatment/ageing conditions giving optimum properties in the composite to be different to those of the unreinforced alloy. The main aim therefore is to optimise

the heat treatment of the composite on a basis of microstructure and mechanical properties transverse to the fibre direction. This will be achieved by the following programme of work.

1.9.1 Programme of Work

The programme of work consists of four main stages:

(1) the acquisition of data on the unreinforced matrix alloy microstructure, precipitation behaviour and mechanical properties.

(2) the manufacture by liquid metal infiltration of MMC based upon Al-Cu-Mg-Ag alloy (ARE415 and A201), and reinforcements of Nicalon, Altex and Sigma fibre.

(3) the study of the physical and chemical effects of the reinforcements on microstructure, including precipitation hardening.

(4) the optimisation of the microstructure and mechanical properties of the MMC.

The following techniques will be used:

Optical and scanning electron microscopy will be carried out to investigate fibre distribution, infiltration, porosity and second phase segregation.

Quantitative values of the fibre volume fraction and amount of second phase and porosity present will be measured using image analysis techniques.

Transmission electron microscopy studies will be employed to investigate the fibre/matrix interface reactions and the effect of reinforcement on precipitation sequence.

Hardness indentation techniques will be used to study the effects of age hardening.

Mechanical tensile testing will be carried out to obtain data on the strength and stiffness behaviour of the MMC.

This report continues with an experimental section which describes the techniques used in composite manufacture and the methods used to study microstructure and mechanical properties. This is followed by the results section which begins with

characterisation of the fibre and matrix and an examination of the effect of liquid metal infiltration on composite integrity. The microstructure of the different systems in the cast and aged conditions will then be studied in conjunction with the corresponding mechanical properties.

The discussion will correlate the microstructural data with the mechanical performance of the composites and compare the findings with relevant literature. Particular attention will be paid to the effects of heat treatment on the composite and relating the mechanical properties to the microstructure. The main conclusions of the study are then stated followed by suggestions for further work in this area.

2.0 EXPERIMENTAL DETAILS

2.1 Materials

2.1.1 Fibres & Monofilament

Three types of fibres were investigated, Altex, Nicalon, and Sigma. Analysis of the fibres was undertaken using scanning electron microscopy (SEM), and where required further compositional studies were carried out using electron-probe microanalysis (EPMA) and x-ray diffraction (XRD).

2.1.1 (a) Altex

This continuous alumina based fibre was supplied in the form of tows of fibres on a spool, see Figure 2.1. Samples of fibre were subjected to three treatments: (a) as received, and thermally exposed in air in a muffle furnace for 18 hours at (b) 800°C and (c) 1000°C . Subsequent to thermal exposure, 5g samples of the fibre were ground to a powder and then studied using x-ray diffraction, to obtain information as to the phases present, and their thermal stability. Electron-probe microanalysis (EPMA) was carried out on the fibre to obtain chemical compositions. To ensure that both the standards and specimens used for EPMA received the same treatments, they were cleaned, polished, and then coated with carbon at the same time.

2.1.1 (b) Nicalon

This is a continuous SiC-based fibre and it was supplied on a spool of 500 filament tows (see Figure 2.1). The fibre constituents are known to be silicon carbide, silicon oxycarbide and free carbon [33], but these have been found to vary between fibre batches, and so EPMA treatment, as described above for Altex, was performed.

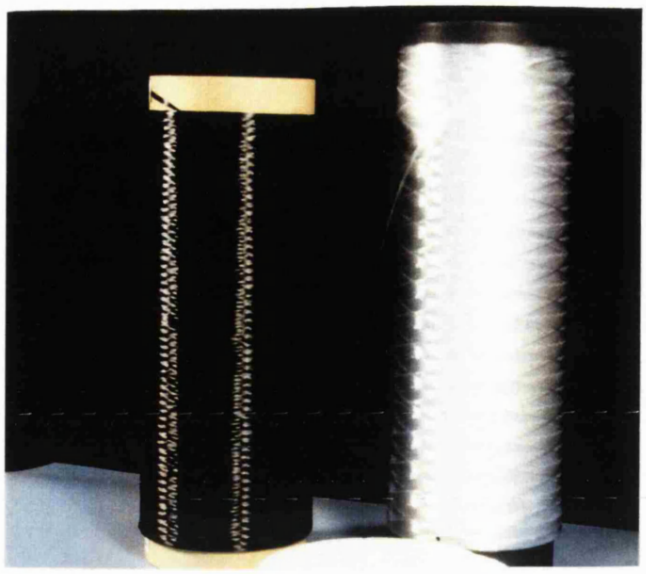

Figure 2.1 Nicalon and Altex Fibres as Supplied.

2.1.1 (c) Sigma

This silicon carbide monofilament was supplied in the form of a tape, with the fibres (of unknown coating) closely bound together. Thermogravimetric analysis (TGA) [103] was performed on a small specimen of Sigma monofilament in order to establish the temperature at which the tape binder is burnt off. An air atmosphere was used. Measurement of the variation of sample mass with temperature is made using a thermobalance enclosed in a controlled atmosphere. The balance operates in null-mode, ensuring that the sample stays in the same part of the furnace regardless of changes in mass. The mass is obtained from the energy required to keep the sample at the null-point.

2.1.2 Matrix Alloys

Two compositions of aluminium alloy were studied. The first designated ARE415 by the DRA, and the second A201 (US standard). The alloys were supplied in the form of cast blocks. Chemical analysis, performed at Holton Heath, was undertaken to establish the compositions of the unreinforced alloys, with EPMA performed at Bath for comparison.

2.2 Composite Manufacture

Composite manufacture involved two stages, the fabrication of a fibre preform, and its infiltration. Preform manufacture was performed at Bath and Holton Heath, and the liquid metal infiltration (LMI) performed at Bath University.

2.2.1 Preform Fabrication

Preform fabrication evolved throughout the study, with three main designs being used.

(1) In order to establish the compatibility and infiltration characteristics of each fibre type with ARE415 alloy, a hybrid preform was produced containing all three reinforcement types. The preform was constructed from commercially pure aluminium mesh (Expamet 602A) composition given in Table 2.1. A sheet of mesh was cut to an 'H' shape, and Nicalon and Altex fibres were wound from their spools onto opposite ends of the mesh. This operation was performed in a fume cupboard. Sections of the Sigma tape were cut using a scalpel, and then placed in the gap between the other fibres. All fibres were then secured in place by winding more mesh around them, and securing it with thermocouple wire.

Table 2.1 Composition of Expamet 602A Aluminium Mesh

Element	Si + Fe	Cu	Zn	Ti	Other	Al
wt.%	1.00	0.05	0.05	0.05	0.15	99.00

(2) The first single fibre type preforms were produced using a steel frame as shown in Figure 2.2a. The steel frame was fixed to a mandrel and then the fibres hand wound around the central region, Figure 2.2b. Top and bottom plates were then screwed in place to secure the fibres, Figure 2.2c.

(3) In the final arrangement fibre preforms were fabricated by winding fibre tows up to 50 layers onto a steel core plate (65mm x 45mm x 4mm).

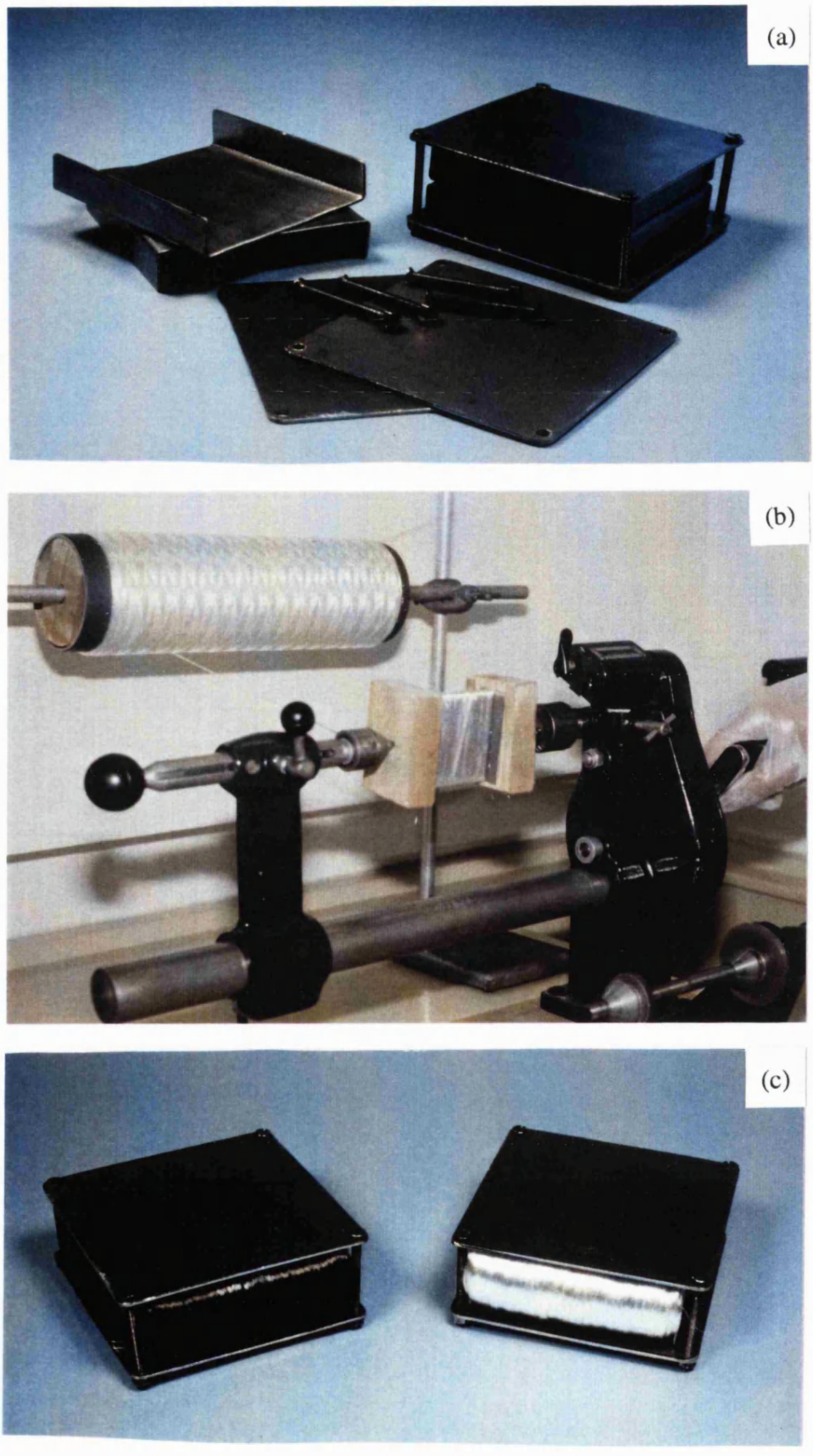

Figure 2.2 (a) Preform Frame, (b) Winding, (c) Finished Preform.

2.2.2 Liquid Metal Infiltration of a Fibre Preform

The LMI rig, Figure 2.3, consisted of a bottom pouring crucible and a launder lined with alumina mat, which fed molten alloy into a cylindrical 100mm diameter die preheated to 450°C, by eight 750W electrical resistance heaters. Before manufacture, the die, crucible and launder were vacuum cleaned to remove contamination. The die and ram were then painted with a graphite mould release. The preform was heated in a muffle furnace for 30 minutes prior to infiltration and then transferred to the die. The effect of preform preheat temperature was studied by looking at two temperatures, (1) 400°C and (2) 700°C. The liquid aluminium alloy (~800g) superheated by radio frequency induction coils was then poured into the die, two temperatures were studied, (1) 750°C and (2) 850°C. A load was then applied immediately by an hydraulic ram to aid infiltration. Two initial loads of (a) 10 tonnes and (b) 20 tonnes were investigated, and produced pressures of approximately 3 MPa and 7 MPa respectively. After a few seconds the pressure produced was increased to 25 MPa to assist consolidation. These loads were chosen as they correspond to pressures within the range predicted by theory for infiltration. After a few seconds the water cooling around the die was operated. The applied pressure was removed after the temperature reached ~300°C and the billet removed at ~100°C (between 30 minutes to an hour after pouring) by means of a dovetail profile on the ram.

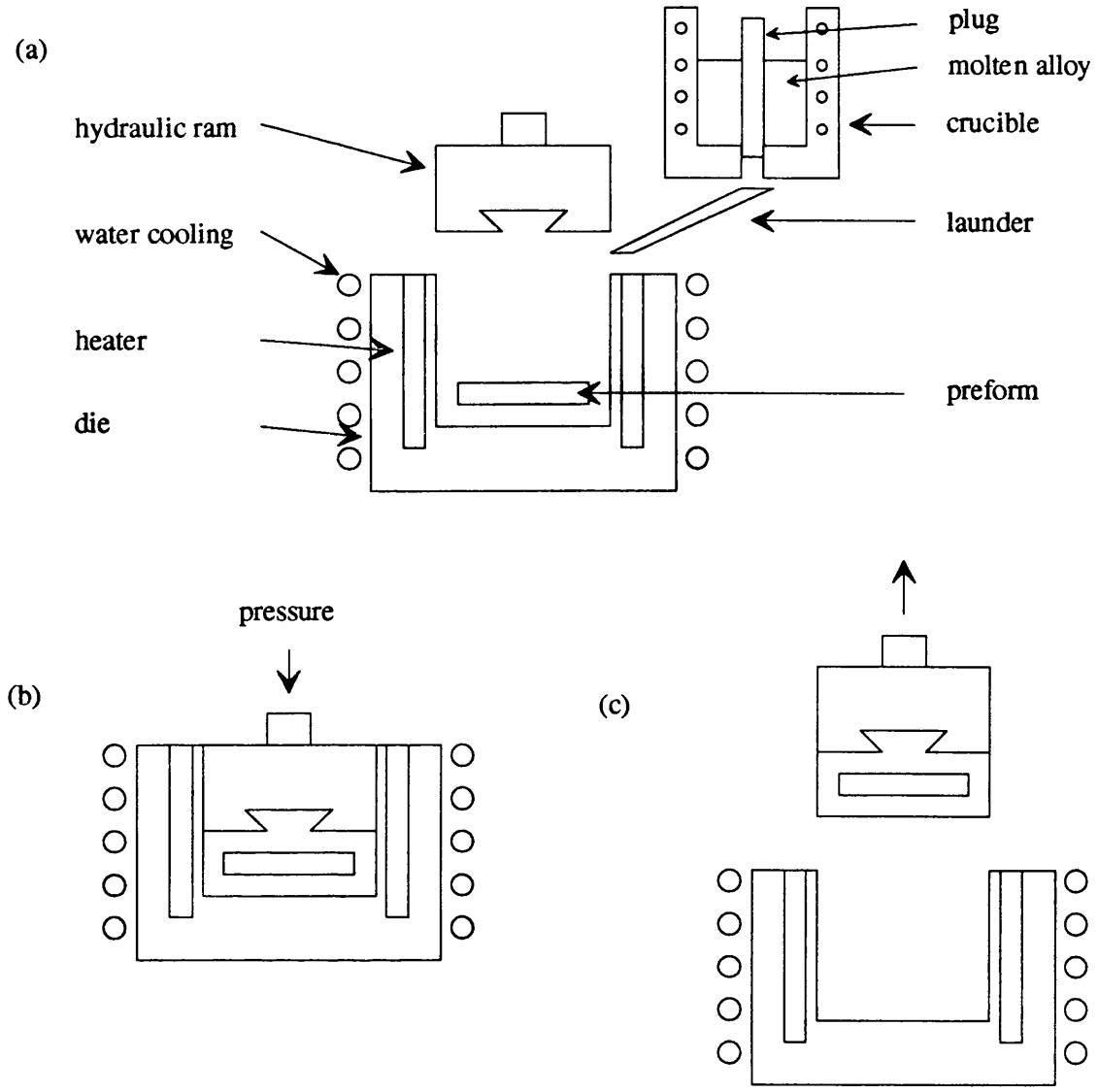

Figure 2.3 (a) Schematic of liquid metal infiltration rig, (b) Infiltration, (c) Extraction.

The billet was then sectioned using the Exotom cutter, and the infiltrated region removed for investigation. The uninfiltrated region was also retained as a control study. To produce samples for microstructural analysis (~1 cm x1 cm x1 cm), further sectioning was performed using a Discotom cutter with a diamond impregnated cutting wheel.

2.3 Heat Treatment

Heat treatment is required to homogenise the alloy after casting and to promote the growth of precipitates. ARE415 is not a standard composition of alloy, and so thermodilatometry and differential scanning calorimetry were used to determine a range of suitable temperatures for solution treatment. A series of experiments were then carried out to determine the most effective solution treatment.

2.3.1 Determination of Solution Treatment Temperature

2.3.1 (a) Thermodilatometry

This technique is based on the measurement of the expansion of solids and liquids. The coefficient of thermal expansion (CTE), α, is related to the structure and type of bonding present in a solid. A sample 10 x10 x40 mm was cut, and a thermocouple embedded in the centre. The sample was supported in a silica glass container by a graphite block. A dial gauge was connected to the top of the sample to measure changes in dimensions. The arrangement was placed in a vertical tube furnace, Figure 2.4.

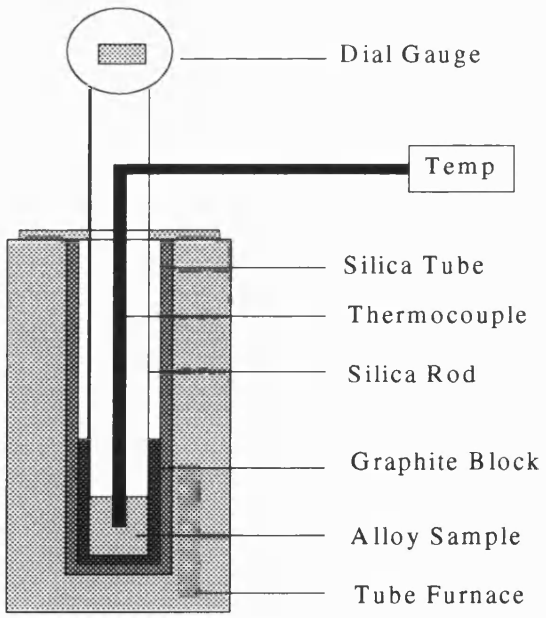

Figure 2.4 Schematic of Thermodilatometer Set-Up.

The sample was heated at a rate of 20°Cmin-1 to a temperature of 600°C. Measurement of the temperature T, and change in sample length Δl, were recorded. The experiment was repeated. A graph of T versus Δl was plotted to determine any changes in slope, or thermal arrests, which could be linked to changes of phase.

2.3.1 (b) Differential Scanning Calorimetry

When a solid is heated in an inert atmosphere the resultant structural changes are almost always accompanied by enthalpy changes, and sometimes changes in mass. The features of a thermal analysis curve (peaks and discontinuities of slope) can be linked to thermal events in the sample. With differential scanning calorimetry (DSC) [103] the sample and reference are maintained at the same temperature throughout a programmed thermal cycle. Any difference in the energy supplied to either in order to maintain both at the same temperature is recorded against the programme temperature. Thermal events in the sample can be identified as deviations from the DSC baseline.

A small disc of the alloy, 8.2mg, as used in TEM preparation, was found suitable for the process. The disc was sealed in an aluminium sample pan. The DSC was calibrated, and a baseline trace obtained. The sample was then heated according to the following thermal cycle:

Jump to 400°C

Equilibriate at 400°C

Ramp 10°Cmin^{-1} to 600°C

Cool

The resultant trace was compared with that of the baseline in order to establish any changes of phase.

2.3.2 Solution Treatment

Specimens cut from unreinforced alloy and composite ~10mm x 10mm x 10mm were subjected to one of the six two-stage solution treatments listed below.

(i) 500°C for 6 hours followed by one of;

(ii) (a) 520°C for 18 hours

(b) 520°C for 42 hours

(c) 530°C for 18 hours

(d) 530°C for 42 hours

(e) 540°C for 18 hours

(f) 540°C for 42 hours

Solutionising took place in a muffle furnace, and was followed by a cold water quench. The furnace temperature was monitored by a thermocouple placed inside a specimen, and found to be set point ±1°C. Electron-probe micro analysis (EPMA) was then performed on metallographically prepared samples to verify the success of the solutionising treatment. Transmission electron microscopy (TEM) was performed to study the fibre/matrix interface.

2.3.3 Artificial Ageing

Samples were aged immediately after solution treatment. Ageing was carried out at 175°C in air for times up to 1000 hours, this temperature was chosen to promote the growth of Ω precipitates, following work by Kerry [43]. At selected ageing times a sample was removed and left to cool naturally for subsequent microhardness and microstructural studies.

2.4 Metallographic Preparation

Prior to microstructural examination samples were mounted in a cold cure epoxy resin, selected to avoid undue thermal exposure to the matrix. A small exotherm of ≈50°C is experienced during the mixing of the resin.

Samples were prepared using a Buehler Metaserv 12" polishing wheel. Owing to the hardness differences between the matrix and fibres, the material removal rates differ. This can lead to problems such as pronounced relief effects and poor sample integrity. The polishing routes to counter these problem are documented in Tables 2.2-2.4.

The initial grinding stage removes damage and produces a planar surface. Subsequent stages with decreasing size of abrasive act to improve sample integrity. In between each stage the samples and holder are cleaned with Teepol and water, and then with methylated spirit. The integrity is then checked by optical microscopy, and if satisfactory, the samples are ultrasonically cleaned for 5 minutes. This removes any remaining abrasives, preventing scratching and contamination during later stages.

Table 2.2 Unreinforced alloy polishing sequence.

Surface	**Abrasive**	**Load per sample**	**Wheel speed**	**Duration**
SiC	320	2.5lb	250	till plane
P.Tex.	9μm o/b	5lb	360	4 min
Tex.	3μm o/b	5lb	360	4 min
Micro(brn)	0.06μm SiO_2	2.5lb	100	3 min

all stages complementary wheel rotation.

Table 2.3 Nicalon reinforced alloy polishing sequence.

Surface	**Abrasive**	**Load per sample**	**Wheel speed**	**Duration**
SiC	320	2.5lb	250	till plane
P.Tex.	9μm o/b	5lb	360	4 min
Silk	3μm w/b	5lb	360	4 min
Tex. (S.1)	0.06μm SiO_2	5lb	360	4 min
Chemomet(blk)	0.06μm SiO_2	2.5lb	100	3 min

all stages complementary wheel rotation.

Table 2.4 Altex reinforced alloy polishing sequence.

Surface	Abrasive	Load per sample	Wheel speed	Duration
SiC	320	2.5lb	250	till plane
P.Tex.	9μm o/b	5lb	min.	4 min (contra)
S.1	1μm o/b	5lb	360	4 min
S.1	0.06μm SiO_2	5lb	100	4 min
Master(wht)	0.06μm SiO_2	2.5lb	100	3 min

all stages complementary wheel rotation unless stated.

2.4.1 Electro-Chemical Etching

The use of an etch reveals information pertaining to the structure of a material not observed under standard metallographic preparations. By anodic oxidation in an aqueous solution, this method forms an optically anisotropic oxide layer on the surface of the specimen. The electrolyte used in this study was Barker's etch, consisting of fluoro boric acid (HBF_4) and distilled water mixed in the ratio 1:20. The conditions for etching using Polectrol equipment were: a flow setting of 2, and a voltage of 2V for 2 minutes. After etching the specimen is rinsed in running water. Microscopic analysis can then be performed under polarised light.

2.5 Light Optical Microscopy

Light optical microscopy techniques were used to study the infiltration, distribution of second phase and porosity, grain size and the volume fraction of fibre, porosity and second phase. Specimens were examined at various magnifications using a Zeiss ICM 405 light microscope. This has facilities for polarised light and differential interference contrast (DIC, which is used to pick up small changes in surface topography). Micrographs were taken as required using a 35 mm camera.

2.5.1 Image Analysis

Image analysis [104] was performed on metallographically prepared samples using a Zeiss light microscope attached to a Cohu high performance camera. The images were analysed using Optimas software packages to obtain the area fractions of fibres, porosity and second phase. The technique is based on distinguishing different phases by their contrasts. Using the Optimas package each part of the image is broken down into pixels, each pixel has a contrast ranging from 0 (black) to 255 (white). By setting thresholds, for example 0-50 is a fibre, 51-255 is matrix, it is possible to calculate the area fractions of different phases.

2.6 Electron Optical Microscopy

Due to the wavelength of visible light, light optical microscopy can only resolve objects up to a useful magnification of ~1000 times. Electron optical techniques can provide a useful magnification up to 0.5 million times, and in addition they can also yield compositional information [105].

2.6.1 Scanning Electron Microscopy

This study used an Hitachi T330, a JEOL 35C and a JEOL 6800 scanning electron microscope (SEM) equipped with a LINK AN10000 energy-dispersive spectrometer (EDS), and a back scattered electron detector. The EDS system allows for qualitative compositional analysis of the sample. The image from an SEM is made up of secondary electrons (low energy) and back-scattered electrons (high energy). Secondary electrons can be collected by applying a positive bias to the grid in front of the collector, and can reveal topographic information. Applying a negative bias to the grid enables back-scattered electrons to be collected, which give compositional information, as heavier elements give a higher back-scattered yield than lighter elements. The principles of SEM are well known and can be found in many reference books [102, 106].

Specimens for SEM were mounted in special holders, and a conducting path of colloidal graphite made between the sample and holder. If necessary a thin layer of gold was sputter coated onto the sample. This acts to reduce charging effects caused by non conducting parts of the sample [107], for example ceramic fibres.

2.6.2 Electron-Probe Microanalysis

Electron-probe microanalysis (EPMA) was performed using a JEOL 8600 Superprobe for quantitative analysis of elements. Operating conditions of 20KeV accelerating voltage and a beam current of 3 x 10^{-8}A were employed for the alloy and composite samples, with a reduced voltage of 10 KeV for the Altex and Nicalon fibres. Software on the probe provides a correction for: atomic number Z, absorption A, and fluorescence F. The ZAF corrected data (see appendix) was then analysed and average compositions calculated with 95% confidence limits. The principles are discussed in the appendix.

2.6.3 Transmission Electron Microscopy

Thinned samples were examined in a JEOL 2000FX transmission electron microscope (TEM) fitted with a LINK AN10000 EDS system. The TEM provides higher magnification than the SEM, and has much better spatial resolution, giving it improved ability for qualitative analysis. It is also possible to obtain diffraction patterns (basically a plot of the reciprocal lattice section), which fingerprint different phases. TEM principles are well documented elsewhere [102].

Specimens for transmission electron microscopy (TEM) were prepared by slicing thin sections normal to the fibre direction from which were drilled 3mm diameter discs. The discs were then ground to a thickness of 100-200μm and dimpled on both sides using a VCR model D500 dimpler. The discs were finally ion-milled in a Gatan Duomill 600, using a voltage of 5kV and an incidence beam angle of 15°, until perforation. The

beam angle was then reduced to 10° for a further hour to give a larger thinned region. A cryogenic stage was used to prevent further ageing of the specimen.

2.6.4 Diffraction Pattern Analysis

When electrons diffracted by atomic planes constructively interfere a spot pattern may be produced. Analysis of this spot pattern can yield information about the atomic configuration, lattice parameter and crystal orientation. The diffraction behaviour follows Bragg's law such that the incident beam of wavelength, λ, is diffracted by the interplanar spacing, d, through angle, θ.

$$n\lambda = 2d \sin \theta$$

However, because the angle of diffraction is very small Bragg's equation can be simplified to

$$n\lambda \approx 2d\,\theta$$

Electron diffraction from a set of atomic planes produces a series of spots which are symmetrical about a central axis. The distance, r, from the central spot to an outer spot can be related to the diffraction angle, θ, and the distance from the specimen to the pattern (the camera length of the TEM), l, by

$$\theta \approx r/l$$

Substituting this into Bragg's law gives

$$d = \frac{n\lambda l}{r}$$

When several d spacings have been calculated they can be compared with reference charts to identify the diffracting crystal. The beam direction can then be calculated by the vector product of two diffracting planes ($h_1\ k_1\ l_1$) and ($h_2\ k_2\ l_2$),

$$[u\ v\ w] = (h_1\ k_1\ l_1)\ .\ (h_2\ k_2\ l_2)$$

2.7 Mechanical Testing

Microhardness tests were carried out to determine the ageing response of the composite and unreinforced alloy. Tensile testing was performed to characterise the stress-strain behaviour of the unreinforced alloy and composite.

2.7.1 Microhardness Testing

Microhardness testing was used to obtain ageing curves for the heat treated alloy and composites. Testing was performed on a standard metallurgically prepared sample, using a Leco M-400 microhardness indentor with Vickers pyramid indentor. A load of 25gf was applied for a time of 15 seconds. 10 indents were measured for each condition, and the average hardness obtained.

2.7.2 Tensile Testing

The mechanical properties can be obtained by a number of methods including bend testing, torsional testing and tensile testing. The method of testing selected will influence the results, as different test geometries test different volumes of the test piece, and may also test different loading criterion such as pure tension, tension/compression, pure compression, or shear. The size of test piece is also important, particularly for brittle materials. Ideally the test specimen would be of the same dimensions as it would be in service, tested under the same loading conditions. In this instance pure tensile testing is the most applicable, testing the whole test piece.

For continuous fibre-reinforced metals, the ASTM [108] recommends that under tensile testing the cross-sectional area in the direction of the loading contains at least

200 aligned filaments. For particulate-reinforced metals NPL [109] recommend a cross-sectional area of 3mm x 6mm. BS EN 10 002 [110] advocate a gauge length of ≥ 30mm.

2.7.2 (a) Specimen Preparation

Tensile testing was performed on unreinforced alloy and composite samples following a method by Chen [111], which accounts for the above considerations. Composite samples were cut using a precision diamond cutting wheel (Isomet 2000). The samples were then machined to provide straight specimens of nominal length 65mm, gauge length 35mm, thickness 3mm and width of 6mm for longitudinal specimens and 8mm for transverse specimens, Figure 2.5. The samples then had aluminium tabs glued to the ends to protect them from gripping damage during testing. Alloy samples were cut from the same billet to the same gauge length and cross section, but with dog-bone ends of width 10mm and profile radius 6mm. Any heat treatment was performed prior to sectioning for all samples. Strain gauges of length 2mm and gauge resistance 120±0.3Ω, were bonded to the central section of all samples.

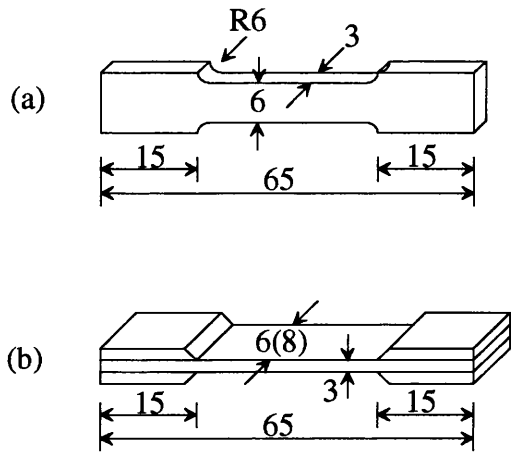

Figure 2.5 Tensile test piece dimensions, (a) unreinforced, (b) composite.

2.7.2 (b) Testing and Evaluation

Tensile testing was performed on an Instron 1195 using an 100KN load cell (50KN full scale load measurement) using a cross-head speed of 1mm/min. A data acquisition system was employed sampling at 100ms intervals to record the load and strain. A minimum of 6 samples per condition were tested. Strength and strain values were calculated directly from the acquired data, and modulus values from the stress-strain curve. Fracture surfaces were then examined by SEM.

3.0 RESULTS

3.1 Characterisation of Fibres and Monofilament

3.1.1 Altex

Analysis of the as-received fibre by scanning electron microscopy (SEM) and energy dispersive spectroscopy (EDS), Figures 3.1(a) and (b), shows the fibre to consist of aluminium, oxygen and silicon, with no obvious binder present. The x-ray diffraction (XRD) results from powdered Altex fibres are displayed in Figure 3.2, and show no difference in peak position or shape between the fibres tested at room temperature and those tested at 1000°C in an air atmosphere for 18 hours. A summary of the angle 2θ, d-spacing and intensity, I, is presented in Table 3.1, and comparison of the data with ASTM charts indicates the presence of several alumina, Al_2O_3, phases including, γ, δ and η. Electron-probe microanalysis (EPMA) of the fibre, Table 3.2, shows it contains 45 wt.% aluminium, 7.5 wt.% silicon and 47.5 wt.% oxygen.

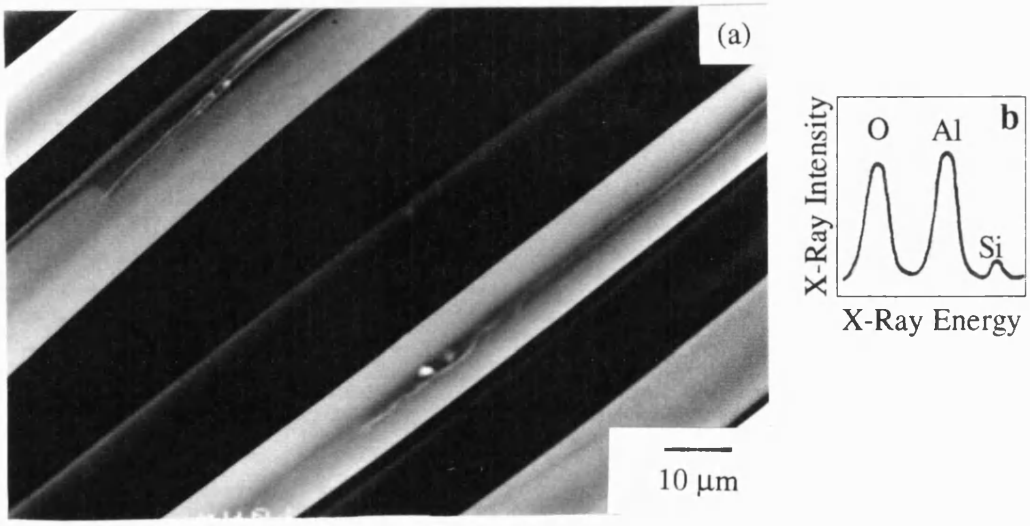

Figure 3.1 Altex Fibre: (a) SEM; (b) EDS.

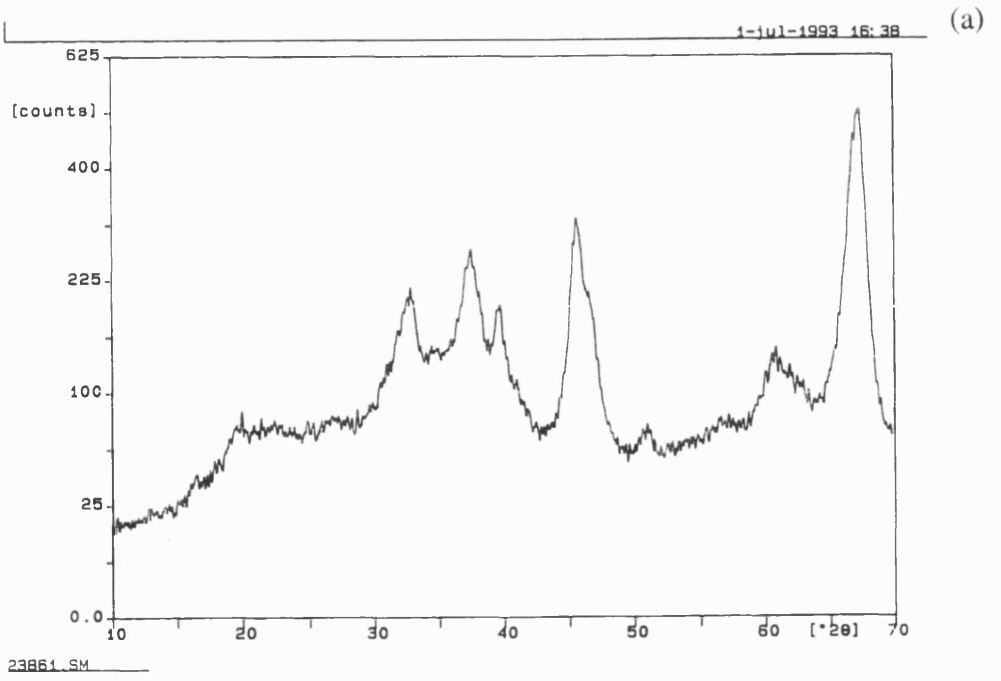

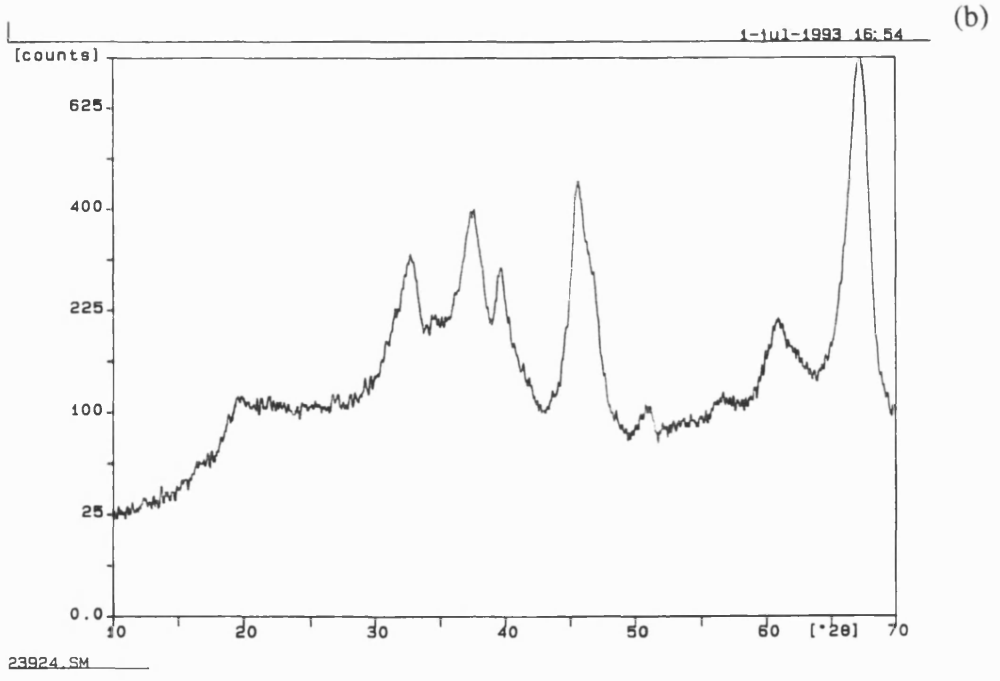

Figure 3.2 X-ray diffraction of Altex fibre: (a) room temperature; (b) 1000°C in air atmosphere for 18 hours.

Table 3.1 X-ray diffraction data for Altex fibre.

Angle 2θ	d-value (Å)	Intensity (%)
19.6	4.531	16.1
32.9	2.722	62.5
37.4	2.402	77.5
39.7	2.266	45.0
45.6	1.989	85.0
50.9	1.791	4.4
60.7	1.525	17.1
67.4	1.389	100.0

Table 3.2 EPMA data for Altex fibre.

Element	ZAF Corrected data	
	Wt %	At %
Al	44.9 ± 0.2	33.9 ± 0.2
Si	7.5 ± 0.2	5.4 ± 0.1
O	47.6 ± 0.5	60.6 ± 0.2
Total	100.0 ± 0.6	

3.1.2 Nicalon

Analysis of the as-received fibre by SEM and EDS, Figures 3.3(a) and (b), shows the presence of carbon, oxygen and silicon, with no obvious binder present. EPMA, Table 3.3, shows the fibre to contain 31.6 wt.% carbon, 54.9 wt.% silicon and 11.7 wt.% oxygen.

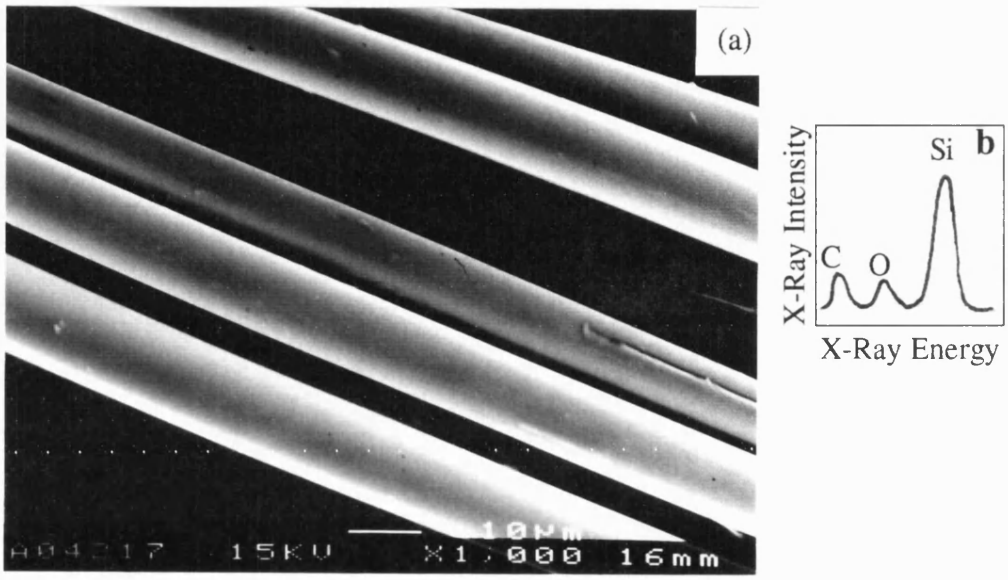

Figure 3.3 Nicalon fibre: (a) SEM; (b) EDS.

Table 3.3 EPMA data for Nicalon fibre.

Element	ZAF Corrected data	
	Wt %	At %
Si	54.9 ± 0.5	36.8 ± 0.1
C	31.6 ± 1.3	49.5 ± 0.3
O	11.7 ± 0.4	13.7 ± 0.2
Total	98.3 ± 1.3	

3.1.3 Sigma

The Sigma monofilament appear bound together, with a tape binder clearly visible on the bottom of the fibres, Figure 3.4(a). EDS, Figures 3.4, confirm that the monofilament has a tungsten core and reveals the presence of silicon and carbon in the fibre and silicon, carbon and oxygen in the binder. There was no evidence for any further surface coating. The tungsten core was 10 μm and the overall monofilament diameter was 100 μm.

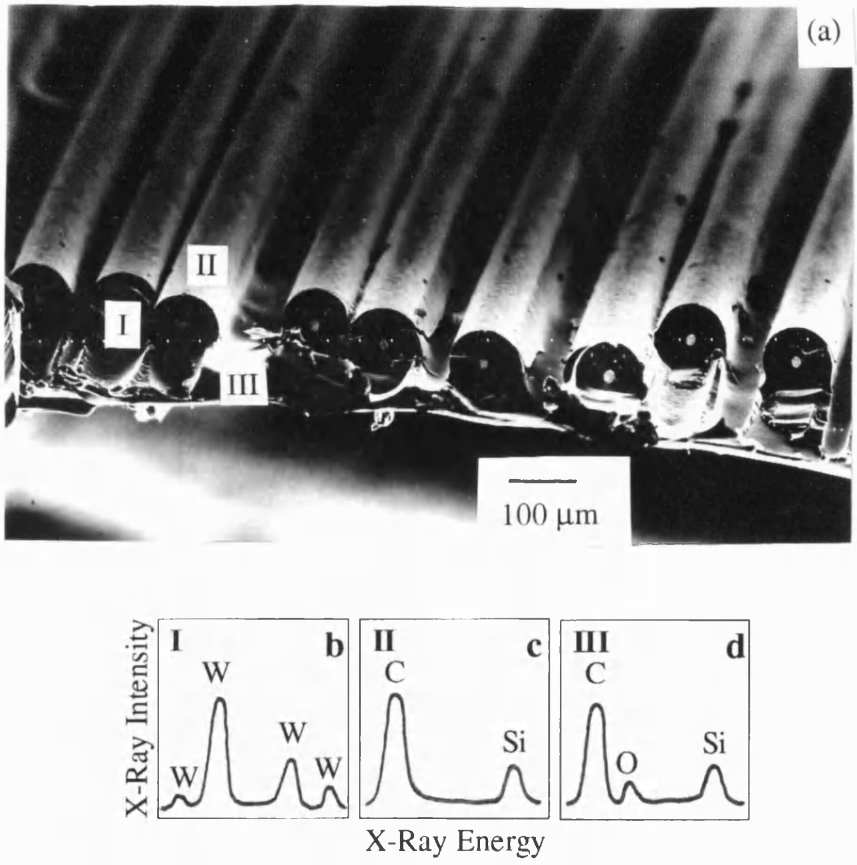

Figure 3.4 Sigma monofilament: (a) SEM; (b) EDS from core; (c) EDS from fibre; (d) EDS from binder.

3.2 Characterisation of the As-Received Matrix Alloys

3.2.1 ARE415

Chemical analysis results are given below in Table 3.4. Figure 3.5, a representative microstructure from as-received alloy, shows a typical cast structure with second phase and large irregular porosity widespread throughout the sample.

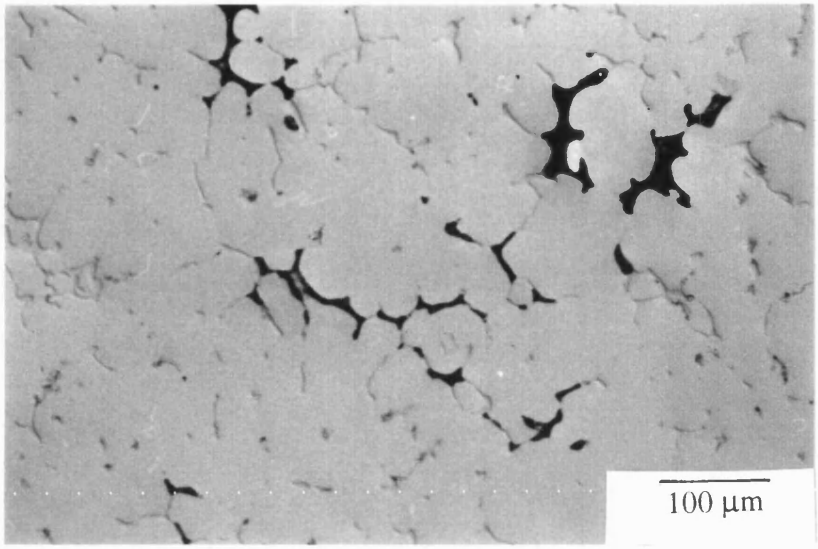

Figure 3.5 Optical micrograph of ARE415, as-received condition.

Table 3.4 Chemical composition of as-received ARE415.

Element	Cu	Mg	Ag	Zn	Mn	Ti	Si	Fe
wt.%	4.26	0.70	0.43	1.59	0.24	0.18	0.03	0.06

3.2.2 A201

Chemical analysis results are given in Table 3.5. The as-received structure for the A201 alloy, Figure 3.6, is similar to that of the ARE415, common features are widespread second phase and porosity.

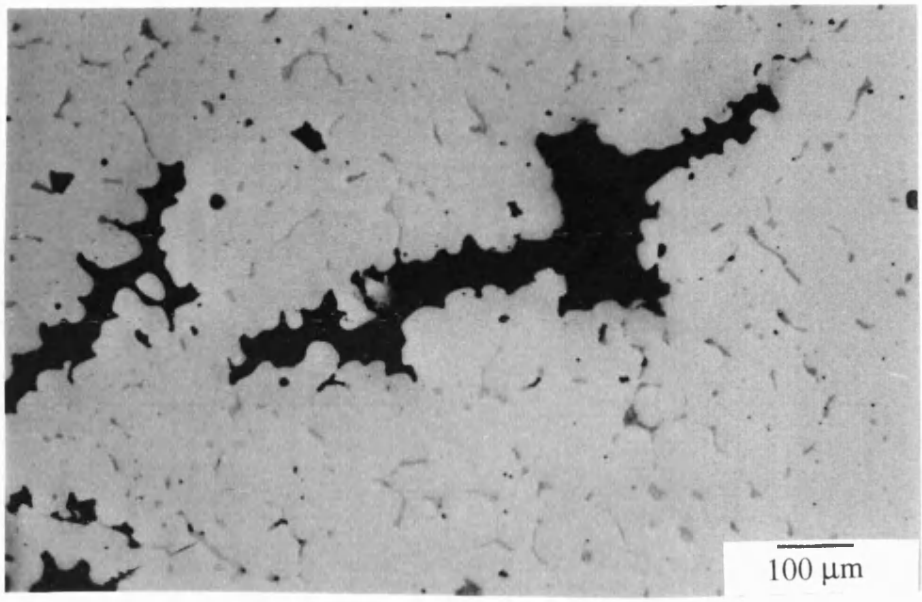

Figure 3.6 Optical micrograph of A201, as-received condition.

Table 3.5 Chemical composition of as-received A201.

Element	Cu	Mg	Ag	Zn	Mn	Ti	Si	Fe
wt.%	4.65	0.31	0.70	-	0.28	0.18	-	-

3.3 Liquid Metal Infiltration Parameters

The different infiltration pressures and melt temperatures used in the manufacture of ARE415 based composites are collated in Table 3.6, subsequently composites are referred to as I - IV. All of composites I - IV were cast using preforms preheated to 400°C prior to infiltration.

Table 3.6 Summary of infiltration pressures and alloy melt temperatures used for ARE415 alloy composites.

	Melt Temperature	
Pressure	750°C	850°C
7 MPa	I	II
3 MPa	III	IV

A macrograph, Figure 3.7, of a section through composite I, shows that towards the edge of the billet, region (i), infiltration is good, whereas in the centre of the billet, region (ii), infiltration is incomplete, as evident by the high level of matrix porosity. Figure 3.8 shows a macrograph of composite II, which in this case shows complete infiltration. Composite III was not investigated. Figure 3.9, a macrograph of composite IV, shows that some fibres have not been wetted. Further analysis of composite I, using a different preform arrangement, Figure 3.10(a), shows that in addition to poor infiltration there is a variation in fibre volume fraction. The volume fraction appears greatest in the middle of the billet, decreases significantly towards the top and bottom surfaces of the billet, and shows some variation across the width of the billet. This problem was substantially reduced when the preform preheat temperature was increased to 700°C, as shown in Figure 3.10(b).

Following analysis of the above results composites were fabricated using a melt temperature of 850°C and an initial applied pressure of 7 MPa followed by consolidation at 25 MPa (i.e. composite II), with a preform preheat temperature of 700°C.

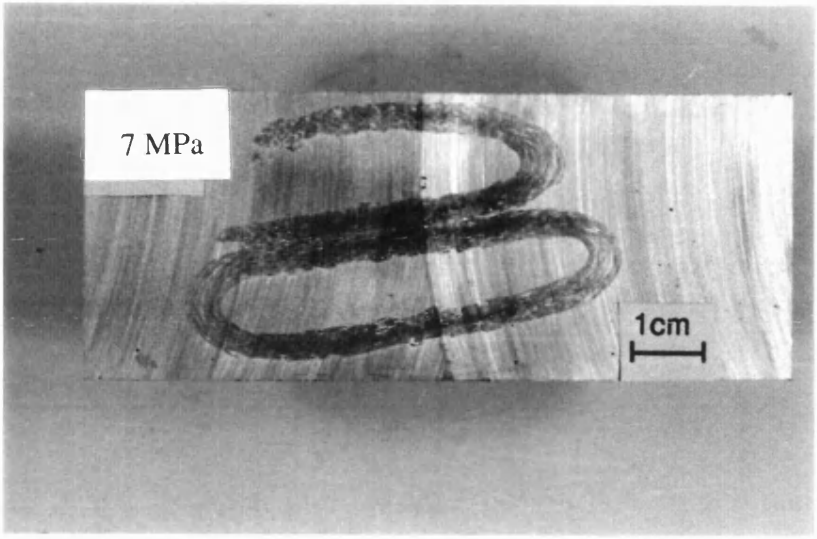

Figure 3.7 Composite I: 750°C melt temperature, 7 MPa pressure.

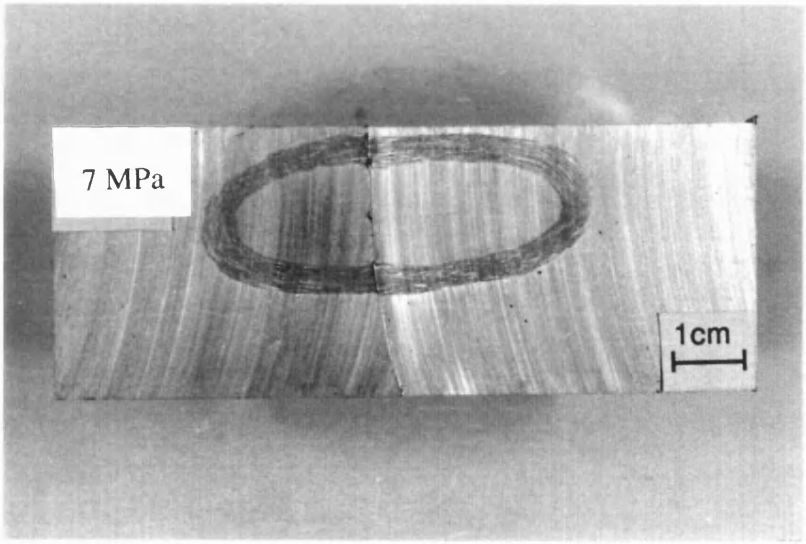

Figure 3.8 Composite II: 850°C melt temperature, 7 MPa pressure.

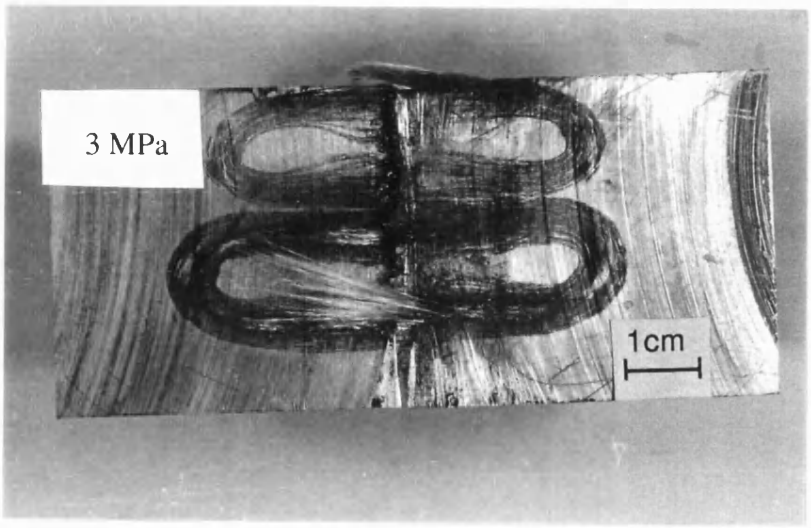

Figure 3.9 Composite IV: 850°C melt temperature, 3 MPa pressure.

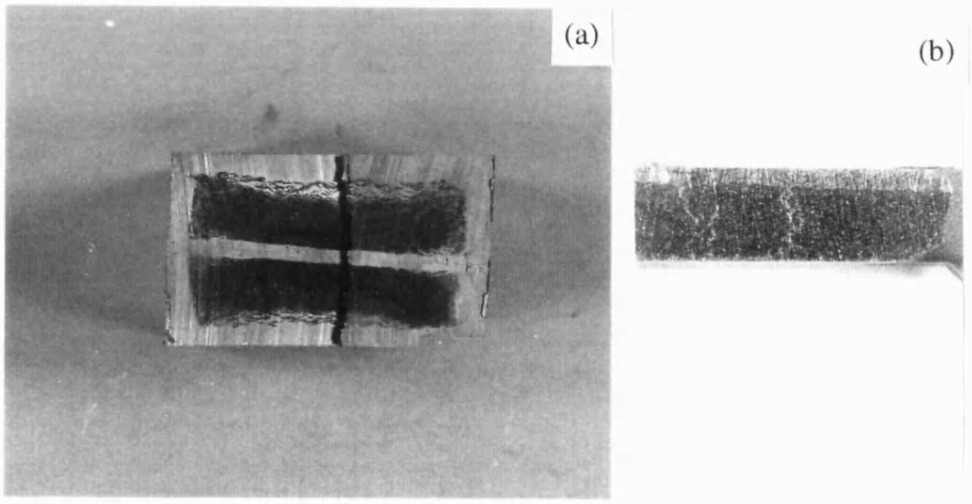

Figure 3.10 Variation in fibre distribution with preform preheat temperature:

(a) 400°C; (b) 700°C.

3.4 Microstructure & Mechanical Testing of ARE415 Alloy Systems

3.4.1 Unreinforced

3.4.1(a) Microstructure

(i) Cast

Figures 3.11(a-c), back-scattered electron image (BEI), optical and etched respectively, show a typical cast structure, the contrast in colour (due to differences in atomic number) being indicative of coring, which gives rise to the formation of $CuAl_2$ in a divorced eutectic. The $CuAl_2$ composition was confirmed by WDS to be 47.3 ± 1.6 wt.% Al and 48.7 ± 0.8 wt.% Cu, but there were also submicron phases containing iron and manganese within this phase. Image analysis indicates less than 1 vol.% of porosity, ~7 vol.% of $CuAl_2$, a grain size of ~200μm and a dendrite arm spacing of ~20μm.

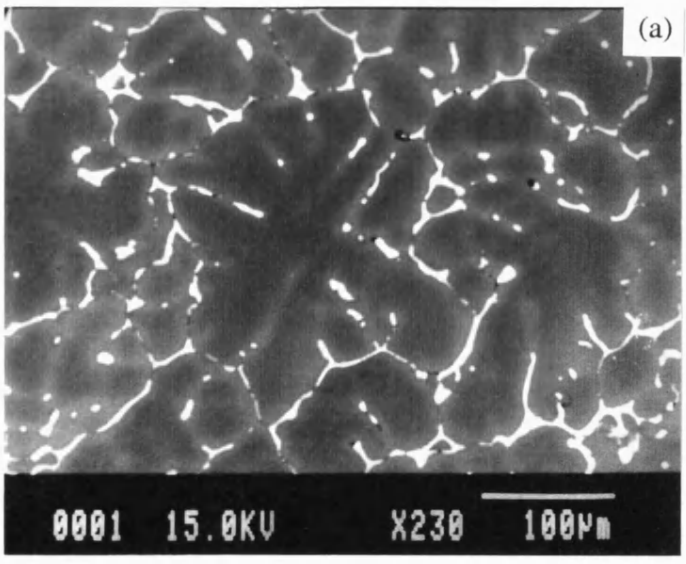

Figure 3.11 ARE415: (a) back scattered electron image;

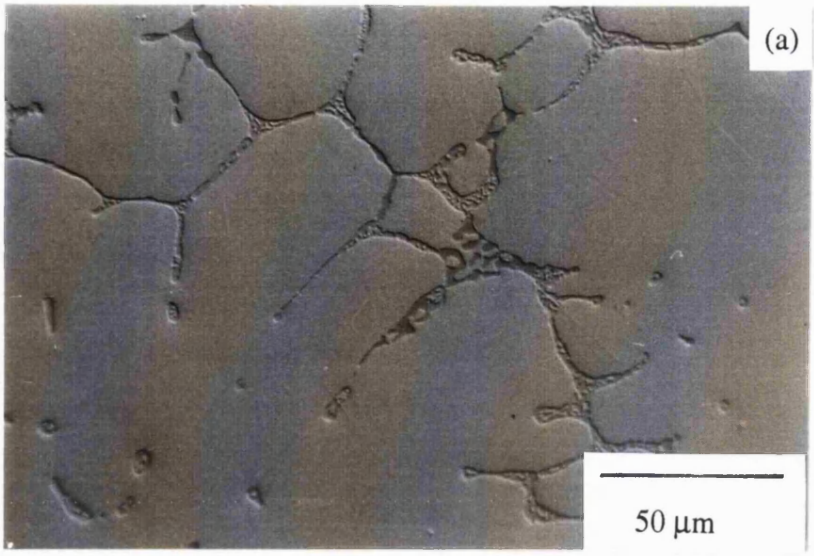

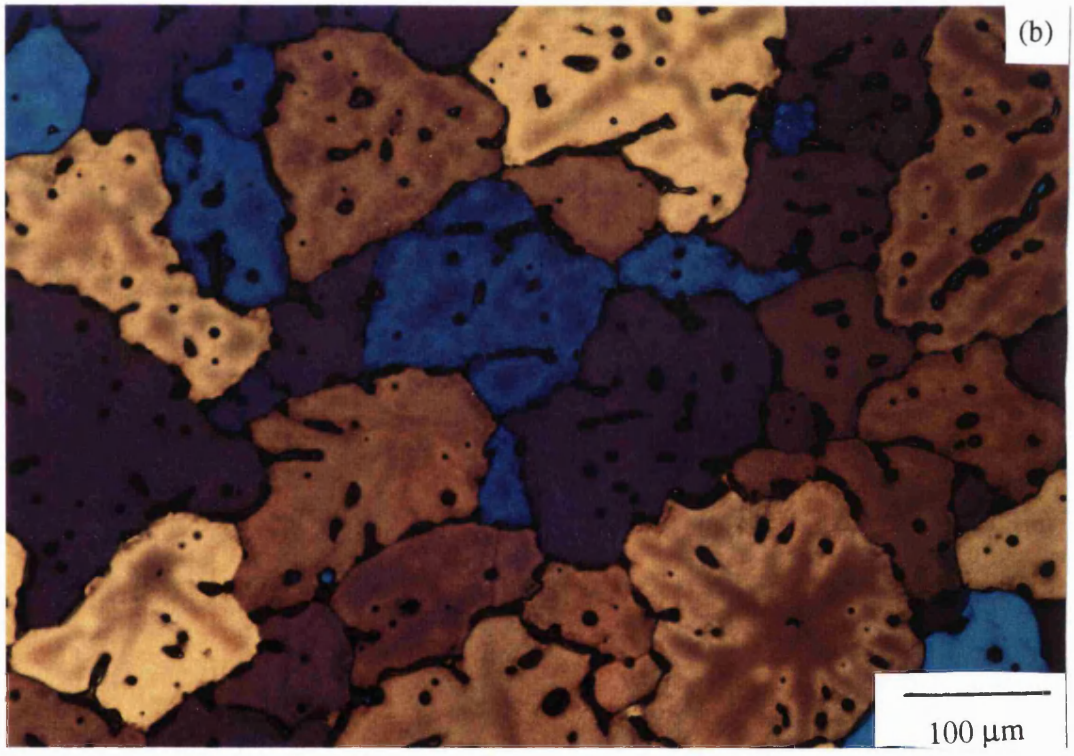

Figure 3.11 ARE415: (b) optical micrograph showing intermetallic second phase; (c) optical, etched.

Transmission electron microscopy (TEM) of the cast alloy shows that regions of precipitation has occurred during fabrication, with precipitates up to 50nm thick and 500nm long, Figure 3.12. The precipitates observed lie in two different directions normal to each other, which suggests they most likely belong to the θ family.

Figure 3.12 Transmission electron micrograph from cast ARE415.

(ii) Heat-Treated

Establishment of Solution Treatment Procedure

A graph of expansion versus temperature obtained from the dilatometry experiments is shown in Figure 3.13.

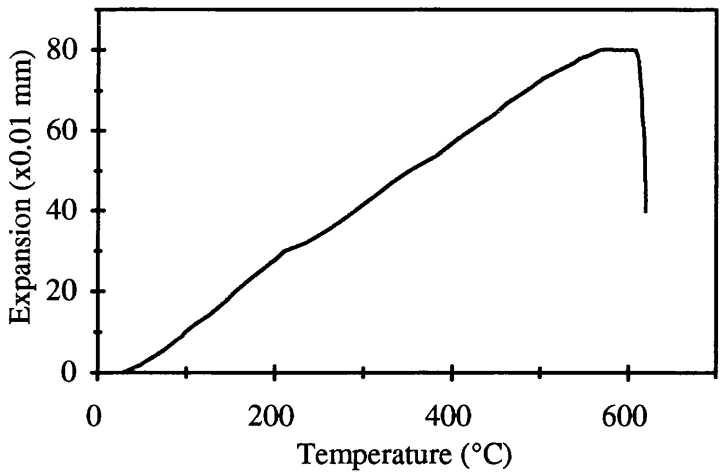

Figure 3.13 Expansion versus temperature for ARE415 alloy.

The graph is approximately linear until 503°C where a change in slope occurs indicative of a phase change. The graph then remains linear after 503°C until a plateau at ~543°C, followed by a marked drop in expansion, indicating melting.

Results from DSC experiments are presented in Figures 3.14(a) and (b), which show a baseline trace and alloy trace respectively. Figure 3.14(b) deviates from the baseline at ~521°C, 546°C and 580°C, indicating changes of phase and melting.

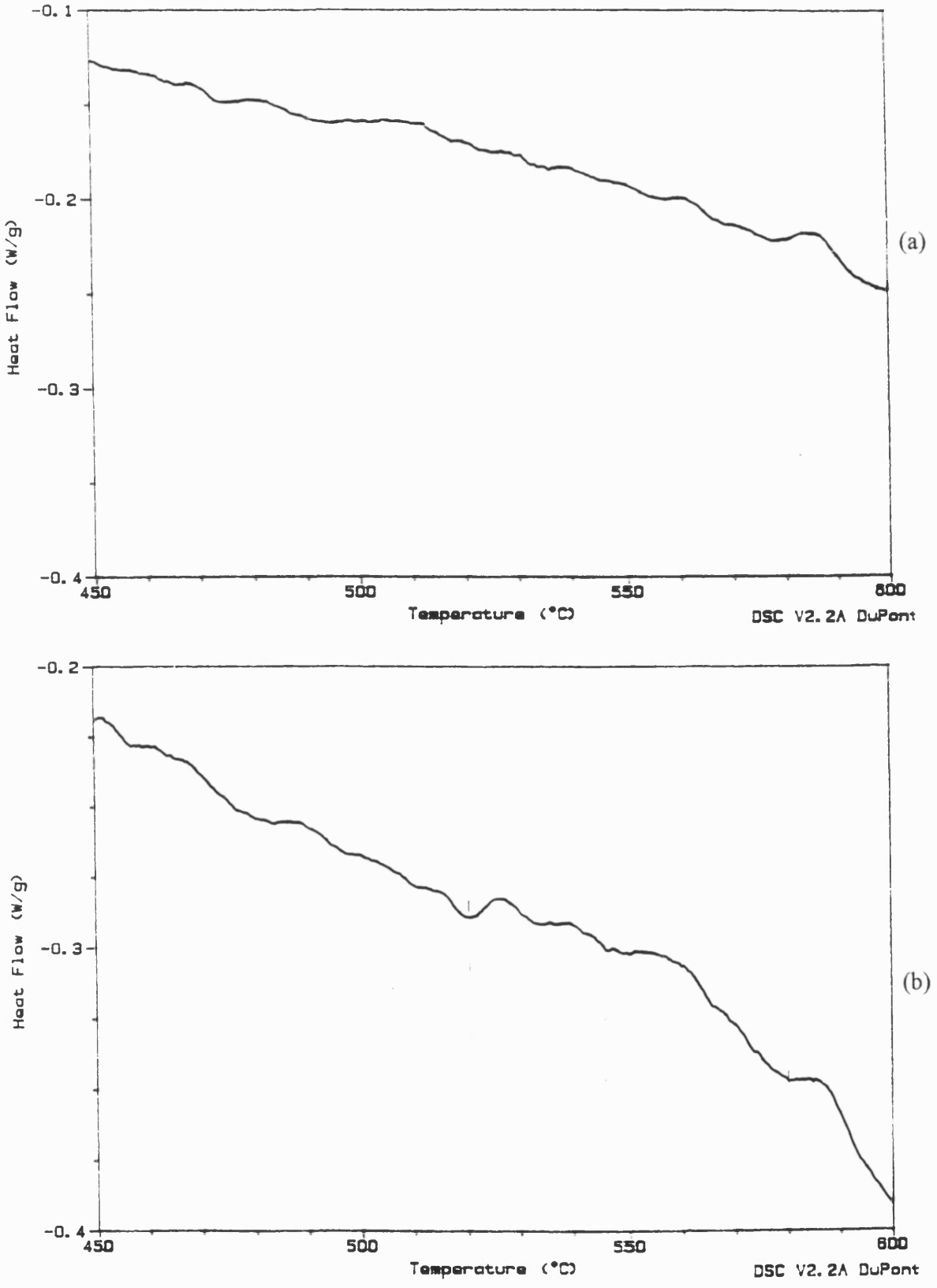

Figure 3.14 Differential scanning calorimetry traces: (a) reference baseline; (b) ARE415 alloy.

From the evidence above, the following two-stage heat treatments were investigated on the ARE415 alloy.

(i) 500°C for 6 hours followed by one of;

(ii) (a) 520°C for 18 hours

(b) 520°C for 42 hours

(c) 530°C for 18 hours

(d) 530°C for 42 hours

(e) 540°C for 18 hours

(f) 540°C for 42 hours

The effectiveness of each treatment was assessed by image analysis, to determine the area % of second phase remaining, and EPMA to check the composition and removal of coring.

Figure 3.15, shows a histogram for the amount of second phase remaining after various solution treatments. It can be seen that the solution treatment offers significant improvement compared to the cast condition. Increasing the second stage temperature reduces the amount of second phase retained, with no gains from extending the time.

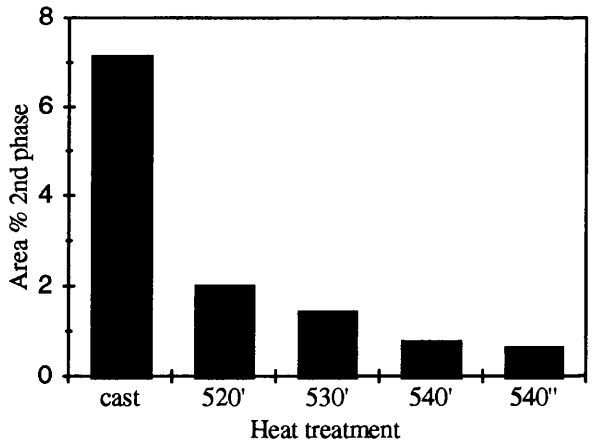

Figure 3.15 Histogram showing the effect of solution treatment temperature on reduction of in amount of second phase (' - 18 hours, " - 42 hours).

The results from EPMA are summarised in Table 3.7, the cast condition is included for comparison. It is clear that all the solution treatments were successful in dissolving second phases and reducing coring in alloy ARE415. The second phases that did remain were too small for quantitative analysis.

The solution treatment schedule selected for all systems was, 500 ± 5°C for 6 hours followed by 530 ± 5°C for 18 hours, in an air atmosphere.

Figure 3.16, shows a typical solution treated microstructure, the amount of $CuAl_2$ intermetallic, ~1 vol.%, is considerably reduced compared with ~7 vol.% in the cast condition. The remaining second phase was found by EDS to contain iron and manganese (the phases were too small for quantitative analysis).

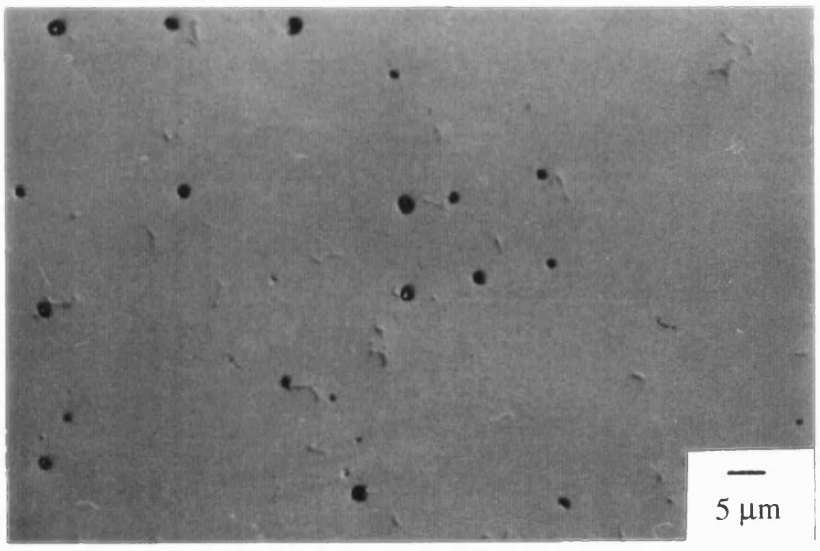

Figure 3.16 Solution treated ARE415 alloy.

Table 3.7 Comparison of ZAF corrected wt.% data for solution treated ARE415.

Element	cast mid dendrite	cast dendrite edge	500°C 6 hours mid dendrite	500°C 6 hours 520°C 18 hours	500°C 6 hours 520°C 42 hours	500°C 6 hours 530°C 18 hours	500°C 6 hours 530°C 42 hours	500°C 6 hours 540°C 18 hours	500°C 6 hours 540°C 42 hours
Al	92.7±2.0	87.9±2.0	89.7±0.	91.6±0.2	90.3±0.4	91.8±0.4	89.7±0.4	91.4±0.4	91.8±0.7
Cu	2.45±0.61	4.07±0.67	4.04±0.09	4.08±0.14	4.32±0.23	4.11±0.07	4.33±0.04	4.38±0.08	3.72±0.13
Mg	0.39±0.07	0.61±0.09	0.67±0.04	0.61±0.03	0.59±0.04	0.57±0.05	0.57±0.03	0.54±0.04	0.54±0.04
Ag	0.41±0.10	0.45±0.03	0.39±0.02	0.41±0.04	0.37±0.05	0.39±0.05	0.42±0.03	0.40±0.02	0.40±0.04
Zn	4.27±0.33	5.43±0.21	4.61±0.09	4.62±0.13	4.08±1.00	4.51±0.12	4.69±0.07	4.42±0.09	4.14±0.12
Total	100.5±1.5	98.7±2.0	99.6±0.2	101.6±0.4	100.5±0.3	101.7±0.7	100.0±0.6	100.9±0.5	101.3±0.8

Figure 3.17, shows a region typical of all samples, containing a large amount of circular porosity, the amount of which was worst at the most severe solution treatment (longest time and highest temperature). Steps were taken to remove the large amount of porosity found in ARE415 alloy after heat treatment, by degassing the alloy melt prior to infiltration. However, this was unsuccessful, and considering that the porosity would have a deleterious effect on mechanical behaviour, the program of work using this alloy was reduced.

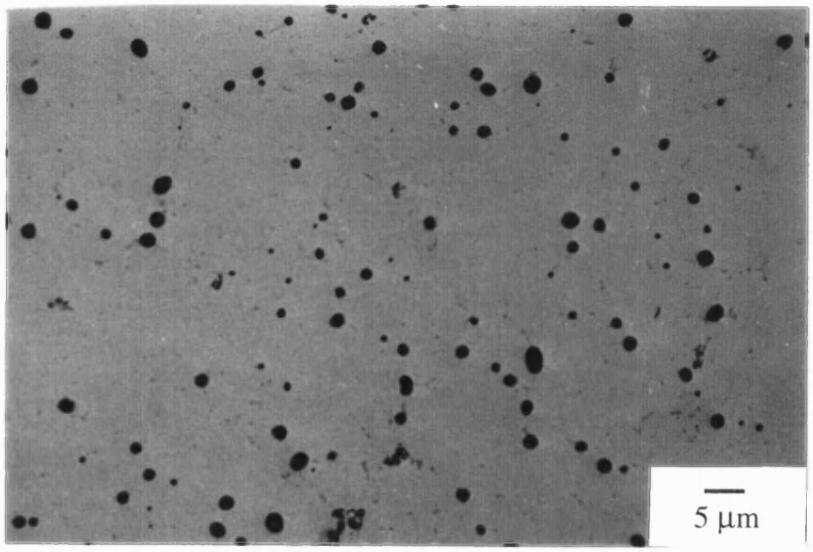

Figure 3.17 Porosity present in ARE415 alloy.

3.4.1(b) Mechanical Testing

A stress-strain curve is given in Figure 3.18. Values for Young's modulus, yield stress and failure strain derived from the curves are collated in Table 3.8, averaged results of 6 tests with 95% confidence limits. The alloy showed little sign of ductility (~1%), and the fracture surface was quite rough, as shown in Figure 3.19.

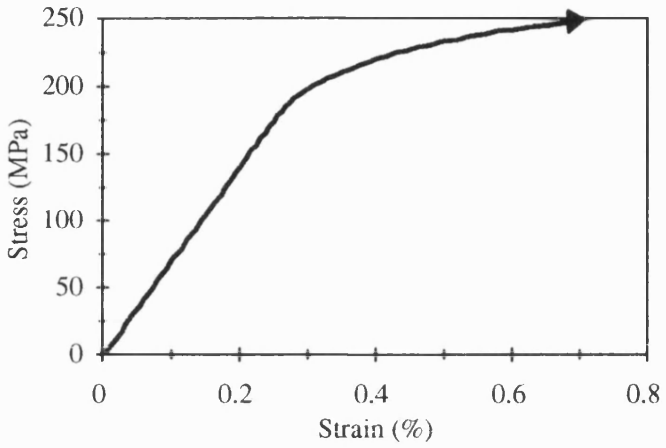

Figure 3.18 Tensile test on cast ARE415.

Table 3.8 Tensile properties, cast ARE415.

Young's modulus (GPa)	yield stress (MPa)	strain at yield (%)	tensile strength (MPa)	strain to failure (%)
70 ± 5	165 ± 25	0.24 ± 0.05	265 ± 20	1.1 ± 0.7

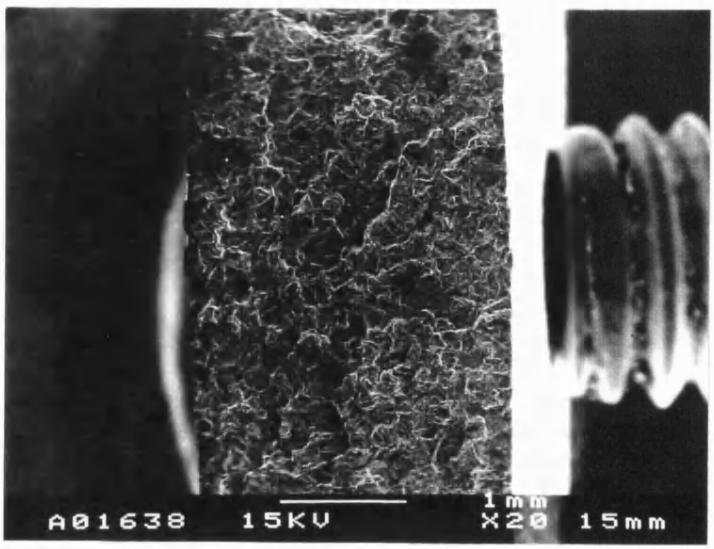

Figure 3.19 Tensile failure of cast ARE415.

3.4.2 Reinforced with Altex

3.4.2(a) Microstructure

(i)Cast

Light micrographs, Figures 3.20(a) and (b), show that the distribution of fibres is slightly uneven, with an average fibre volume fraction (V_f) of 0.44 ± 0.03. The figures also highlight the variation in fibre diameter, from 6 to 23μm, and averaging 16 ± 2 μm. Infiltration of the fibre by the liquid metal appears good, with matrix porosity of less than 1 vol.%. A second phase, 46.1 ± 1.0 wt.% Al and 48.6 ± 1.4 wt.% Cu identified as eutectic $CuAl_2$, is segregated to and bridging the fibres, indicating that these areas were the last to solidify. Electrochemical etching, Figure 3.20(c), reveals that in some cases the grain size is smaller than the unreinforced alloy, at 50-100μm, although where the fibres are widely dispersed the grain size is unaffected.

A TEM micrograph of the fibre/matrix interface is shown in Figure 3.21(a). EDS data from the fibre, fibre/matrix and matrix, Figures 3.21(b), (c) and (d) respectively, show that a small amount of magnesium has segregated to the surface of the fibre, although no visible evidence was found to suggest the formation of a reaction phase at the interface. The fibre has a fine crystalline structure, with crystals ~10nm in diameter. A diffraction pattern from the central region of the fibre, Figure 3.21(e), shows a series of concentric rings which may be indexed to show a cubic structure (a = 0.79nm), consistent with γ-alumina. A diffuse central ring is indicative of some amorphous phase.

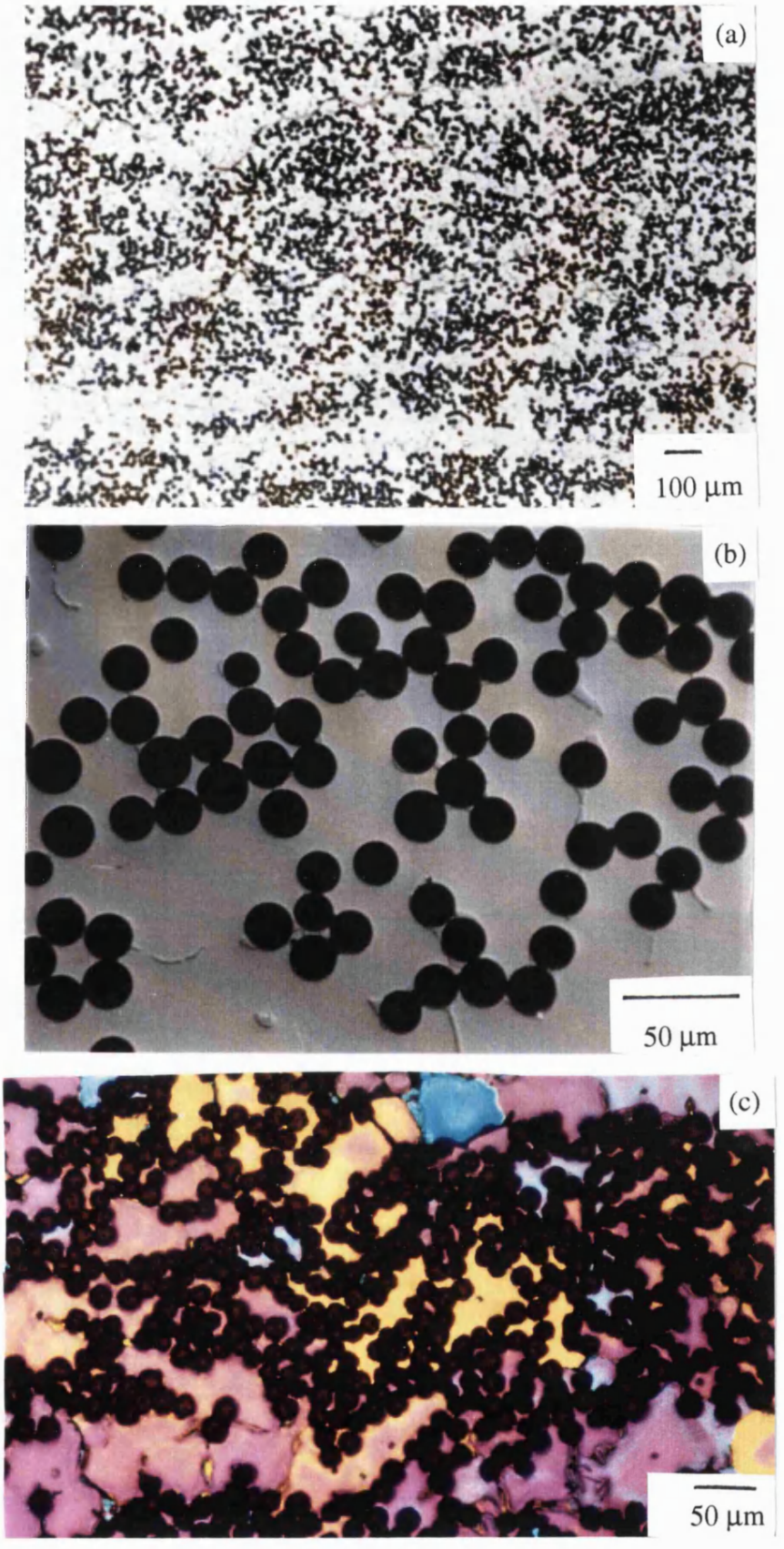

Figure 3.20 Altex reinforced ARE415:

(a) optical (b) optical; (c) optical, etched.

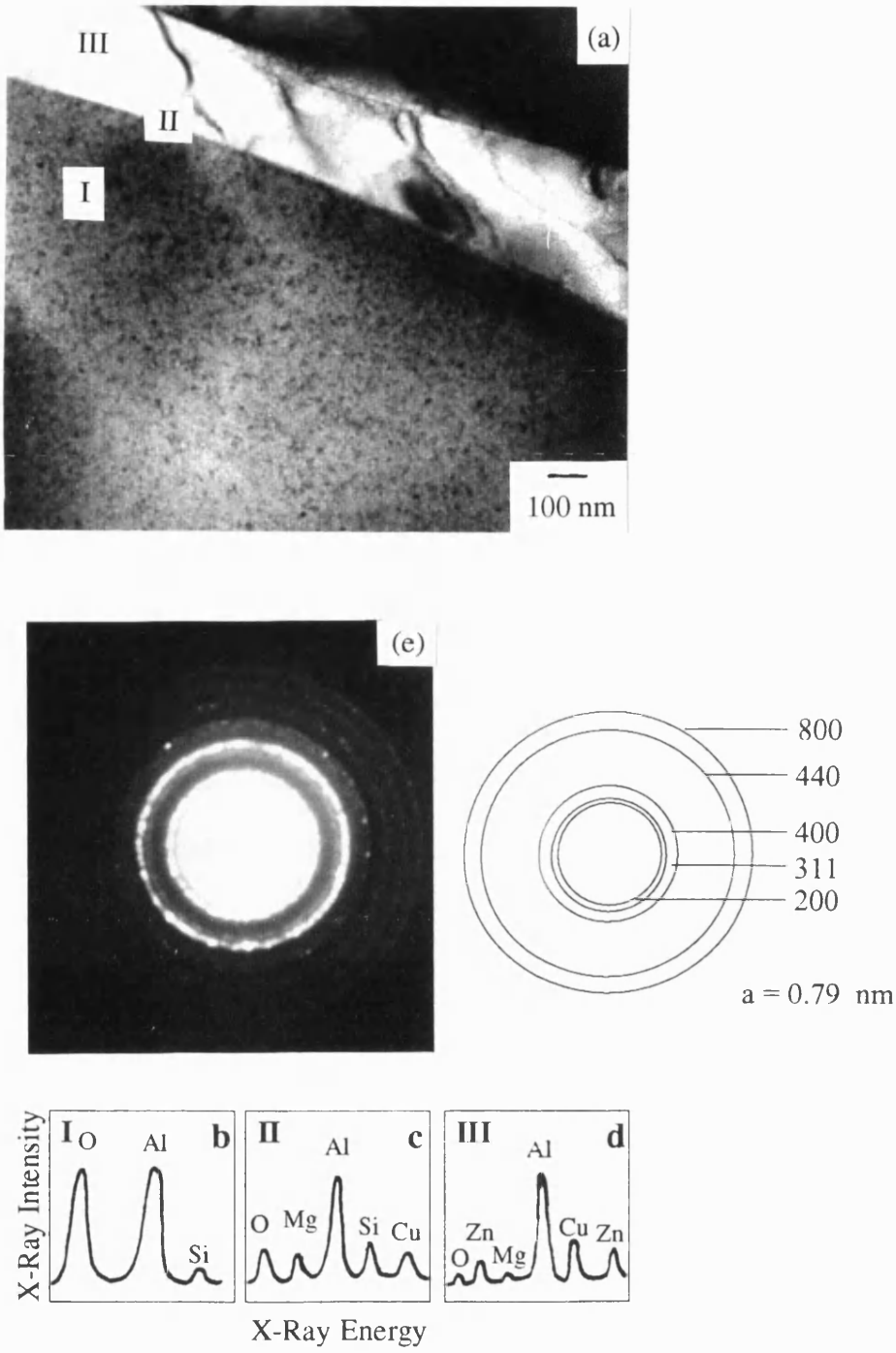

Figure 3.21 Thin foil of Altex reinforced ARE415 alloy:

(a) fibre/matrix interface region, TEM;

(b) EDS from fibre, region I;

(c) EDS from interface, region, II;

(d) EDS from matrix, region III;

(e) Diffraction pattern, region I, fibre.

(ii)Heat-Treated

EPMA from the matrix after various solution treatments is shown in Table 3.9. The solution treatment is effective in reducing the coring present in the cast condition. Figure 3.22, a micrograph for the 500°C for 6 hours and 540°C for 18 hours condition shows that most of the second phase has been dissolved, with only small iron and manganese containing intermetallics remaining. Again some porosity has appeared after solutionising, comparable with the unreinforced alloy.

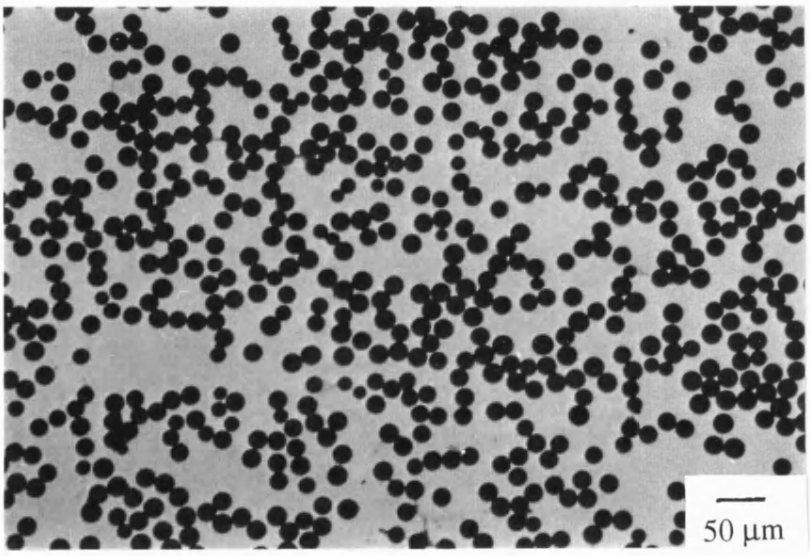

Figure 3.22 Solution treated Altex reinforced ARE415.

Table 3.9 Comparison of ZAF corrected wt.% data for Altex reinforced solution treated ARE415

Element	cast mid dendrite	cast dendrite edge	500°C 6 hours mid dendrite	500°C 6 hours 520°C 18 hours	500°C 6 hours 520°C 42 hours	500°C 6 hours 530°C 18 hours	500°C 6 hours 530°C 42 hours	500°C 6 hours 540°C 18 hours	500°C 6 hours 540°C 42 hours
Al	95.2±0.6	91.6±1.9	92.1±0.4	90.4±0.3	90.9±0.5	91.4±0.3	91.6±0.5	91.3±0.4	91.9±0.4
Cu	1.53±0.40	2.51±0.54	4.11±0.24	4.52±0.14	4.33±0.08	3.87±0.11	3.42±0.12	3.81±0.13	4.03±0.04
Mg	0.35±0.06	0.52±0.11	0.60±0.04	0.49±0.04	0.51±0.03	0.60±0.04	0.39±0.01	0.52±0.02	0.41±0.04
Ag	0.25±0.04	0.58±0.03	0.45±0.04	0.43±0.07	0.45±0.05	0.41±0.10	0.42±0.05	0.39±0.03	0.39±0.04
Zn	2.73±0.35	3.73±0.43	3.72±0.11	3.67±0.14	3.68±0.10	3.39±0.10	3.41±0.12	3.45±0.14	3.60±0.15
Total	100.1±0.4	98.7±1.3	100.9±0.5	99.7±0.4	99.6±0.5	100.1±0.4	100.7±0.4	100.4±0.5	100.8±0.5

Figure 3.23, shows a TEM micrograph of the fibre/matrix interface. EDS data from the fibre, interface and matrix, was no different to the cast condition, there was still a build up of magnesium at the interface. No evidence was found for the formation of any reaction phases at the interface, but some aluminium and copper precipitates appear to have nucleated at the fibre surface. Diffraction patterns from the central regions of the fibres, were the same as fibres in the cast composite.

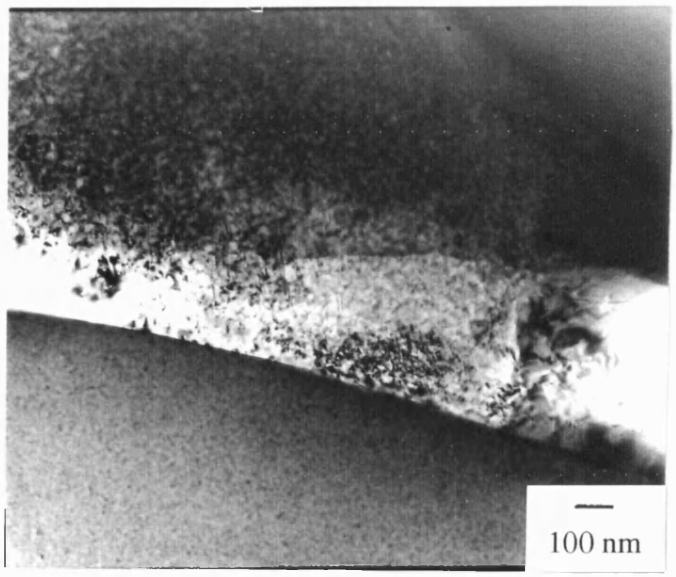

Figure 3.23 Thin foil of solution treated Altex reinforced ARE415.

3.4.2(b) Mechanical Testing

A stress-strain curve for the Altex reinforced alloy tested in longitudinal tension, Figure 3.24, shows a noticeable reduction of slope (arrowed), referred to as a 'knee-point'. This occurred at a stress of ~100 MPa and a corresponding strain of ~0.09 %. The tensile strength of the composite was found to be 300 MPa at a strain of ~0.4 %. Collated test data is given in Table 3.10; values for stress at the knee-point are referred to here as yield stress, for reasons to be given later.

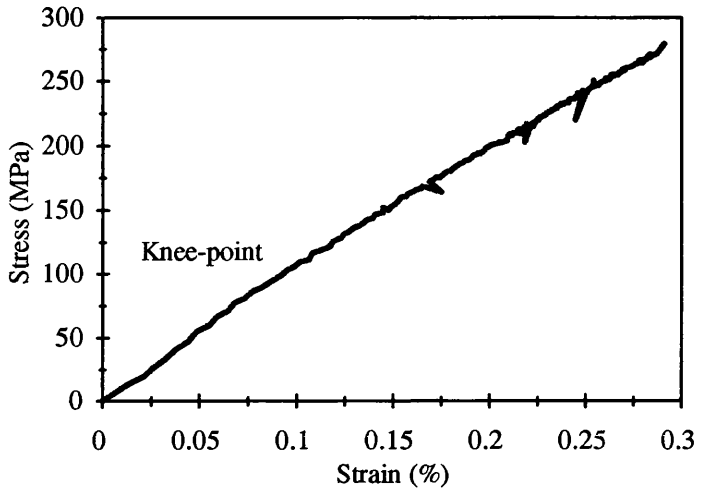

Figure 3.24 Tensile test on cast Altex/ARE415, longitudinal.

Table 3.10 Longitudinal tensile properties, cast Altex/ARE415

Young's modulus (GPa)	yield stress (MPa)	strain at yield point (%)	tensile strength (MPa)	strain at failure (%)
110 ± 20	100 ± 10	0.09 ± 0.03	300 ± 10	0.38 ± 0.06

Examination of the fracture surface, Figures 3.25(a) and (b), shows evidence of fibre pull-out and matrix yielding respectively. Figure 3.25(c), shows a fibre broken in several places along its length, with matrix metal adhering to the fibre surface, this is indicative of a strong fibre/matrix bond.

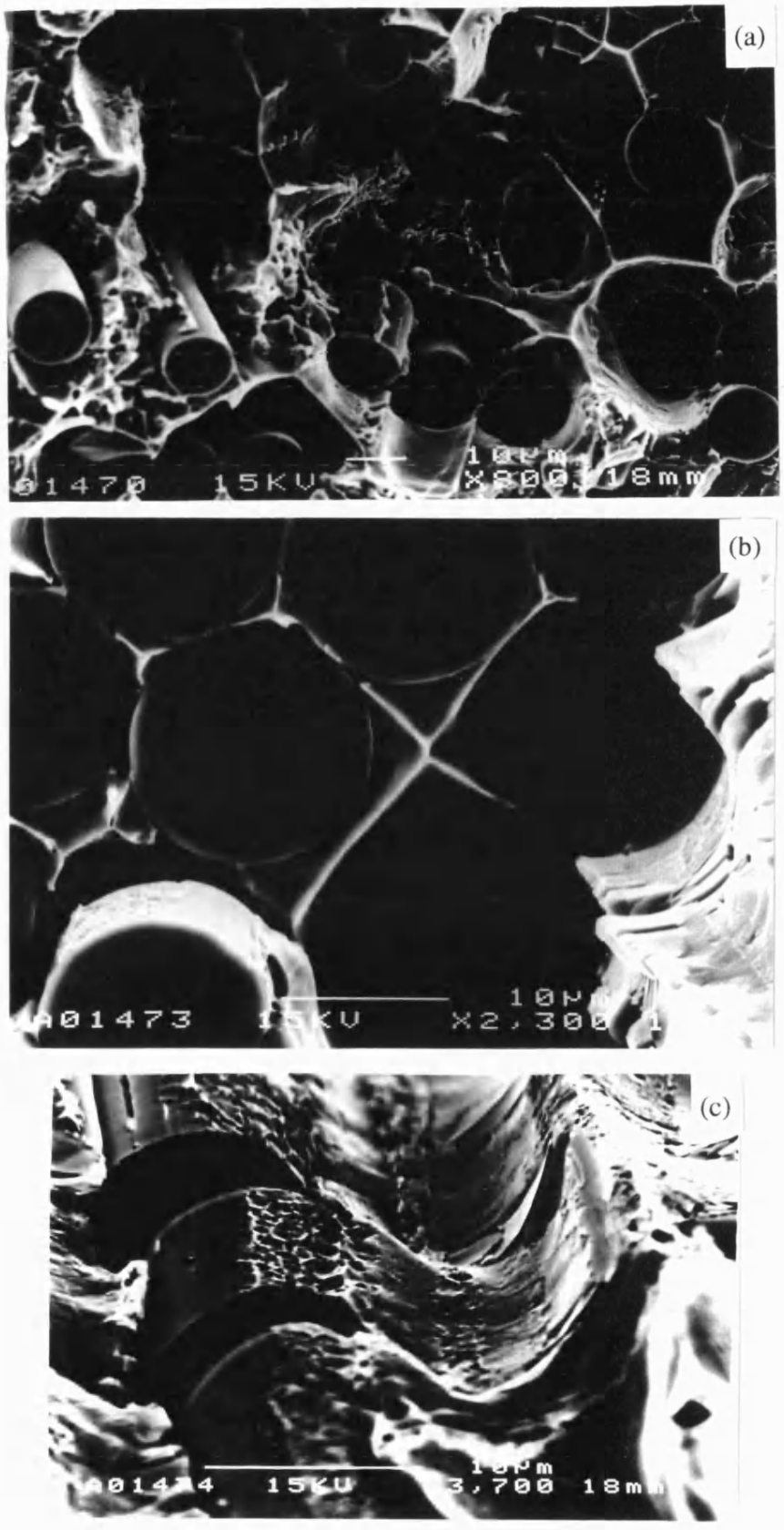

Figure 3.25 Tensile failure of longitudinal Altex/ARE415:

(a) region of pull-out; (b) area of matrix ductility;

(c) broken fibre showing matrix metal adhered to surface.

3.4.3 Reinforced with Nicalon

3.4.3(a) Microstructure

(i)Cast

Light and SEM micrographs, Figures 3.26(a) and (b), show a microstructure similar to that of the Altex reinforced composite. The distribution of fibres is slightly uneven, with an average V_f of 0.40 ± 0.05. Again there is a variation in the diameter of the fibres, between 7 and 21μm, but on average 12 ± 2μm. Infiltration of the fibres is high, with less than 1 vol.% of matrix porosity detected. The second phase is segregated to and bridging the fibres, and has the composition of 46.1 ± 1.0 wt.% Al and 48.6 ± 1.4 wt.% Cu, consistent with eutectic $CuAl_2$. Again etching reveals that where the fibres are closely spaced the grain size is reduced to the same extent as the Altex reinforced composite, Figure 3.26(c).

TEM studies of the fibre matrix interface, coupled with the EDS data from the fibre, fibre/matrix interface and matrix, Figures 3.27, show that a small amount of magnesium has segregated to the surface of the fibre. Some phases were found at the interface, from EDS, Figure 3.27(e), these are deduced as $CuAl_2$. The fibre has a very fine crystalline structure, with crystals a few nm in size. A diffraction pattern from the central region of the fibre, Figure 3.27(f), shows a series of rings which may be indexed to show a face-centred cubic structure (a = 0.436nm), consistent with β-silicon carbide. A diffuse central ring is indicative of some amorphous phase.

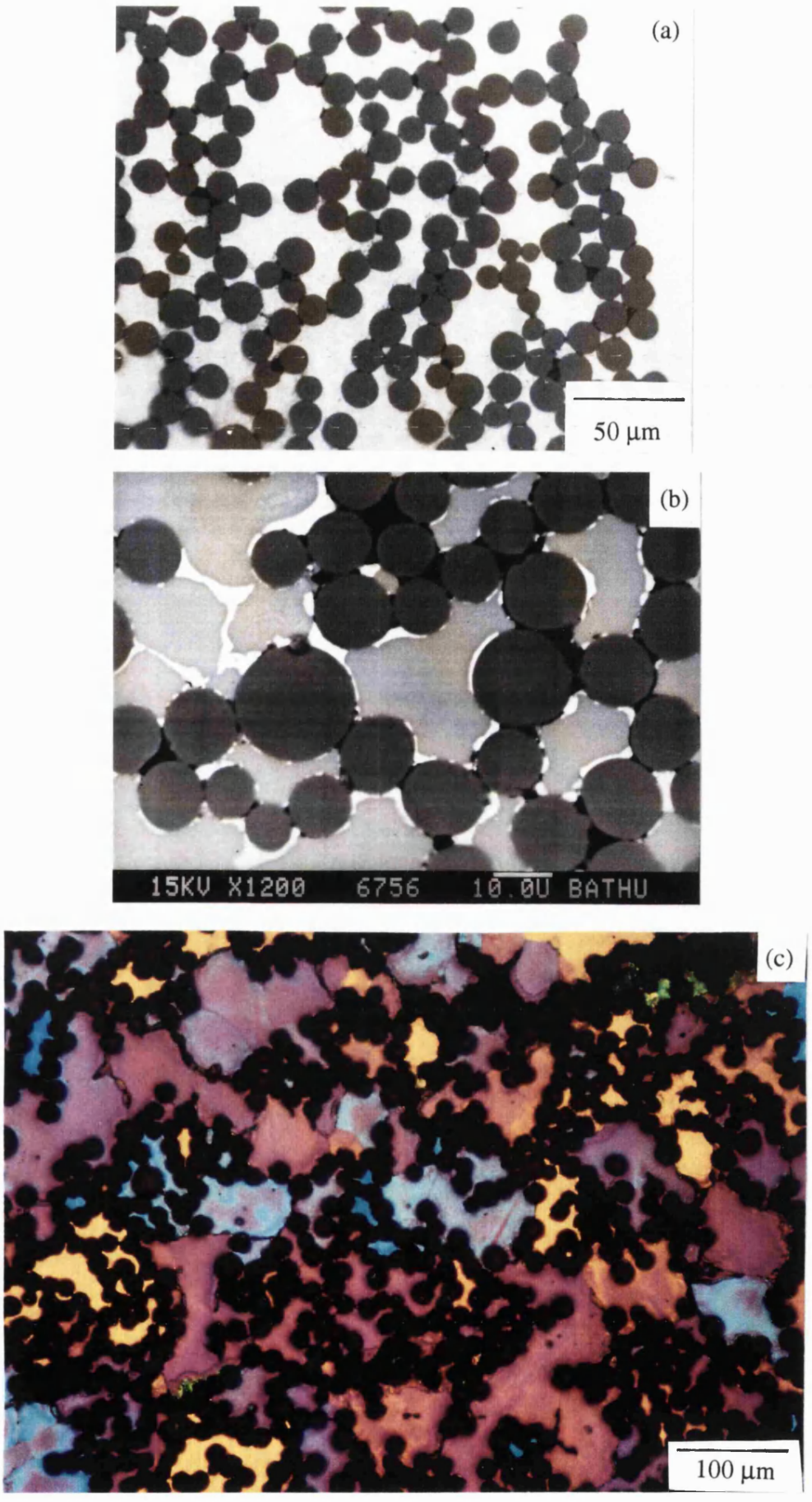

Figure 3.26 Nicalon reinforced ARE415: (a) optical; (b) SEM; (c) optical, etched.

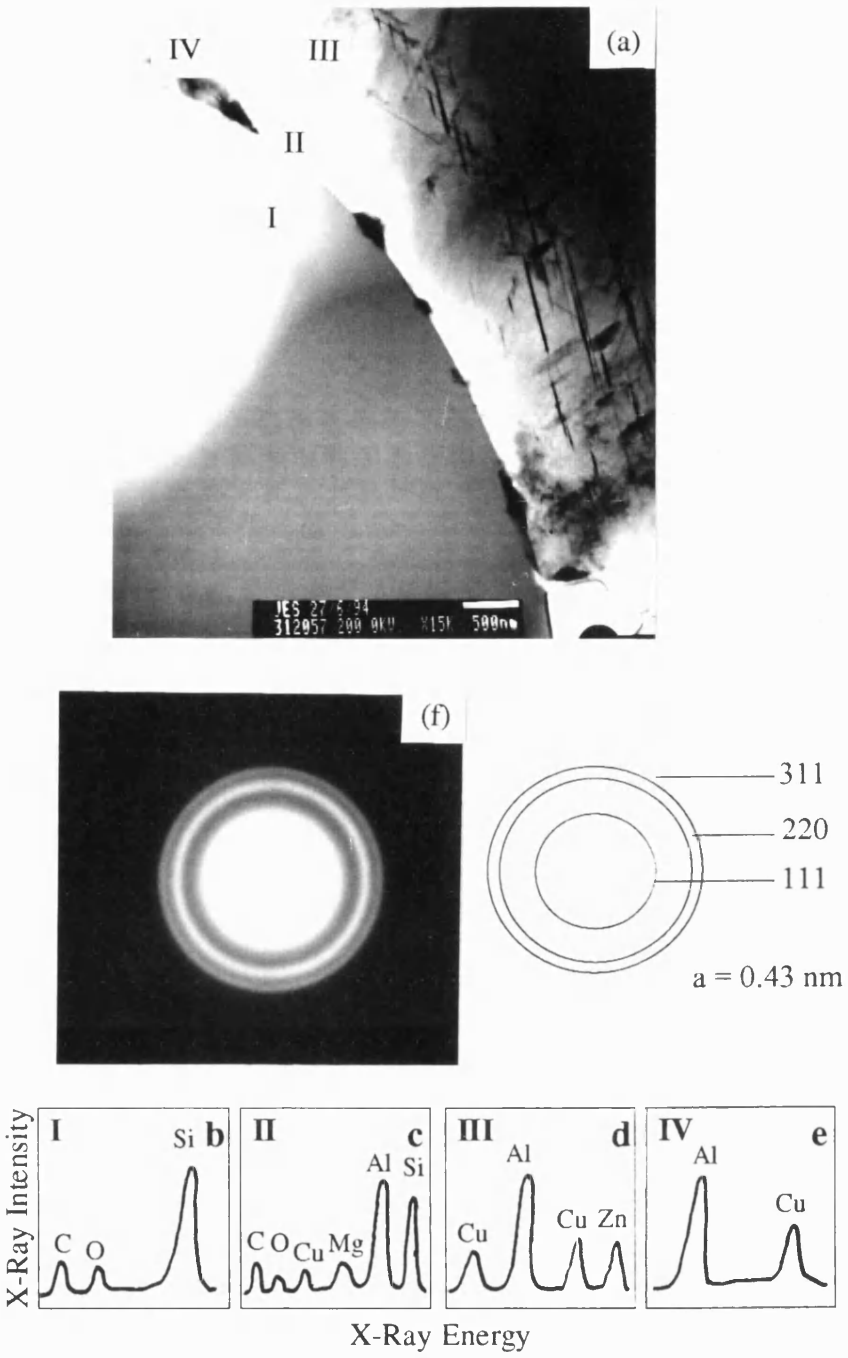

Figure 3.27 Thin foil of Nicalon reinforced ARE415:

(a) fibre/matrix interface region, TEM;

(b) EDS from fibre, region I;

(c) EDS from interface, region II;

(d) EDS from matrix, region III;

(e) EDS from second phase region IV;

(f) diffraction pattern, region I, fibre.

(ii)Heat-Treated

Table 3.11, shows EPMA data for the solutionised and cast composite. A decrease in magnesium and aluminium is observed with the increase in solution treatment temperature, and a corresponding increase in silicon content in the matrix. The matrix does not appear homogenised. Transverse and longitudinal sections are presented in Figures 3.28 and 3.29 respectively. These show a reaction layer within the original dimensions of the fibre and needles extending into the matrix. It is clear that the reaction occurs over the whole range of the sample and is not a localised effect.

Table 3.11 Comparison of ZAF corrected wt.% data for Nicalon reinforced solution treated ARE415

Element	**cast mid dendrite**	**500°C 6 hours**	**500°C 6 hours 520°C 42 hours**	**500°C 6 hours 530°C 42 hours**	**500°C 6 hours 540°C 42 hours**
Al	91.4±0.6	88.3±0.5	87.5±0.6	87.9±0.4	87.6±0.4
Cu	1.22±0.11	3.92±0.08	3.63±0.08	3.27±0.07	2.87±0.08
Mg	0.26±0.03	0.33±0.02	0.13±0.03	0.07±0.01	0.13±0.02
Ag	0.24±0.02	0.42±0.03	0.37±0.03	0.39±0.03	0.37±0.02
Zn	3.56±0.20	4.74±0.06	4.80±0.09	4.59±0.07	4.39±0.07
Si	0.47±0.32	1.12±0.29	1.37±0.12	2.01±0.14	2.71±0.31
Total	97.6±0.6	99.4±0.3	98.2±0.7	98.6±0.4	98.7±0.7

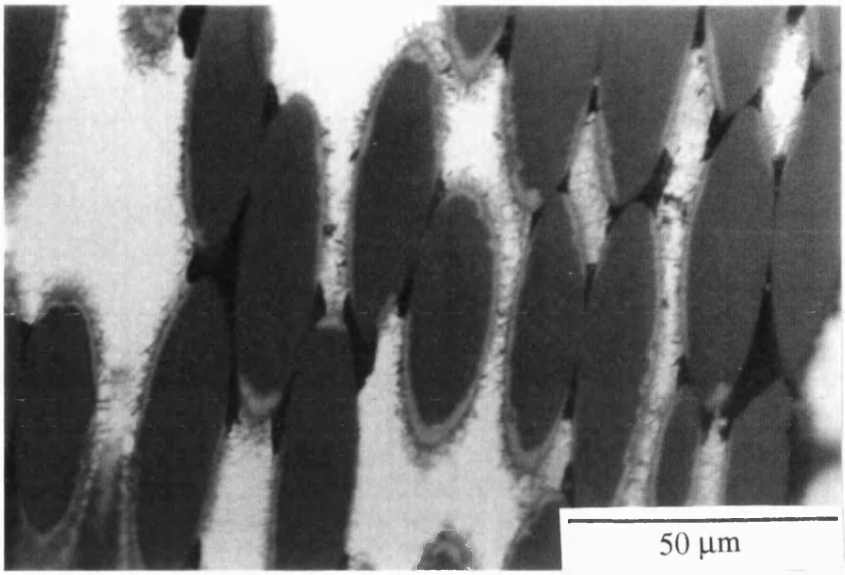

Figure 3.28 Reaction layer in fibres of solutionised Nicalon/ARE415

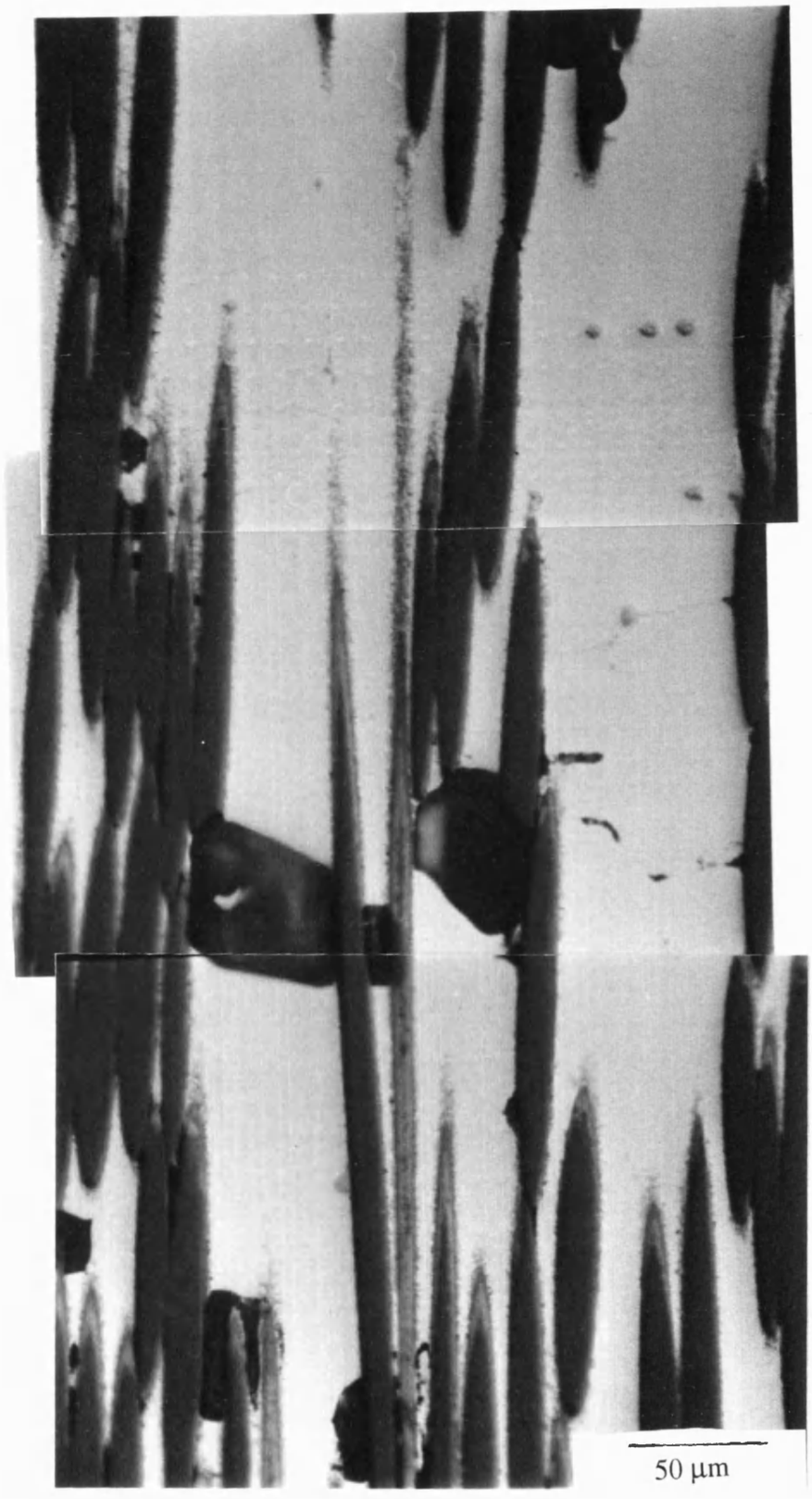

Figure 3.29 Reaction layer in fibres of solutionised Nicalon/ARE415

In addition to the fibre/matrix reaction, three new second phases are observed, Figures 3.30(a-c). The first phase, Figure 3.30(a), appears bulky and rounded, EDS analysis of this phase revealed aluminium, copper, silicon, iron and manganese. The second phase, Figure 3.30(b), has an angular morphology, EDS showed aluminium, silicon, manganese, iron, copper and small amounts of oxygen. The third phase is circular in appearance, Figure 3.30(c), and contained aluminium, silicon, copper, zinc, oxygen, and carbon. No reliable EPMA data could be obtained. The rounded morphology of the phases suggests some form of melting during the treatment. Holes have formed as in the unreinforced alloy.

A TEM micrograph of the fibre/matrix interface, Figure 3.31(a), shows a reaction layer ~200nm thick. Diffraction patterns from the fibre core were the same as fibres from the cast composite. Diffraction patterns from the reacted region of the fibre, Figure 3.31(b), show, however, sharper rings with spots. This indicates larger crystal size than the unreacted fibre, although the diffuse central region again indicates the presence of amorphous material. Unlike the cast condition the pattern does not correspond to β-silicon carbide, aluminium is the closest match. An EDS trace from the reacted region, Figure 3.31(c), confirms the presence of aluminium and magnesium in addition to the fibre constituents. EDS traces from the phases on the fibre, Figures 3.31(d-f), indicate $CuAl_2$, aluminium, copper, magnesium and silicon intermetallics, and aluminium, copper, manganese, iron and silicon intermetallics. A needle growing from the fibre is imaged in Figure 3.32, the spacing of the interference fringes, ≈0.83 nm, corresponding to Al_4C_3. Figure 3.33 shows precipitates in the matrix, perpendicular to each other, indicative of θ type.

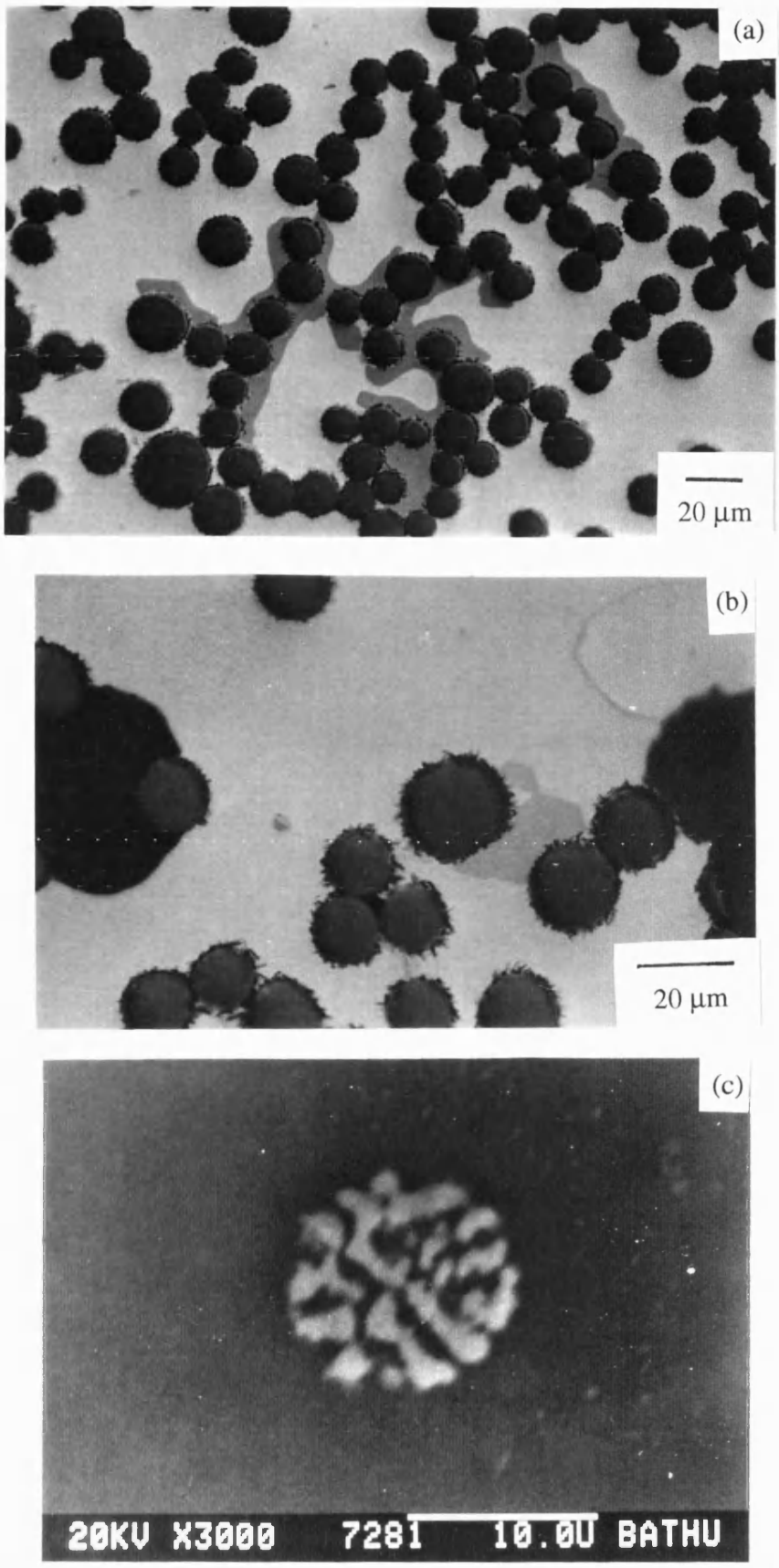

Figure 3.30 Second phases present after solutionising Nicalon/ARE415:

(a) optical; (b) optical; (c) SEM.

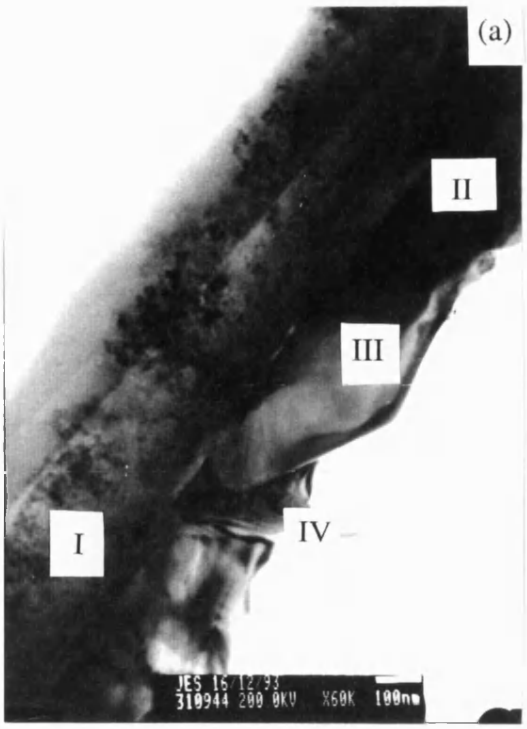

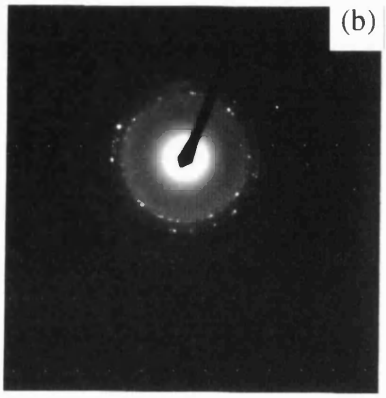

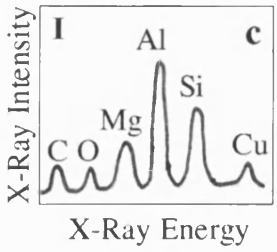

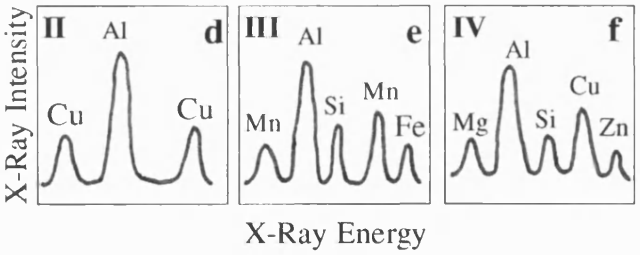

Figure 3.31 Thin section of solution treated Nicalon/ARE415:

(a) fibre/matrix interface section, TEM;

(b) diffraction pattern, fibre region I;

(c) EDS from reacted fibre, region I;

(d) EDS from reaction product II;

(e) EDS from reaction product III;

(f) EDS from reaction product IV.

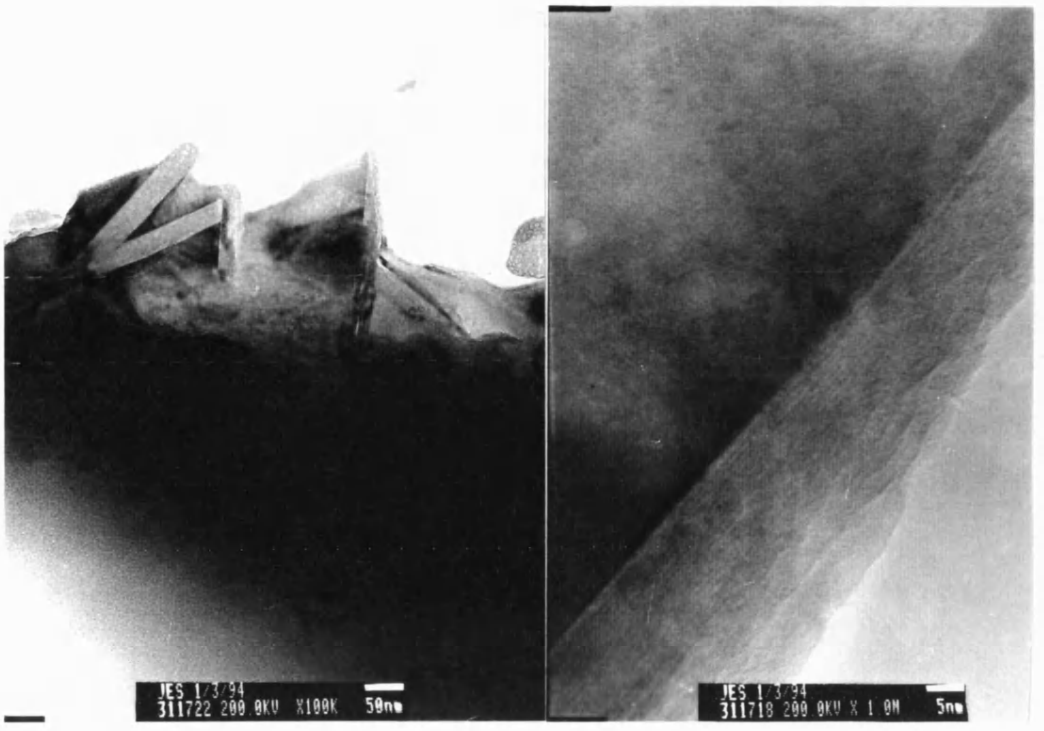

Figure 3.32 Needle from solutionised Nicalon/ARE415.

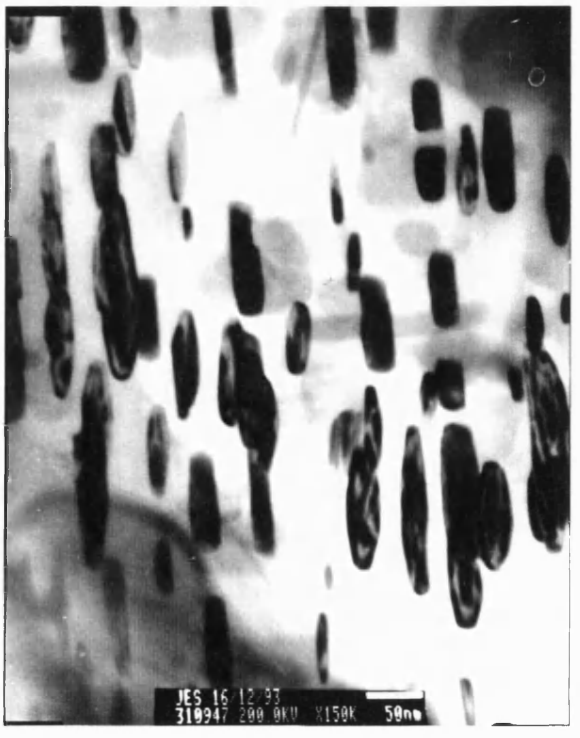

Figure 3.33 Precipitation in Solutionised Nicalon/ARE415.

3.4.4 Reinforced with Sigma

3.4.4(a) Microstructure

(i)Cast

A light micrograph from the Sigma reinforced ARE415 alloy, Figure 3.34, shows touching fibres, many of which appear to have been damaged. There is widespread cracking observed at both the fibre/matrix interface and along the intermetallic regions. SEM analysis, Figure 3.35, shows an extensive build up of intermetallic on one side of the reinforced region, labelled I. EDS performed on the matrix on the side opposite to the build up of intermetallic, labelled II, revealed only aluminium, suggesting strong segregation of solute.

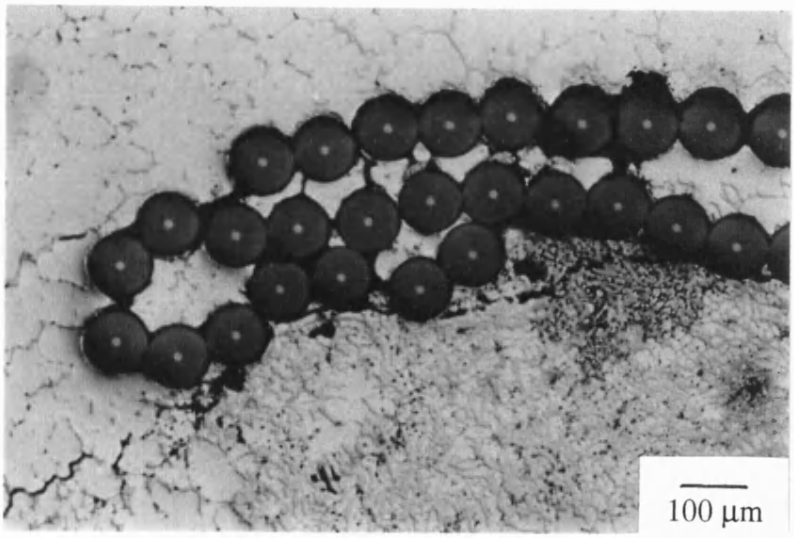

Figure 3.34 Light micrograph of Sigma reinforced ARE415.

Two different morphologies of second phase were observed in region I, a bulky phase and a thin needle-like phase. EDS on the bulky phase revealed the presence of copper and aluminium, indicative of $CuAl_2$. The needle-like phase also contained, in addition, iron and manganese. Quantitative analysis was not performed as the composite was deemed of poor quality.

Figures 3.35(a) and (b) show a back-scattered SEM image of the fibre/matrix interface and EDS trace from the dark uninfiltrated area, region I. The EDS trace reveals carbon, oxygen and silicon indicating an organic phase. Thermogravimetric analysis (TGA) was subsequently performed on the fibre and graphs of time versus: temperature, percentage weight loss (TG) and rate of change of weight loss (DTG), are shown in Figure 3.36. Weight losses are observed of ~7% at 350°C and a further 3% at ~525°C, followed by a slight weight gain. Visual observation of the fibres after TGA showed them to be discoloured black, with the tape and hence fibre alignment gone. SEM analysis revealed that almost all of the binder had been removed, with EDS showing only silicon and carbon on the fibre surface, Figure 3.37(a) and (b) respectively.

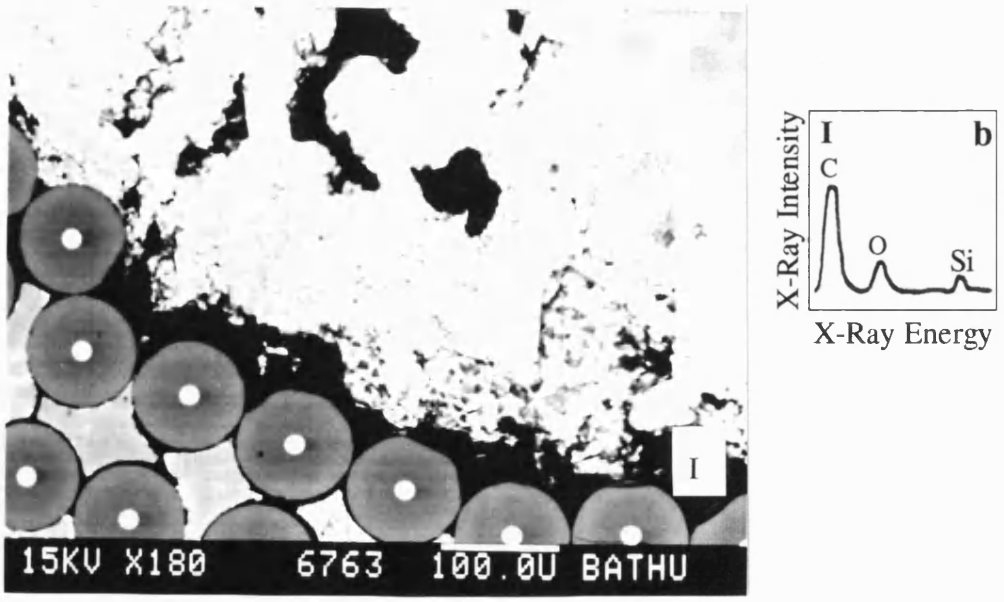

Figure 3.35 Sigma reinforced ARE415:

(a) back-scattered electron image; (b) EDS trace from region I.

Figure 3.36 Thermogravimetric analysis of Sigma monofilament heated in air.

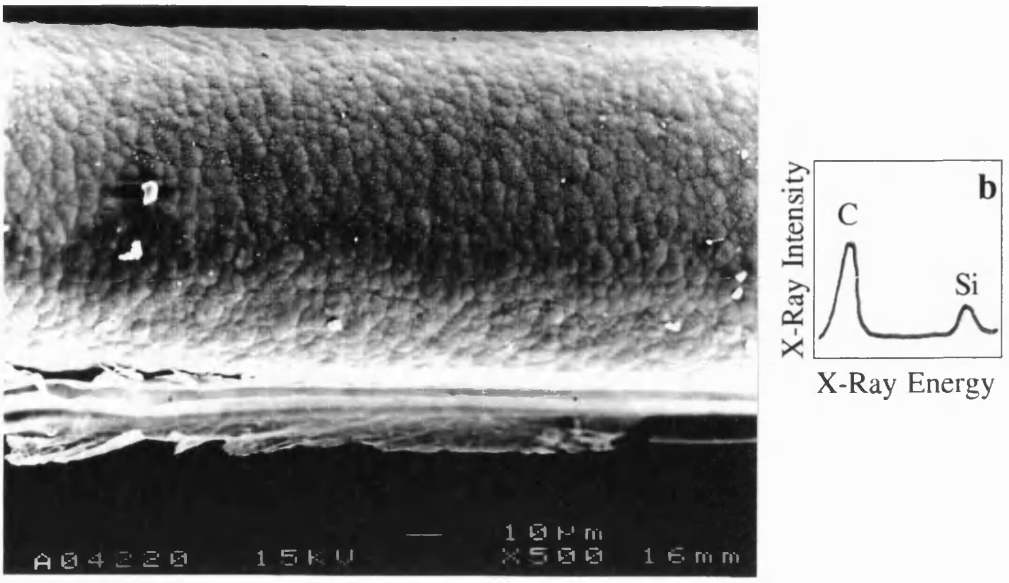

Figure 3.37 Sigma fibre after TGA: (a) SEM micrograph;
(b) EDS from monofilament.

3.5 Microstructure & Mechanical Testing of A201 Alloy Systems

Many structural features were the same as in the ARE415 alloy systems, especially fibre data.

3.5.1 Unreinforced

3.5.1(a) Microstructure

(i)Cast

A back-scattered electron image of the cast alloy, Figure 3.38(a), shows a typical cast structure. Further detail was revealed by electrochemical etching, Figures 3.38(b) and (c), showing coarse (~300µm) grains, with cored dendrites (~10µm), and an interdendritic second phase. Using EDS, the second phases were identified as $CuAl_2$ or a mixture of copper, aluminium and iron. Image analysis indicated that ~7 vol.% of second phase was present, with less than 1 vol.% of porosity.

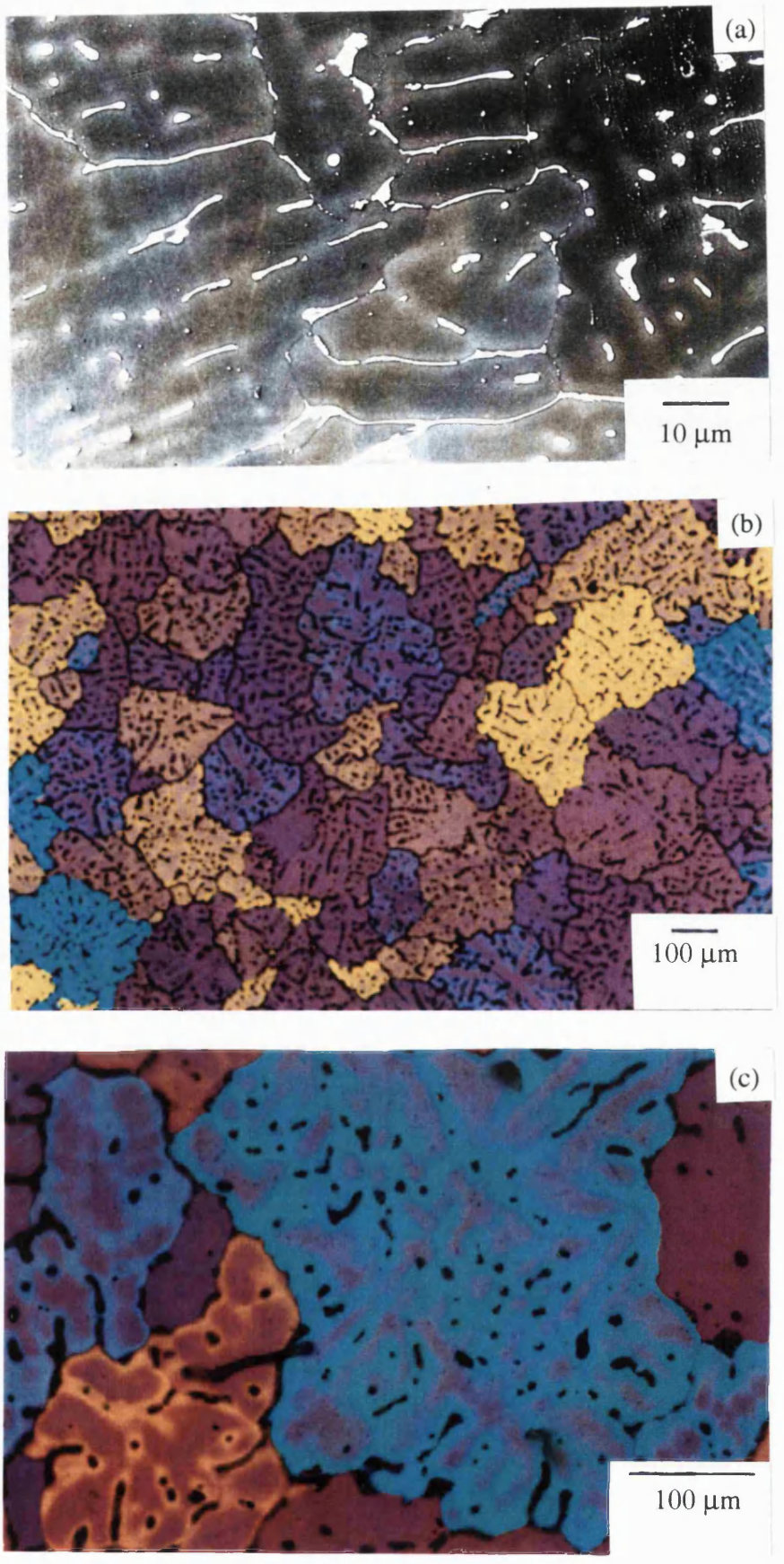

Figure 3.38 Unreinforced A201: (a) back-scattered electron image; (b) optical, etched; (c) optical, etched.

TEM analysis showed that some precipitation had occurred during manufacture. The precipitation was very patchy showing both fine and coarse precipitates and in some areas none. Figures 3.39(a) and (b), show a region of precipitation in the matrix and the corresponding EDS trace respectively. The EDS trace shows the presence of copper and aluminium, indicative of θ-$CuAl_2$ type precipitates.

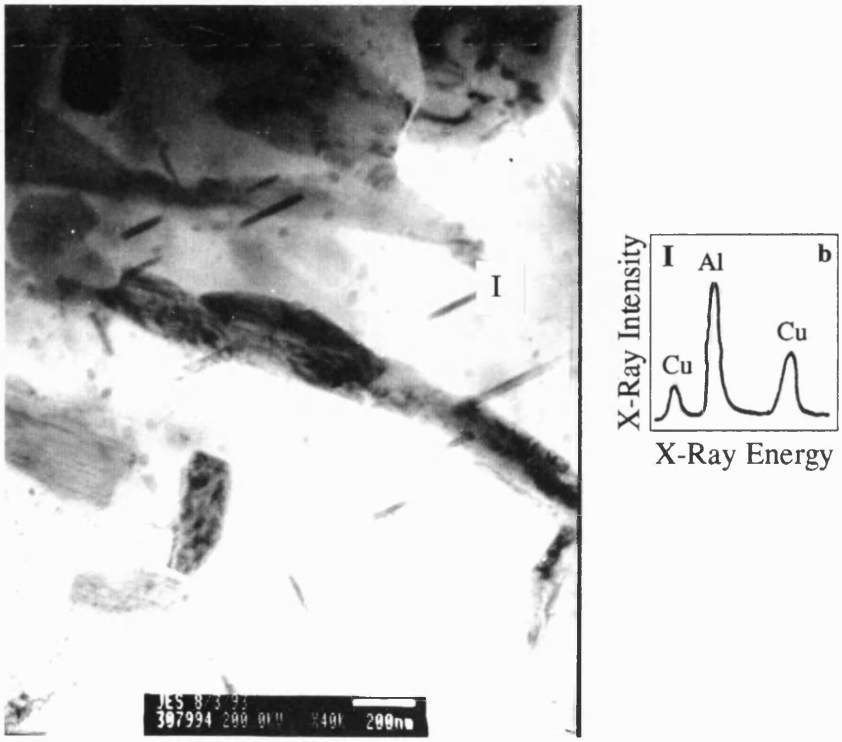

Figure 3.39 Thin foil of unreinforced A201:

(a) Region of precipitation, TEM;

(b) EDS from precipitates, region I.

(ii)Heat-Treated

The solution treatment developed for the ARE415 alloy, 500 ±5°C for 6 hours and 530 ±5°C for 18 hours, was also used for the A201 alloy. EPMA work, Table 3.12, confirms that the matrix has been homogenised.

Table 3.12 Comparison of ZAF corrected wt.% data for solution treated A201.

Element	cast mid dendrite	cast dendrite edge	500°C 6 hours 530°C 18 hours
Al	98.2 ± 1.4	95.6 ± 1.2	91.9 ± 1.5
Cu	1.83 ± 0.59	4.03 ± 0.71	5.04 ± 0.15
Mg	0.11 ± 0.04	0.31 ± 0.05	0.23 ± 0.04
Ag	0.30 ± 0.04	0.78 ± 0.17	0.15 ± 0.02
Mn	0.31 ± 0.05	0.36 ± 0.03	0.22 ± 0.02
Total	100.8 ± 1.6	101.2 ± 0.9	98.1 ±1.5

After solution treatment, the amount of $CuAl_2$ phase was reduced to ~1 vol.%, and the coring was removed. The microstructure is shown in Figure 3.40. The phases were too small for quantitative analysis, but EDS revealed the presence of iron and manganese. There was no recurrence of the increased levels of porosity associated with the solution treated ARE415 alloy.

Figure 3.40 Solution treated A201 alloy.

Ageing was carried in an air atmosphere at 170°C in a muffle furnace. TEM studies were then performed on the peak-aged and over-aged (1000 hours) samples.

Upon ageing the hardness was found to increase from ~120 HV to a peak of 155 ± 4 HV after 7 hours, Figure 3.41. The hardness remains at this level until over 100 hours after which there is a small decline in hardness, as the time axis is plotted using a log scale this shows the precipitate to have good stability.

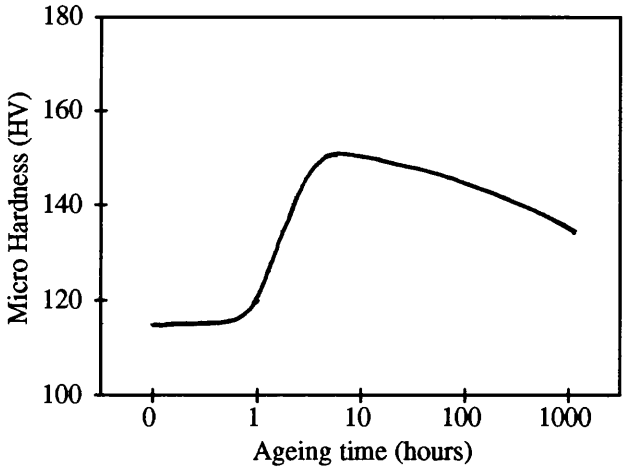

Figure 3.41 Microhardness versus ageing time at 170°C, A201.

TEM analysis of the peak-aged alloy reveals the presence of fine precipitates, Figure 3.42. The precipitates are >10 nm thick and between 50 and 100 nm long with an estimated density of $1x10^{21}$ m^{-3}. Figures 3.43 and 3.44 show precipitates and the corresponding indexed diffraction pattern from the $[1\bar{1}0]$ beam direction respectively. Analysis indicates the presence of θ' and Ω precipitates. EDS indicated that the precipitates contained aluminium and copper, with traces of magnesium and silver at the Ω precipitate/matrix interface.

Figure 3.42 Precipitates from the peak-aged A201 alloy.

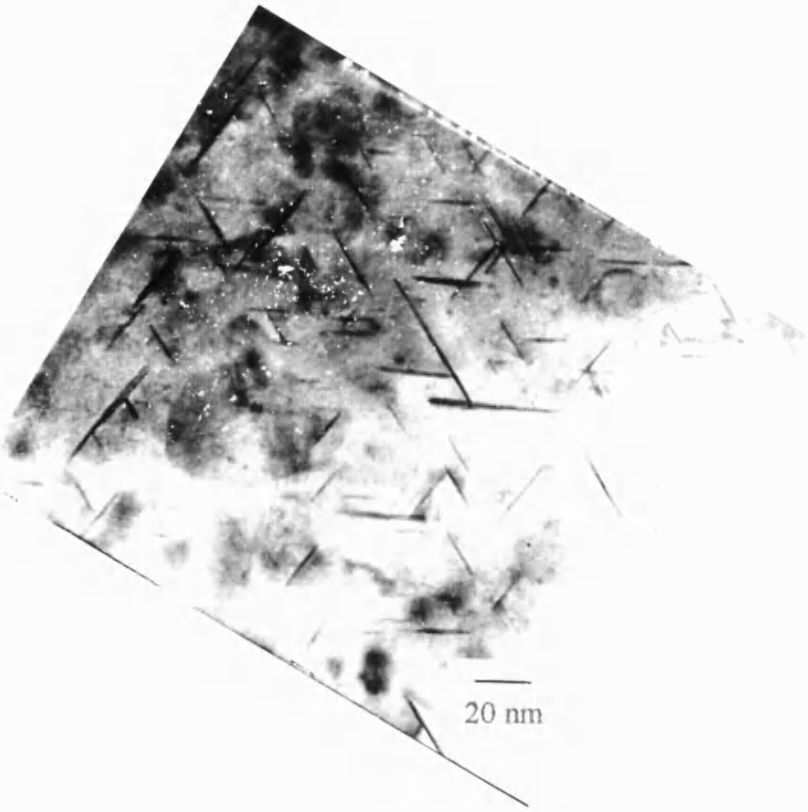

Figure 3.43 Precipitates from the peak-aged A201 alloy, [1 $\bar{1}$ 0] beam direction.

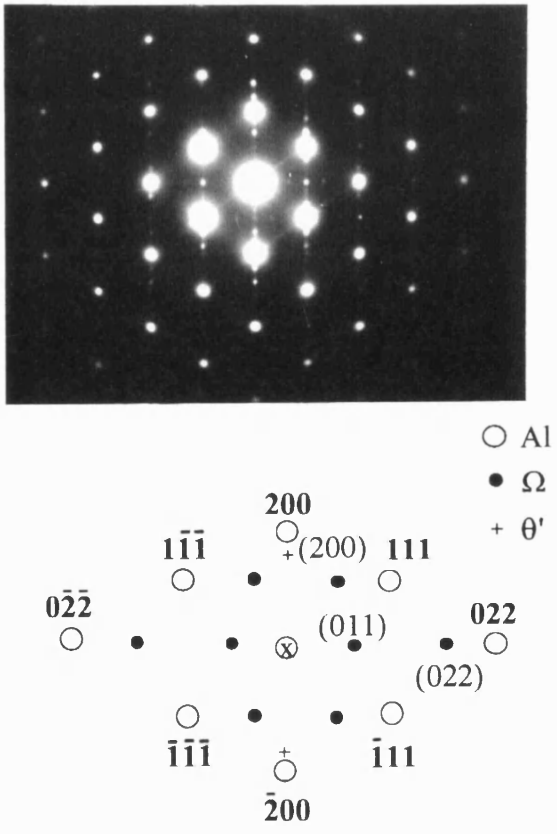

Figure 3.44 Indexed diffraction pattern, [1 $\bar{1}$ 0] beam direction.

Precipitation in the over-aged condition is very similar to that of the peak-aged condition, even after 1000 hours the precipitates are ~10 nm thick and between 100-150 nm long, Figure 3.45. Diffraction analysis of the precipitates showed no difference to those found in the peak-aged condition, with the precipitate density deduced to be ~ 2 x 10^{21} m^{-3}, Ω, and ~ 3 x 10^{20} m^{-3}, θ'.

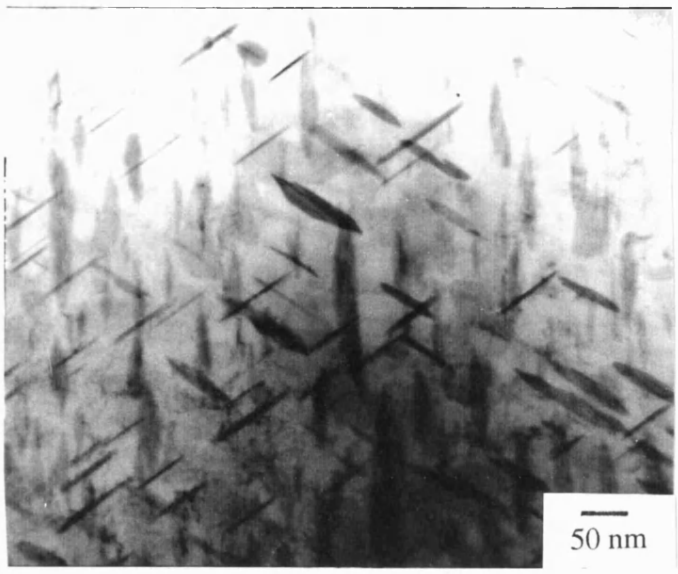

Figure 3.45 Precipitates from over-aged A201.

3.5.1(b) Mechanical Testing

Stress-strain curves for the cast, peak-aged and over-aged alloy are given in Figure 3.46. Values for Young's modulus, yield stress and failure strain derived from the curves are collated in Table 3.13, averaged results of 6 tests with 95% confidence limits.

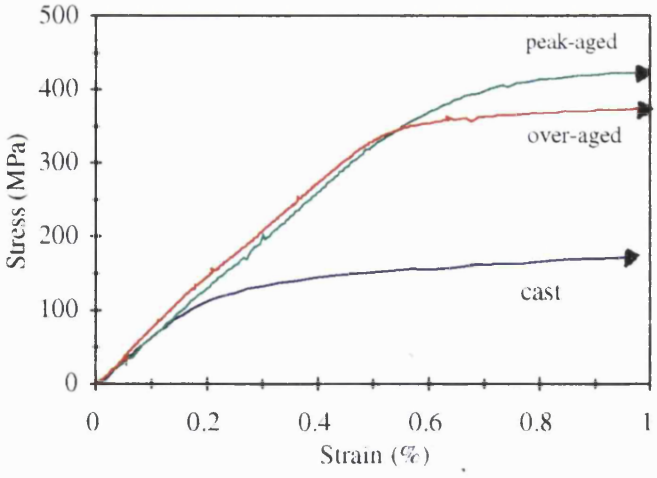

Figure 3.46 Tensile test on A201.

Table 3.13 Tensile test data, unreinforced A201.

condition	Young's modulus (GPa)	yield stress (MPa)	strain at yield (%)	tensile strength (MPa)	strain to failure (%)
cast	73 ± 3	96 ± 5	0.13 ± 0.01	267 ± 6	14.5 ± 1.3
peak-aged	69 ± 5	293 ± 46	0.42 ± 0.08	448 ± 29	4.6 ± 1.2
over-aged	79 ± 6	156 ± 16	0.19 ± 0.02	421 ± 25	4.8 ± 1.2

It can be seen that the modulus is unaffected by heat-treatment and is ~70 GPa for all conditions. The yield stress increases from ~96 MPa in the cast condition, to ~293 MPa in the peak-aged condition, further ageing causes the yield stress to fall to ~ 156 MPa in the over-aged condition. The strain at yield also falls after over-ageing from 0.42 % at peak-aged to 0.19 %. The tensile strength was found to increase from 267 MPa to 448 MPa after heat treatment, with a slight fall to 421 MPa after over-ageing. In the cast condition the alloy is very ductile with a failure strain of ~14.5 %, the alloy loses some of this ductility on ageing, the failure strain falling to 4.6 %, with little change after over-ageing.

The test piece surface was found to exhibit an 'orange peel' type finish after testing, for all the different conditions, this can be seen in Figure 3.47. The fracture surfaces for the cast and peak-aged samples are shown if Figure 3.48 (the over-aged fracture surface is indistinguishable from the peak-aged sample). The cast fracture surface appears much more ductile than the peak-aged sample, which although has some areas of ductility also shows smooth areas corresponding to a more brittle failure.

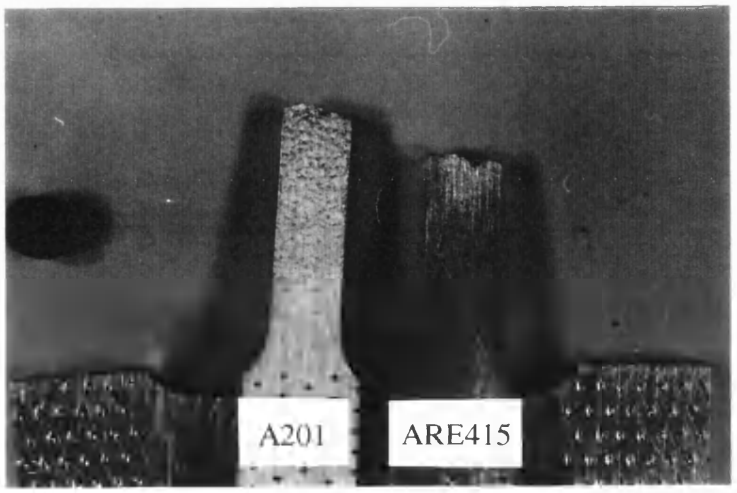

Figure 3.47 Surface of A201 and ARE415 alloys after tensile testing.

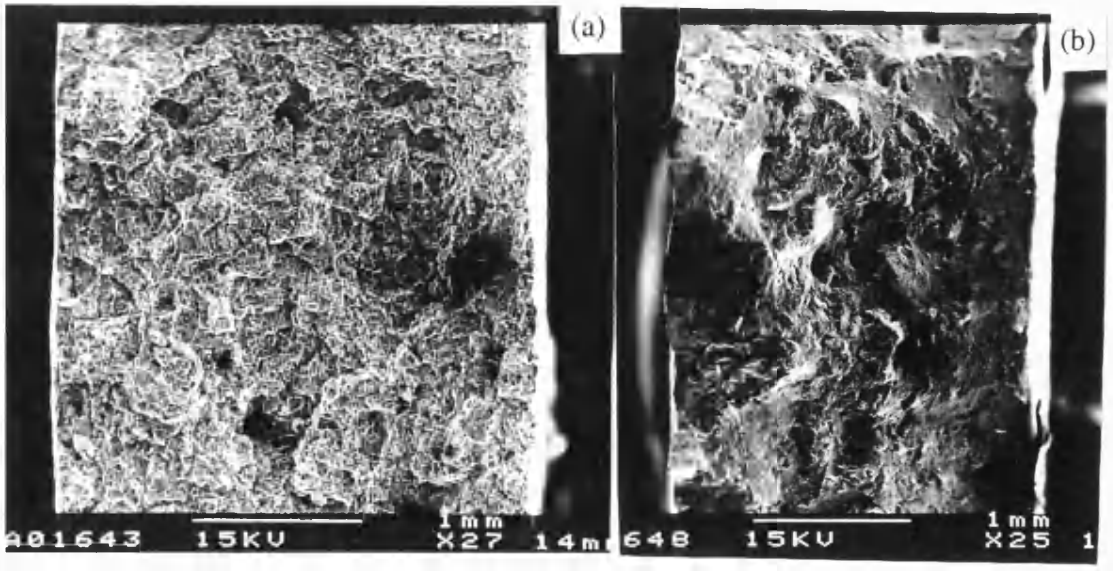

Figure 3.48 Tensile failure of A201: (a) cast;(b) peak-aged.

3.5.2 Reinforced with Altex

3.5.2(a) Microstructure

(i)Cast

Transverse sections through the cast composite were similar to the Altex/ARE415 composite, Figures 3.49(a) and (b), show that infiltration of the fibres by the liquid metal was good with a matrix porosity below 1 vol.%. The fibre volume fraction was 0.46 ± 0.03, although the distribution of fibres was somewhat uneven. Etching the sample, Figure 3.49(c), reveals the mean grain size of the particles to be ~300μm, not noticeably different from that in the unreinforced alloy. Coarse particles present around the fibres, Figure 3.50, were identified as 46.1 ± 0.9 wt.% Al and 48.6 ± 1.3 wt.% Cu, close to the composition of eutectic $CuAl_2$. Figure 3.50 also highlights the incidence of porosity at touching fibres.

A TEM micrograph of the fibre/matrix interface is shown in Figure 3.51(a). EDS data from the fibre, fibre/matrix interface and matrix, Figures 3.51(b-d), show that a small amount of magnesium has segregated to the surface of the fibre, although no evidence was found to suggest a reaction at the interface. Diffraction patterns from the central regions of the fibres, were the same as fibres in the Altex/ARE415 composite.

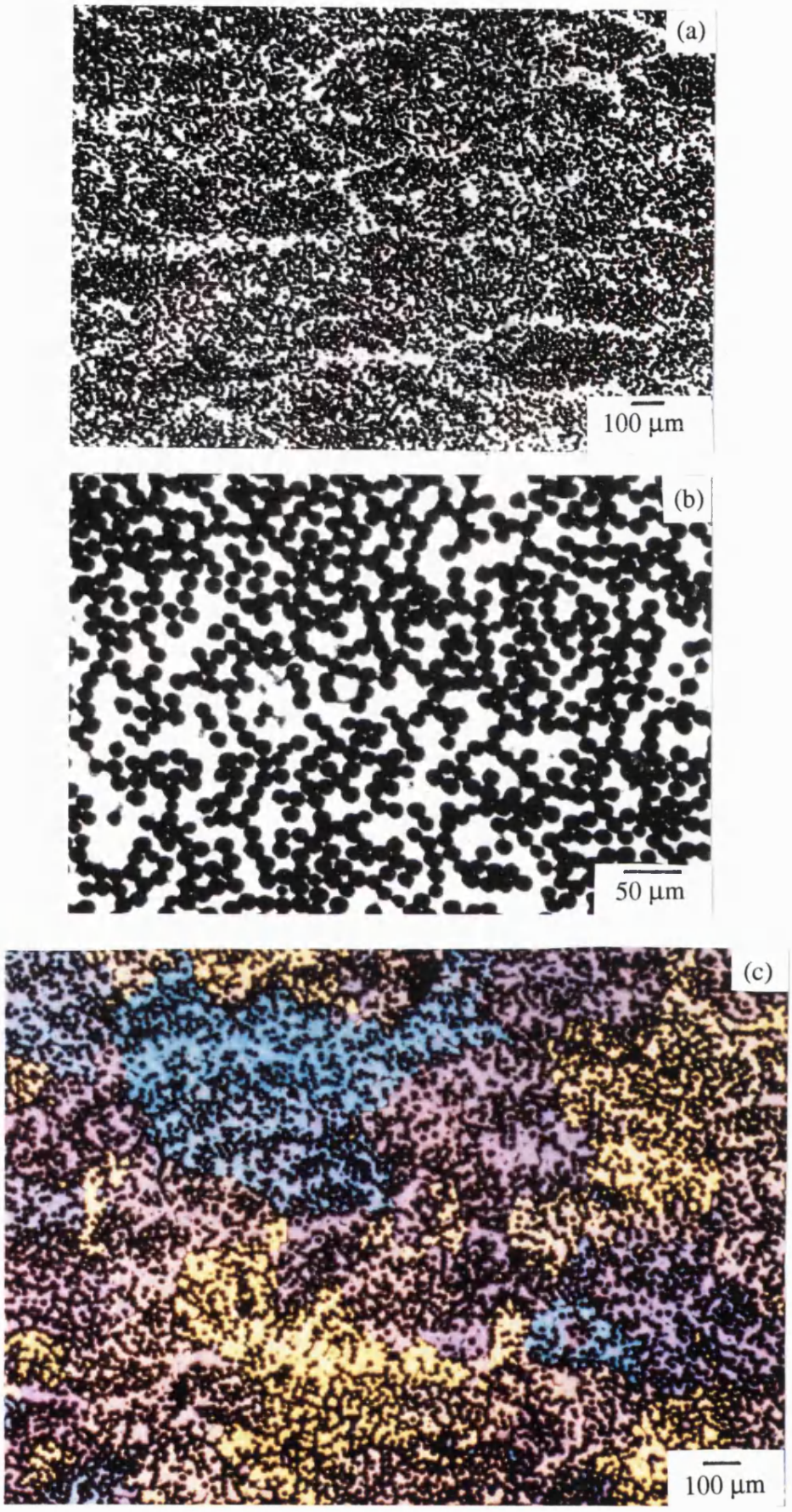

Figure 3.49 Altex reinforced A201: (a) optical; (b) optical; (c) optical, etched.

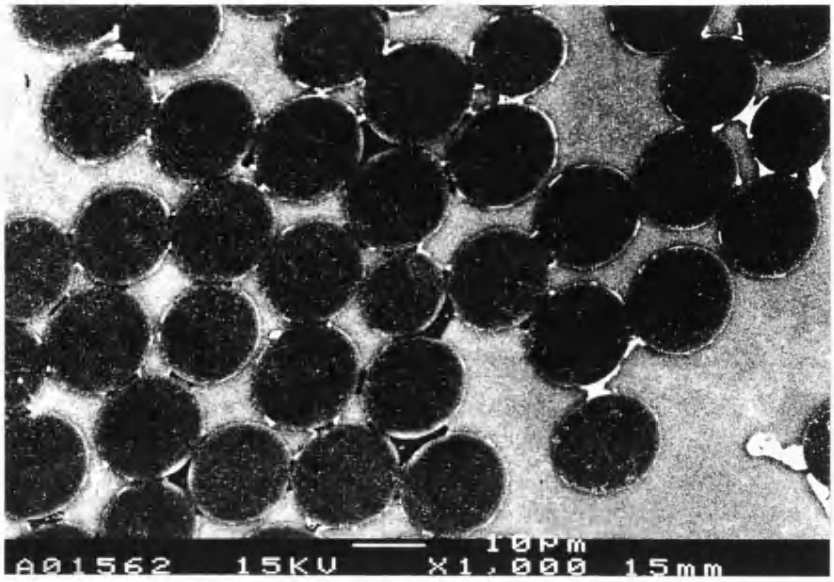

Figure 3.50 SEM micrograph of Altex reinforced A201.

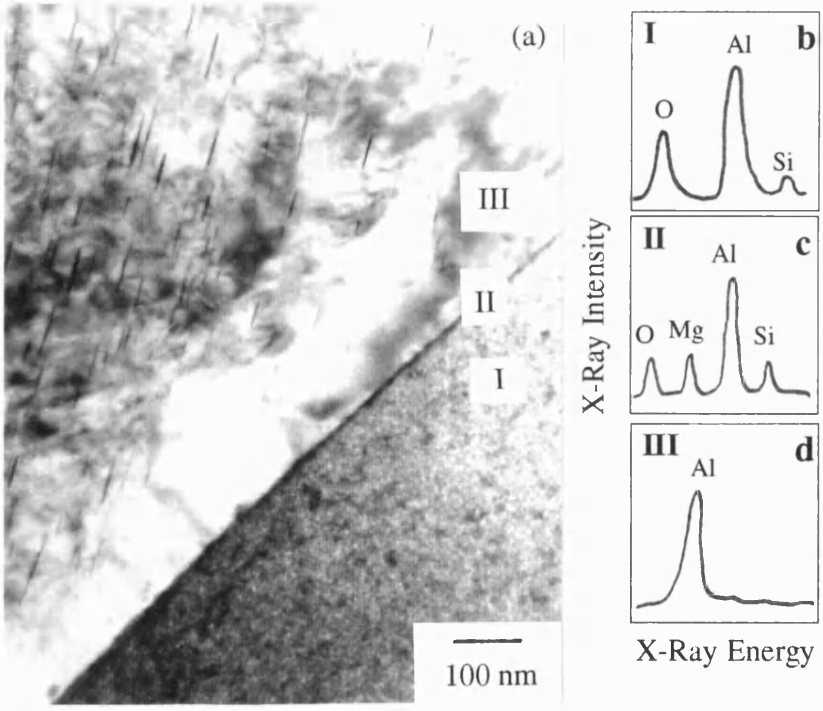

Figure 3.51 Thin foil of Altex reinforced A201:

(a) fibre/matrix interface region, TEM;

(b) EDS from fibre, region I;

(c) EDS from interface, region II;

(d) EDS from matrix, region III.

Like the unreinforced material some precipitation occurred during manufacture. The range of precipitate sizes is illustrated in Figures 3.51(a) and 3.52, with thickness varying from <5nm up to 300nm and the length between 100nm and 3μm. The orientation of the precipitates suggests that both θ and Ω are present.

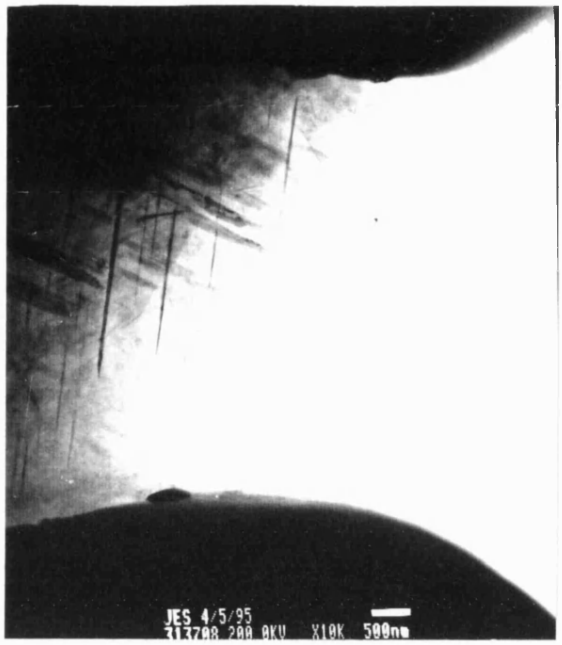

Figure 3.52 Thin foil of Altex reinforced A201.

(ii)Heat-Treated

Figure 3.55 shows that most of the second phase has been removed. No reaction was observed at the interface. EPMA data, Table 3.14, gives the composition of the composite before and after solutionising and shows that the copper taken up in the cast eutectic has been dissolved into the matrix, and the magnesium content of the matrix has been depleted.

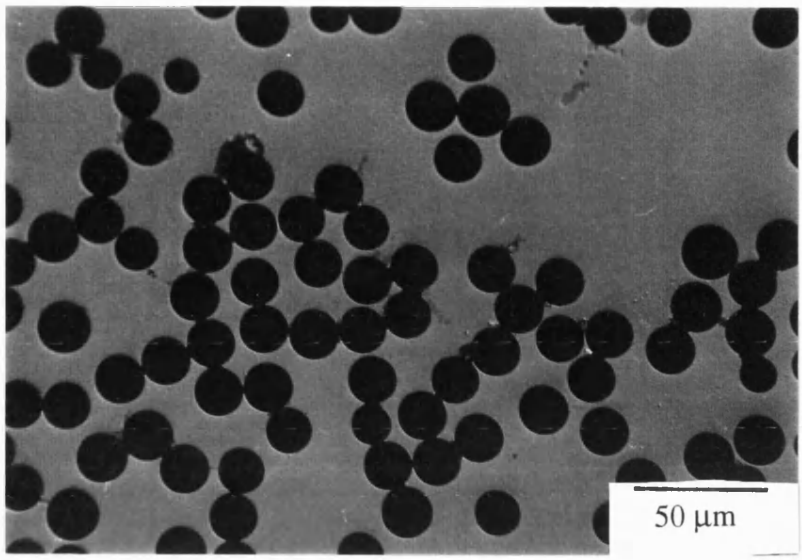

Figure 3.55 Solution treated Altex reinforced A201.

Table 3.14 ZAF corrected wt.% data for Altex/A201.

Element	cast	solution treated
Al	96.7 ± 1.4	95.1 ± 0.9
Cu	1.79 ± 1.52	4.27 ± 0.42
Mg	0.25 ± 0.02	0.08 ± 0.02
Ag	0.46 ± 0.13	0.50 ± 0.02
Total	99.1 ± 1.0	99.1 ± 1.4

Figure 3.56 shows the ageing curve for the Altex reinforced A201, with the unreinforced alloy included for comparison. The hardness increases from 130 HV to reach a peak of 155 ± 7 HV after 2 hours which remains until ~50 hours when the hardness begins to fall. It can be seen that the hardness of the composite falls off earlier and to a greater extent than the unreinforced alloy.

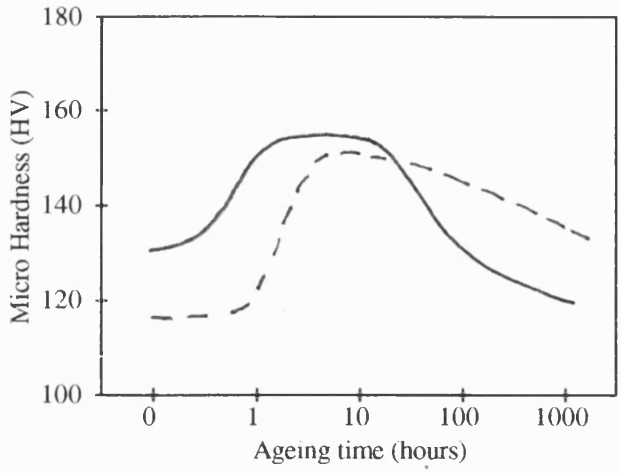

Figure 3.56 Microhardness versus ageing time at 170°C, Altex/A201.

TEM analysis of the peak-aged Altex composite, Figure 3.57 shows the presence of very fine precipitates lying normal to each other. The precipitates are ~ 3nm thick and between 20 and 50 nm long. There is no apparent reaction at the fibre/matrix interface. Diffraction patterns from the fibres, were identical to fibres from the cast composite. EDS from the fibre, interface and matrix, show no change from the cast composite.

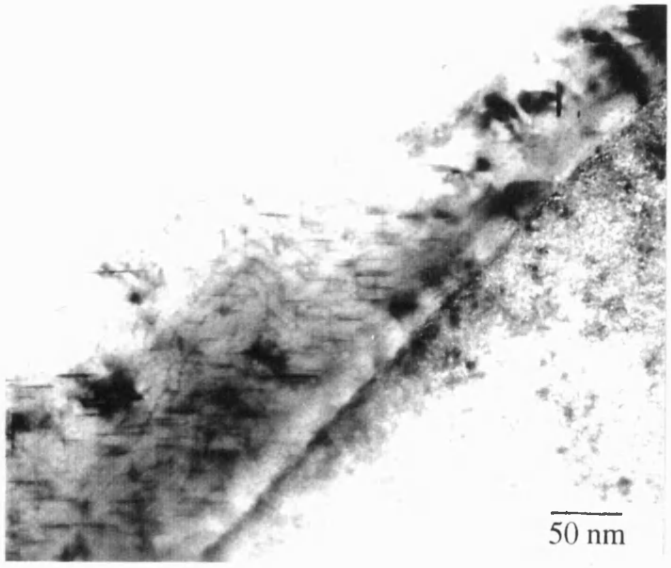

Figure 3.57 Thin foil of peak-aged Altex reinforced A201.

Diffraction analysis of the precipitates, Figure 3.58, indicates that they consist of θ'. EDS revealed aluminium and copper, no magnesium or silver was detected.

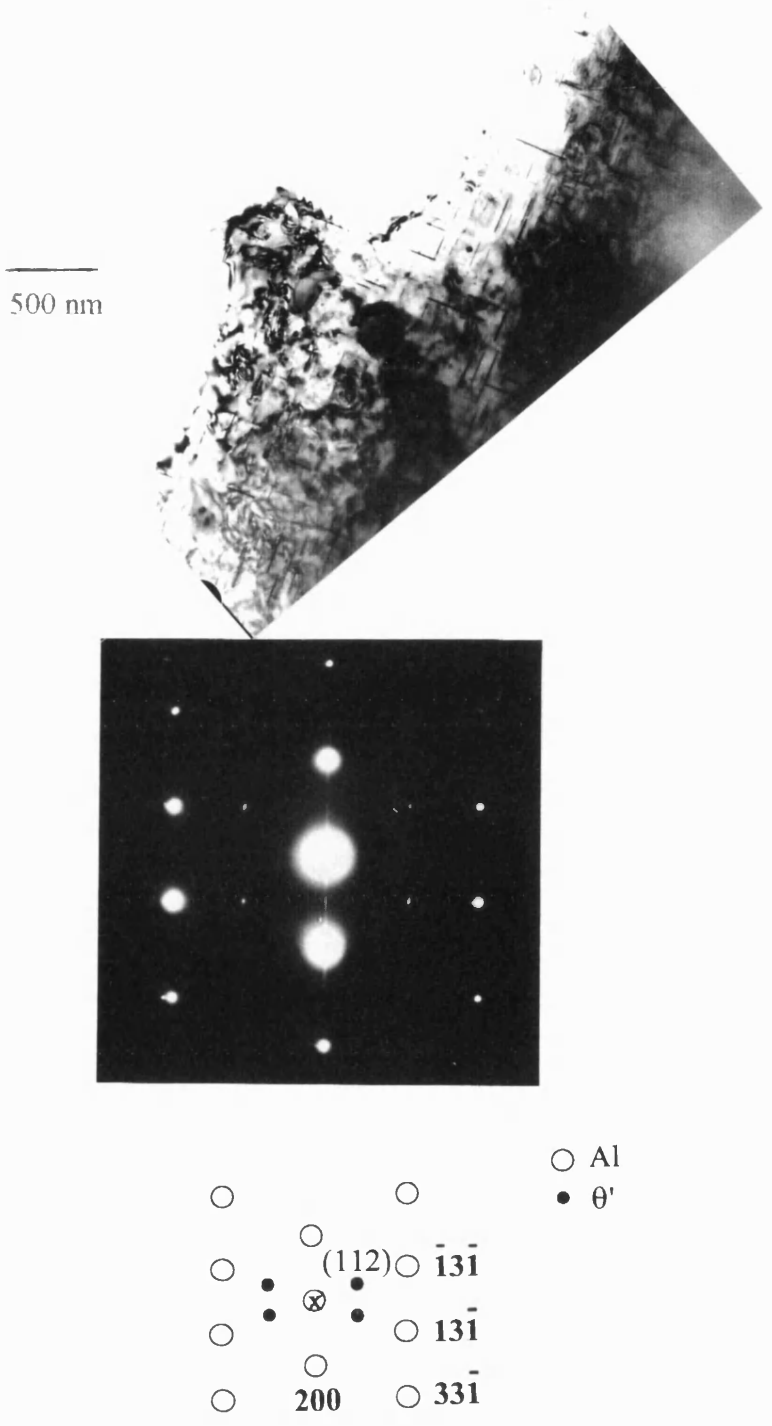

Figure 3.58 Precipitates from peak-aged Altex/A201, [013] beam direction.

Precipitates in the over-aged condition were still small, ~10nm thick and between 60 and 200 nm long, and diffraction analysis showed no differences to the peak-aged precipitates. The precipitate density was deduced to be ~ 1 x 10^{20} m^{-3}.

3.5.2(b) Mechanical Testing

Stress-strain curves for cast and peak-aged composite in longitudinal tension are given in Figure 3.59. Both curves are similar to the Altex/ARE415 composite, with a 'knee-point', occurring at a stress of 105 MPa for cast material and 190 MPa for composite in peak-aged condition; the corresponding strains were 0.10% and 0.15%. The tensile strength of the composite was found to increase from 270 MPa to 415 MPa after heat treatment, whilst the failure strains were not significantly different. The presence of the reinforcement significantly improves the Young's modulus compared to the unreinforced alloy, with average values of 120 GPa and 145 GPa for the cast and peak-aged conditions. When the sample variation is accounted for these values are not significantly different. Collated test data is given in Table 3.15.

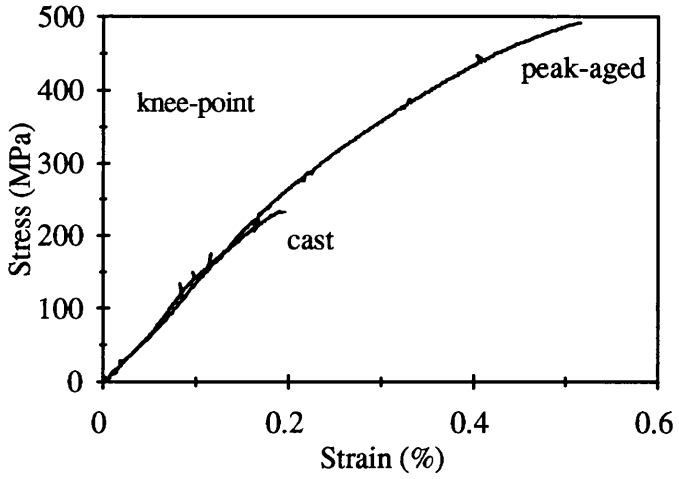

Figure 3.59 Tensile test on Altex/A201, longitudinal.

Table 3.15 Longitudinal tensile properties, Altex/A201

condition	Young's modulus (GPa)	yield stress (MPa)	strain at yield (%)	tensile strength (MPa)	strain to failure (%)
cast	120 ± 15	105 ± 30	0.10 ± 0.01	270 ± 30	0.30 ± 0.10
peak-aged	145 ± 20	190 ± 15	0.15 ± 0.05	420 ± 36	0.40 ± 0.10

Examination of the fracture surfaces shows evidence of fibre pull-out and matrix yielding, Figure 3.60(a) and (b), cast and peak-aged respectively. There is no significant difference in the length of pull-out between samples, and both samples showed evidence of matrix adhesion to the fibre surfaces. After testing several fractured samples were polished and then observed under the microscope. This analysis, Figure 3.61, shows that some of the fibres failed at several points away from the fracture surface, but not farther than 1μm.

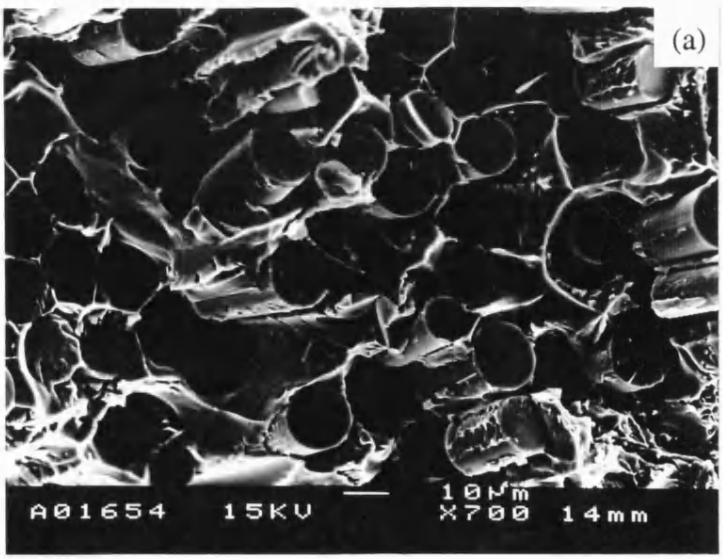

Figure 3.60 Longitudinal tensile failure of Altex/A201: (a) cast;

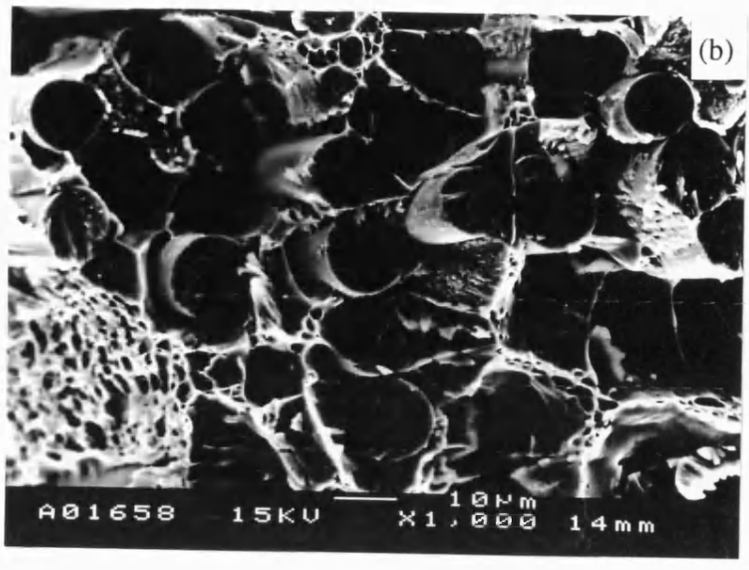

Figure 3.60 Longitudinal tensile failure of Altex/A201: (b) peak-aged.

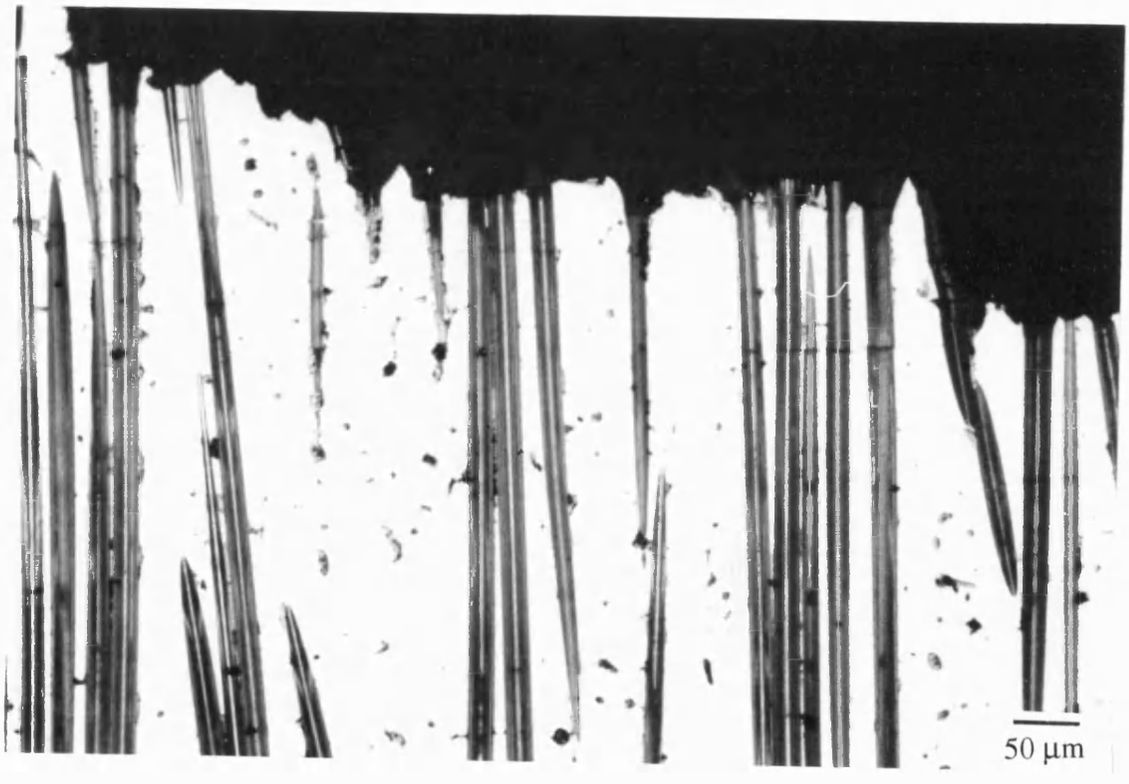

Figure 3.61 Polished longitudinal tensile failure of Altex/A201.

Stress-strain curves for the cast and peak-aged composite under transverse tension are given in Figure 3.62, the cast samples exhibited a yield-point, but the peak-aged samples appear linear up until failure. The yield stress for the cast samples is ~77 MPa but has a large scatter, the associated strain is 0.12 %. The tensile strength of the composite fell from 105 MPa to 85 MPa after heat treatment, but the two values are similar when the scatter is accounted for, the corresponding strain to failure is 0.14 % for both conditions. The values for Young's modulus are 70 GPa and 64 GPa for the cast and peak aged samples, with a large variation in results. The test data is collated in Table 3.16.

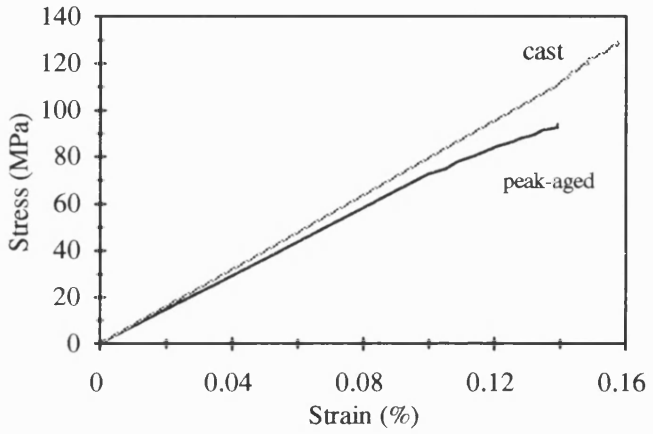

Figure 3.62 Tensile test on Altex/A201, transverse.

Table 3.16 Transverse tensile properties, Altex/A201.

condition	Young's modulus (GPa)	yield strength (MPa)	strain at yield (%)	tensile strength (MPa)	strain to failure (%)
cast	70 ± 26	77 ± 24	0.12 ± 0.05	105 ± 8	0.14 ± 0.06
peak-aged	64 ± 11			85 ± 26	0.14 ± 0.02

Examination of the fracture surfaces, Figure 3.63, shows no difference between samples, fibre splitting and matrix adhesion occur after both conditions, indicative of a strong interfacial bond. A polished fracture surface, Figure 3.64, shows areas of matrix cracking.

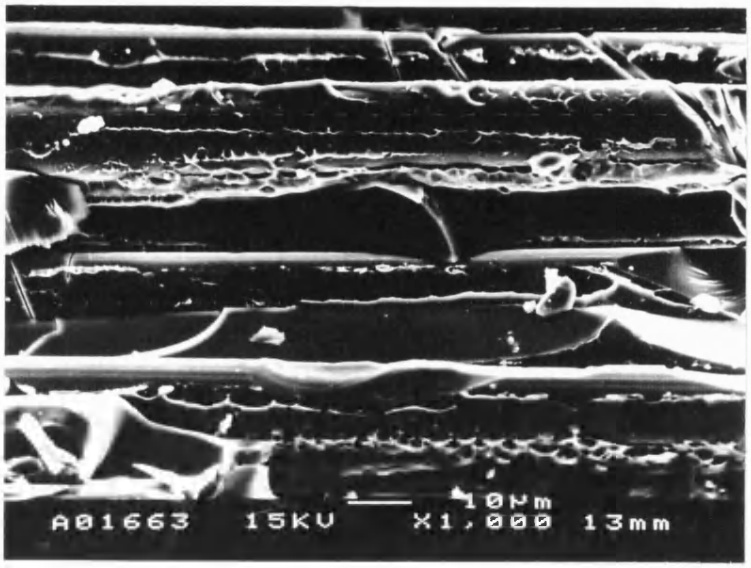

Figure 3.63 Transverse tensile failure of Altex/A201.

Figure 3.64 Polished transverse tensile failure of Altex/A201.

3.5.3 Reinforced with Nicalon

3.5.3(a) Microstructure

(i)Cast

A transverse section through the cast composite, Figure 3.65, shows good infiltration of the fibres by the liquid metal, with matrix porosity less than 1 vol.%. The fibre volume fraction was 0.42 ± 0.03, with an uneven spatial distribution. After etching, Figure 3.66, the grain size is revealed to show no difference to that in the unreinforced alloy. The matrix possessed a cored, dendritic structure containing the divorced aluminium-copper eutectic ($CuAl_2$ and aluminium).

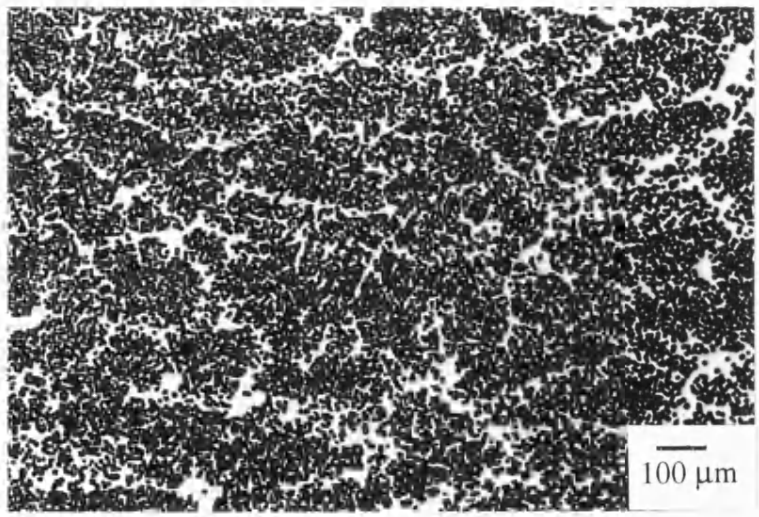

Figure 3.65 Light micrographs of Nicalon reinforced A201.

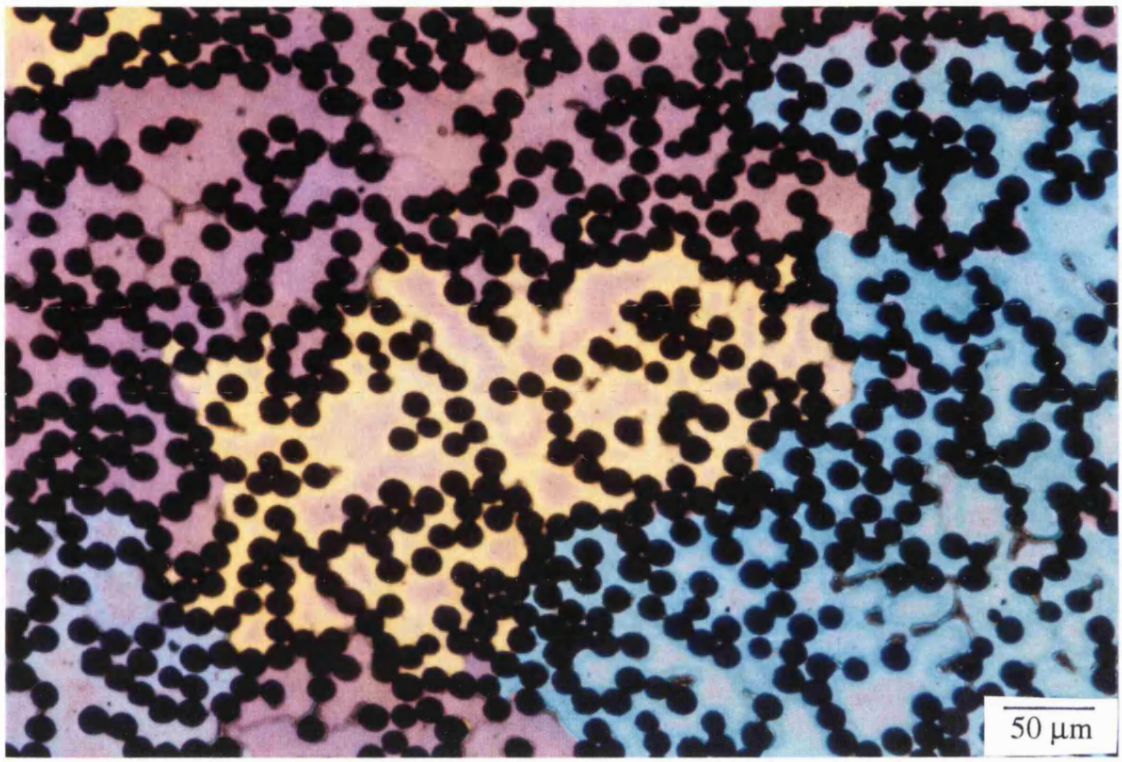

Figure 3.66 Micrograph from etched Nicalon reinforced A201.

A TEM micrograph of the fibre/matrix interface is shown in Figure 3.67(a). EDS data from the fibre, fibre/matrix interface and matrix, Figures 3.67(b-d), show that like the Nicalon/ARE415 composite, magnesium has segregated to the surface of the fibre. Diffraction analysis of the fibres was the same as that from fibres in the cast Nicalon/ARE415 composite.

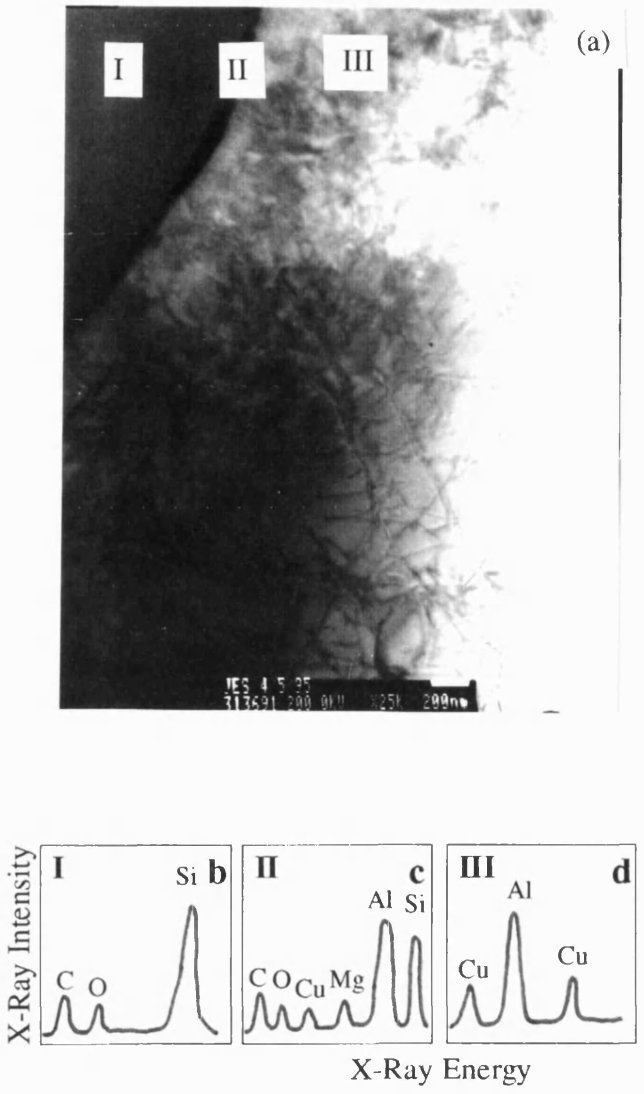

Figure 3.67 Thin foil of Nicalon reinforced A201:

(a) fibre/matrix interface region, TEM;

(b) EDS from fibre, region I;

(c) EDS from interface, region II;

(d) EDS from matrix, region III.

The interface, Figure 3.68, shows patchy precipitation and no diffraction patterns were obtained, however, evidence suggests the precipitates are θ type. Large phases observed at the fibre/matrix interface have been identified by EDS, Figure 3.68(b), to contain copper and aluminium, the morphology suggests that they are eutectic $CuAl_2$. Figures 3.67 and 3.69, show dislocations in the vicinity of the fibre, the density of which is greatest near the fibres and decreases away from the fibres. The dislocation density at the interface was estimated as 9×10^{13} m^{-2}.

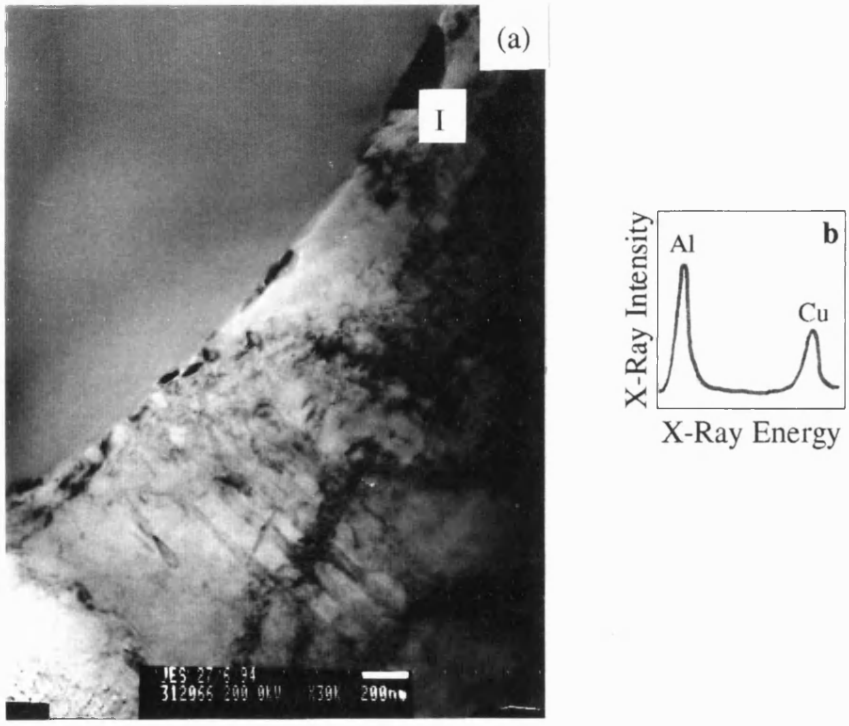

Figure 3.68 Thin foil cast Nicalon reinforced A201:

(a) fibre/matrix interface region, TEM;

(b) EDS from interfacial phase, region I.

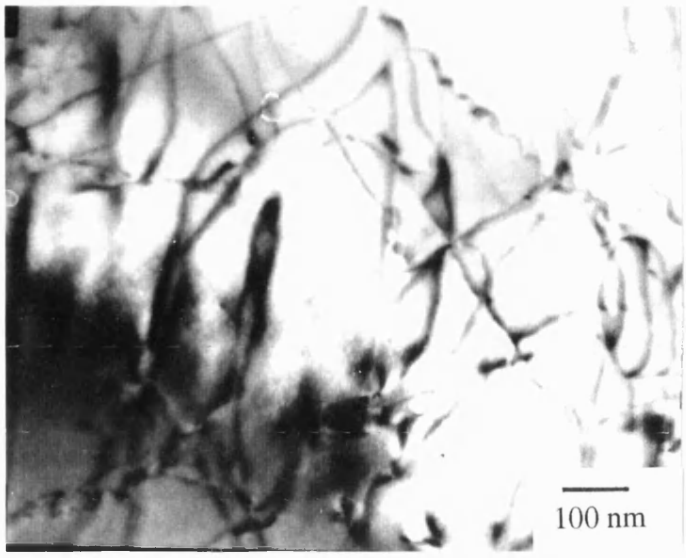

Figure 3.69 Thin foil of cast Nicalon reinforced A201, showing the presence of dislocations.

(ii)Heat-Treated

EPMA analysis of the matrix, Table 3.17, shows that solutionising has not homogenised the matrix, the main points to note are the loss of magnesium from the matrix and the presence of silicon. The Nicalon reacts with the matrix during solution treatment, Figure 3.70 shows second phase around the fibres and evidence of needles extending into the matrix. EDS revealed the phases around the fibres contained aluminium, copper and silicon.

Table 3.17 ZAF corrected wt.% data for the Nicalon/A201 composite.

Element	cast	solution treated
Al	96.1 ± 1.8	94.7 ± 0.7
Cu	1.65 ± 0.32	3.22 ± 0.18
Mg	0.11 ± 0.02	-
Ag	0.41 ± 0.07	0.47 ± 0.08
Si	-	1.21 ± 0.33
Total	98.4 ± 1.9	98.7 ± 0.8

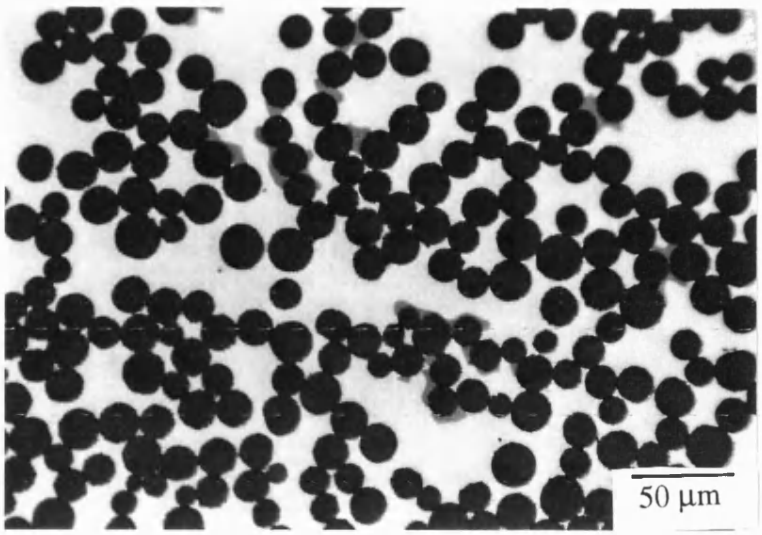

Figure 3.70 Solution treated Nicalon reinforced A201.

Upon ageing the Nicalon/A201 composite hardness increases from 110 HV to reach a peak of 130 ± 5 HV after 2 hours, it then remains at this level up to 100 hours when the hardness falls slightly, Figure 3.71. The ageing response of the Nicalon composite is slight and clearly inferior to the unreinforced alloy.

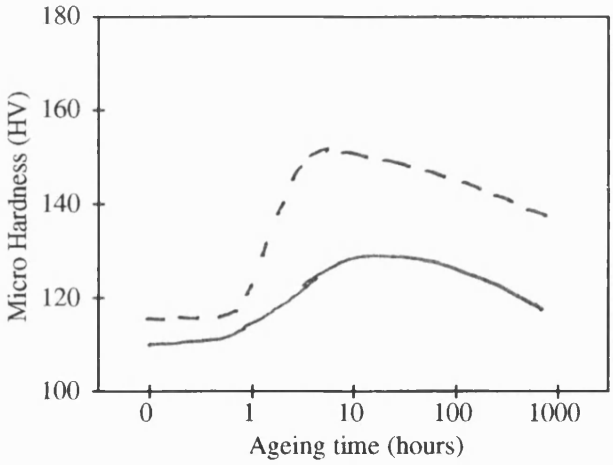

Figure 3.71 Microhardness versus ageing time at 170°C, Nicalon/A201.

TEM analysis of the peak-aged Nicalon composite confirmed the reaction observed optically. Figures 3.72(a) and (b) show the fibre/matrix interface, the central region of the fibre appears unchanged from the cast condition, but the outer 150nm shows a clear change in structure, with the fine microcrystallites being replaced. Needles are also found to extend out into the matrix. Diffraction analysis from the central region of the fibre was identical to fibres from the cast composite, and indicated the presence of β-silicon carbide. The diffraction pattern from the reacted section of the fibre, Figure 6.72(c), shows a diffuse central region with spotty outer rings. The ring patterns do not correspond to β-silicon carbide and many of the spots correspond to magnesium, magnesium oxide and several magnesium, aluminium, silicon and oxygen containing phases. The reacted zone is most likely to be a combination of phases, the corresponding EDS trace is given in Figure 3.72(d).

A needle phase with corresponding diffraction pattern and EDS trace, Figures 3.73, shows the presence of aluminium and carbon, with diffraction analysis indicating the phase to be rhombohedral aluminium carbide, Al_4C_3.

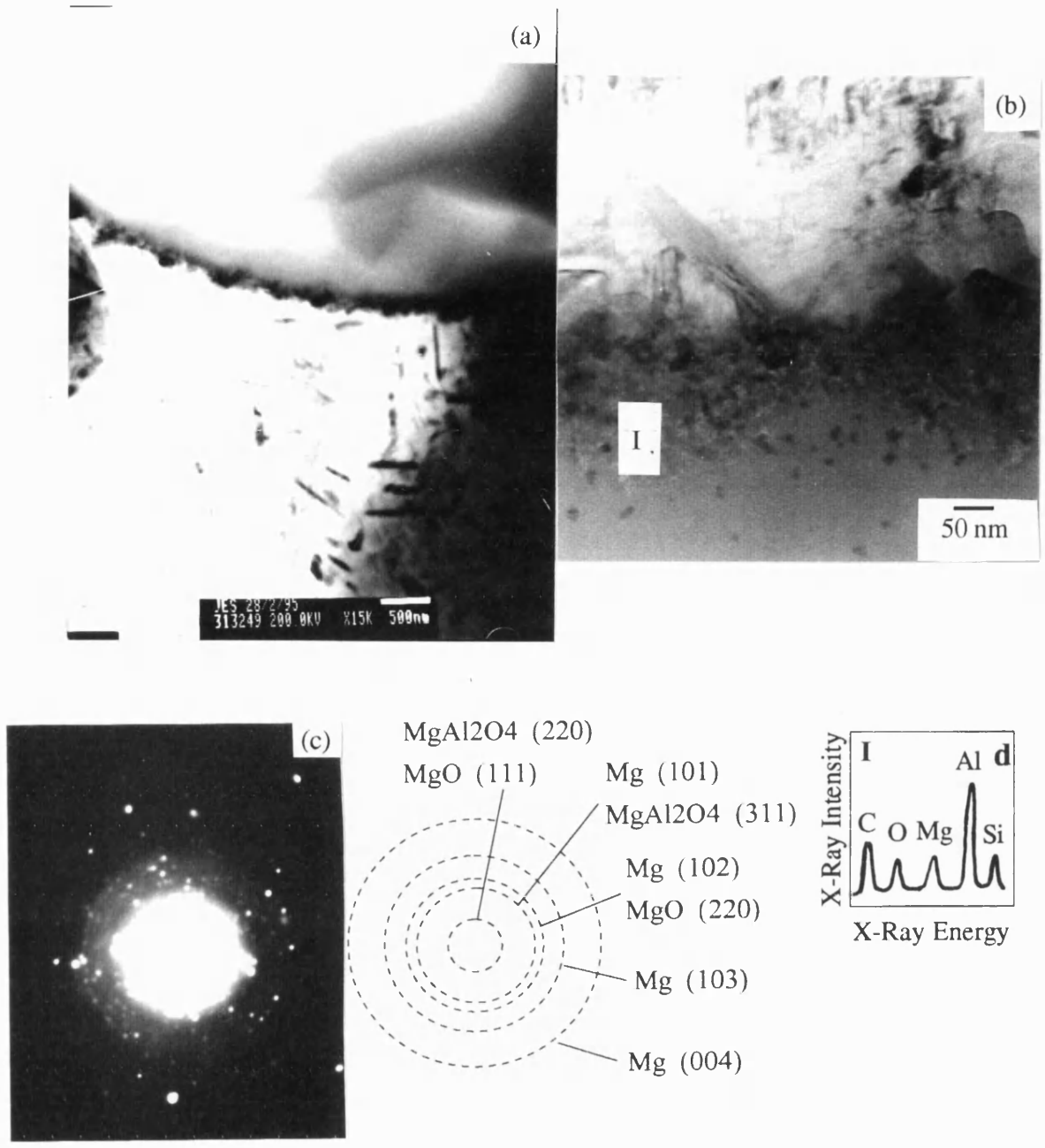

Figure 3.72 Thin foil of peak-aged Nicalon/A201:

(a) interface region, (b) interface region;

(c) diffraction pattern, region I, fibre;

(d) EDS, from fibre, region I.

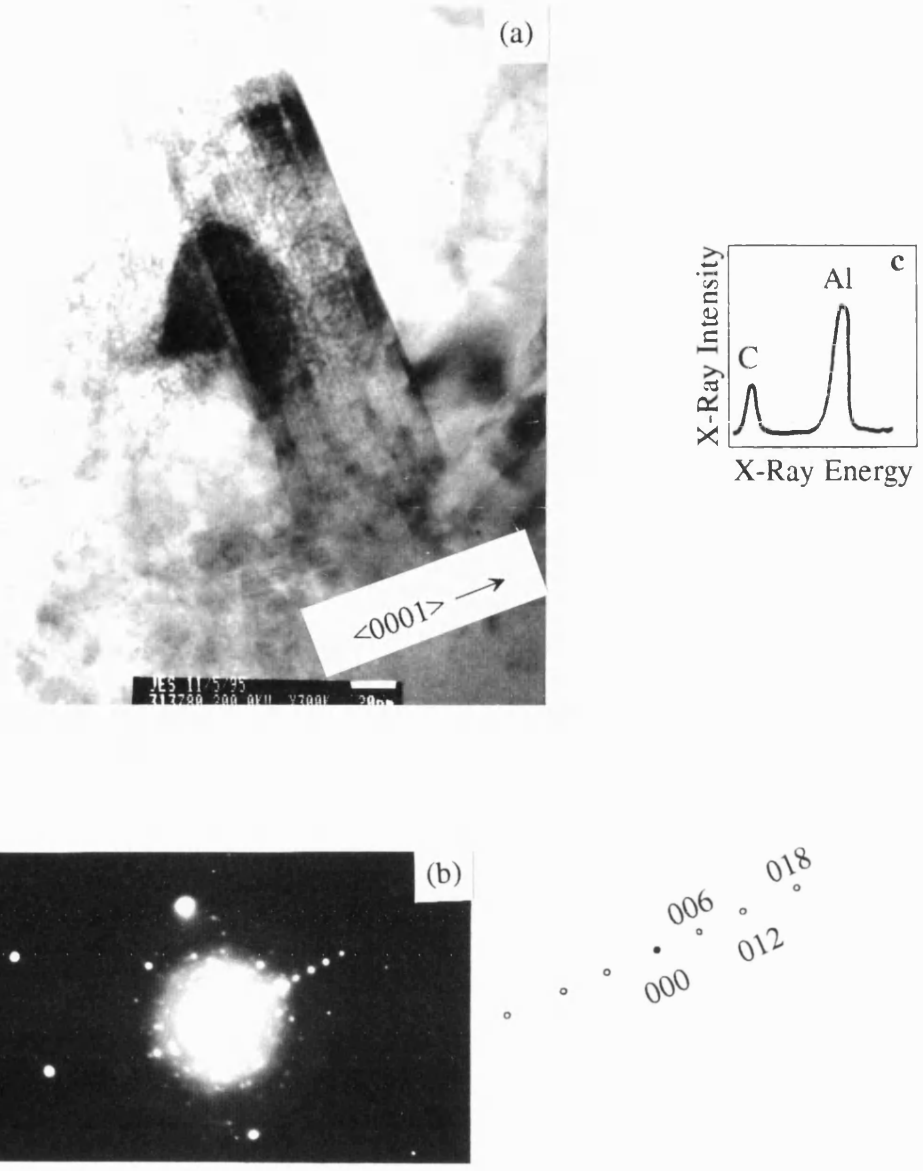

Figure 3.73 (a) Reaction needle growing from Nicalon fibre into A201 matrix:
(b) diffraction pattern from needle;
(c) EDS trace from needle.

Figure 3.74 shows a general view of the precipitation in the peak-aged Nicalon composite. The majority of precipitates are perpendicular and ~10 nm thick and 100 nm long, and contain aluminium and copper, there are also a number of coarse particles present. The estimated precipitate density was 3 x 10^{20} m^{-3}. Diffraction analysis of the precipitates was identical to the θ' type observed in the Altex reinforced composites.

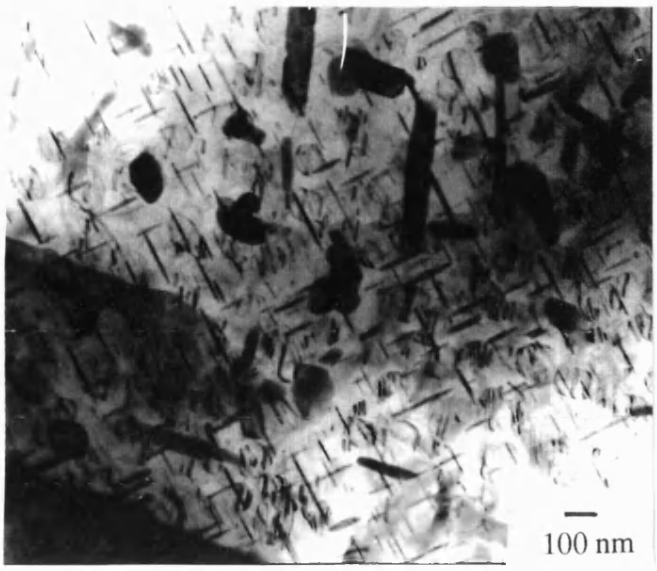

Figure 3.74 Thin foil through peak-aged Nicalon/A201.

In the over-aged condition the fibre reaction zone remains unchanged compared to the peak-aged condition. The precipitates have increased in length to excess of 200nm, Figure 3.75, but diffraction analysis and EDS shows no change from the peak-aged condition.

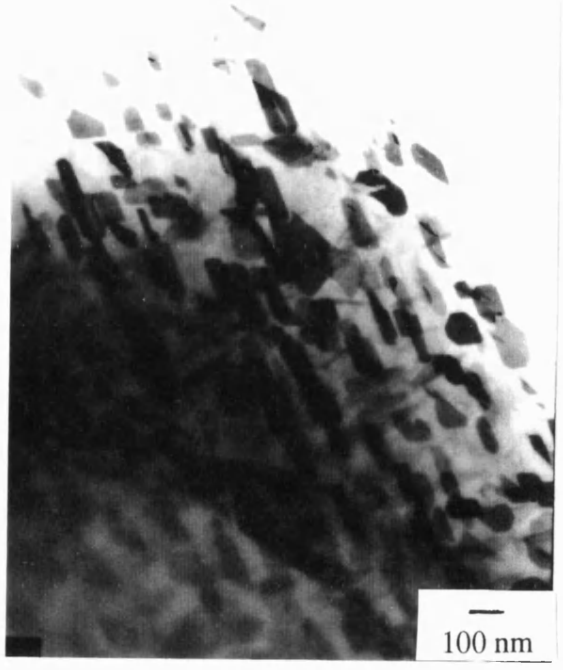

Figure 3.75 Thin foil through over-aged Nicalon/A201.

3.5.2(b) Mechanical Testing

Stress-strain curves for the cast and peak-aged composite in longitudinal tension are given in Figure 3.76, both curves exhibit a knee, occurring at 100 MPa for the cast material and 145 MPa for the peak-aged condition; corresponding to strains of 0.09 % and 0.13 %. The tensile strength increased slightly from 227 MPa to 266 MPa after heat treatment. The Young's modulus are 107 GPa and 128 GPa for the cast and peak-aged conditions. Collated test data is given in Table 3.18.

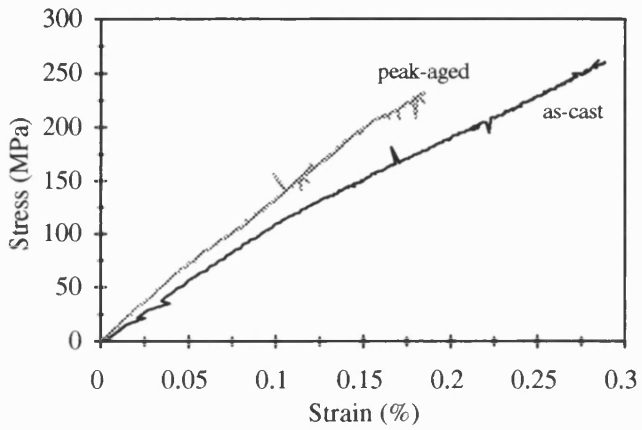

Figure 3.76 Tensile test on Nicalon/A201, longitudinal.

Table 3.18 Longitudinal tensile properties, Nicalon/A201.

condition	Young's modulus (GPa)	yield strength (MPa)	strain at yield (%)	tensile strength (MPa)	strain to failure (%)
cast	107 ± 12	100 ± 13	0.09 ± 0.02	227 ± 36	0.29 ± 0.04
peak-aged	128 ± 16	145 ± 30	0.13 ± 0.03	266 ± 31	0.25 ± 0.05

Examination of the cast fracture surface shows evidence of fibre pull-out, matrix yielding and adherence of the matrix to the fibre surface, Figures 3.77(a) and (b). There is also evidence of fibre splitting. In the peak-aged condition the fracture surface

is almost flat, Figure 3.78(a), with fibre splitting clearly evident. The reaction zone around the fibres is clear, Figure 3.78(b), and is still attached to the fibre after failure indicating that it is well bonded.

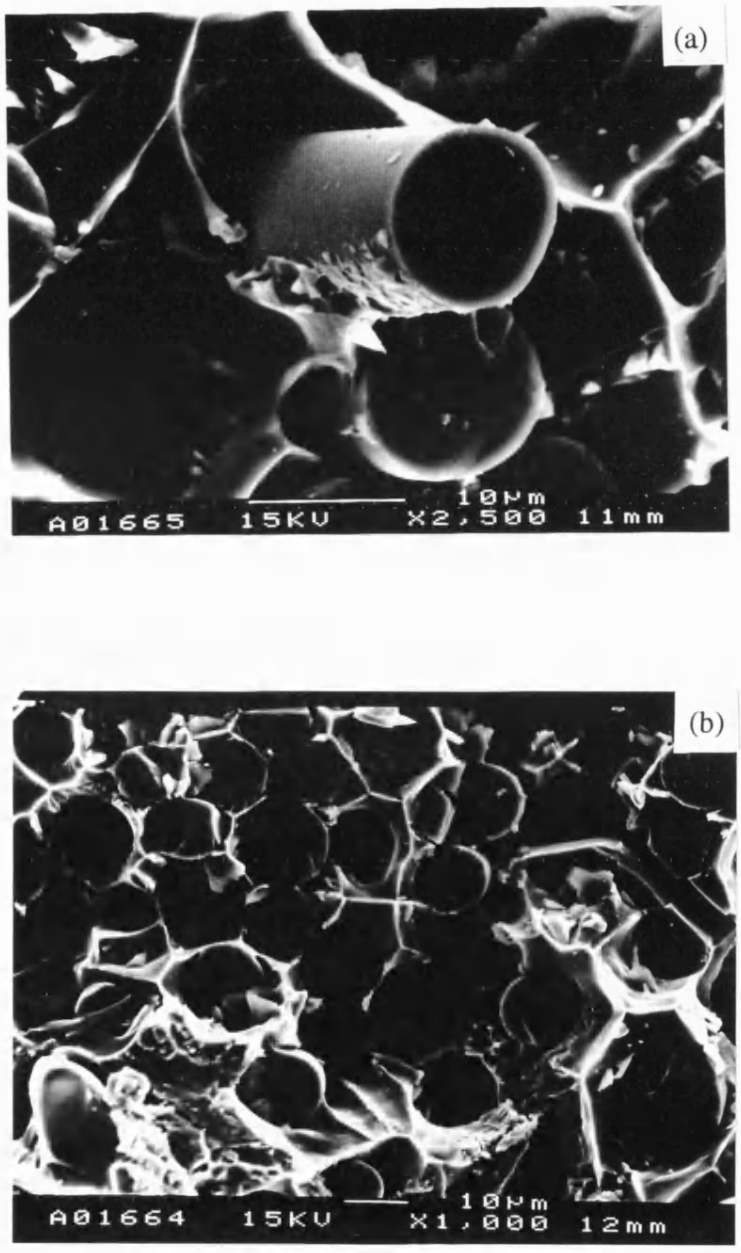

Figure 3.77 Longitudinal tensile failure, cast Nicalon/A201.

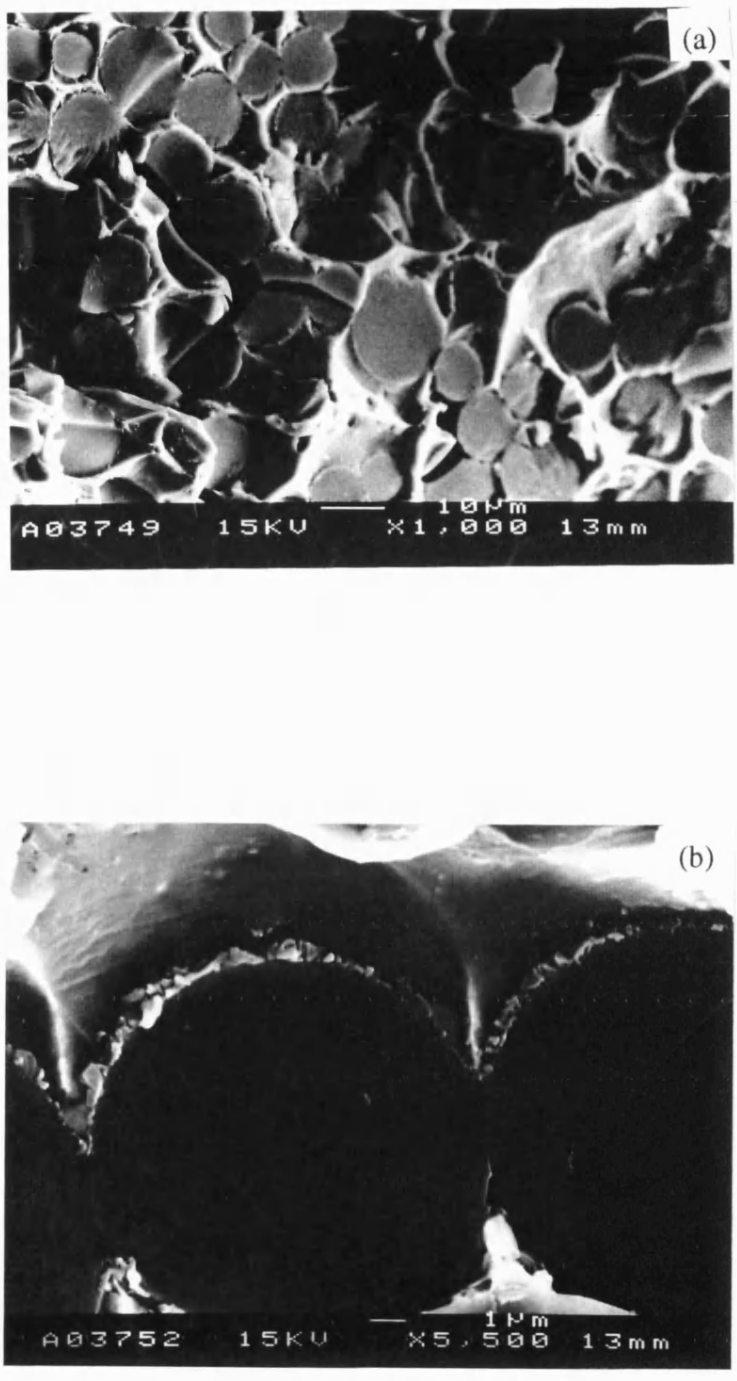

Figure 3.78 Longitudinal tensile failure, peak-aged Nicalon/A201.

Stress-strain curves for the Nicalon/A201 composite under transverse tension in the cast, peak-aged and over-aged conditions are plotted in Figure 3.79. Both the cast and over-aged samples exhibit a yield point, but the peak-aged sample remains linear until failure. The yield stress for the cast and over-aged are 67 MPa and 100 MPa respectively, with corresponding strains of 0.07 % and 0.1 %. The tensile strengths recorded were 125 MPa, 104 MPa and 108 MPa for the cast, peak-aged and over-aged respectively. The corresponding failure strains were 0.15 %, 0.13 % and 0.10 %. The Young's modulus is consistent between all the conditions, 90 GPa, 93 GPa and 99 GPa for the cast, peak-aged and over-aged, and is higher than the unreinforced alloy data. The data is collated in Table 3.19.

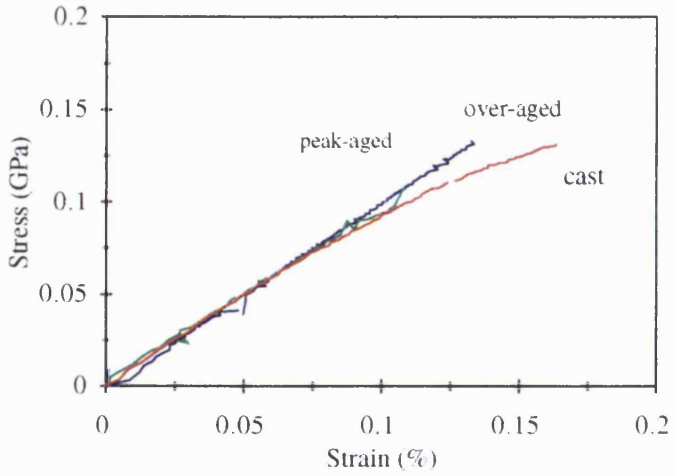

Figure 3.79 Tensile test on Nicalon/A201 composite, transverse.

Table 3.19 Transverse tensile properties, Nicalon/A201.

condition	Young's modulus (GPa)	yield strength (MPa)	strain at yield (%)	tensile strength (MPa)	strain to failure (%)
cast	90 ± 4	67 ± 11	0.07 ± 0.01	125 ± 13	0.15 ± 0.04
peak-aged	93 ± 10			104 ± 12	0.13 ± 0.02
over-aged	99 ± 10	100 ± 10	0.1± 0.002	108 ± 18	0.10 ± 0.02

Examination of the fracture surfaces, Figure 3.80(a-c), shows fibre splitting in all conditions. In the cast condition, Figure 3.80(a), matrix metal can clearly be seen adhered to the fibres. In the peak-aged and over-aged samples, Figure 3.80(b) and (c) respectively, the interfacial reaction is apparent at the fibre surfaces and is still bonded to the fibres.

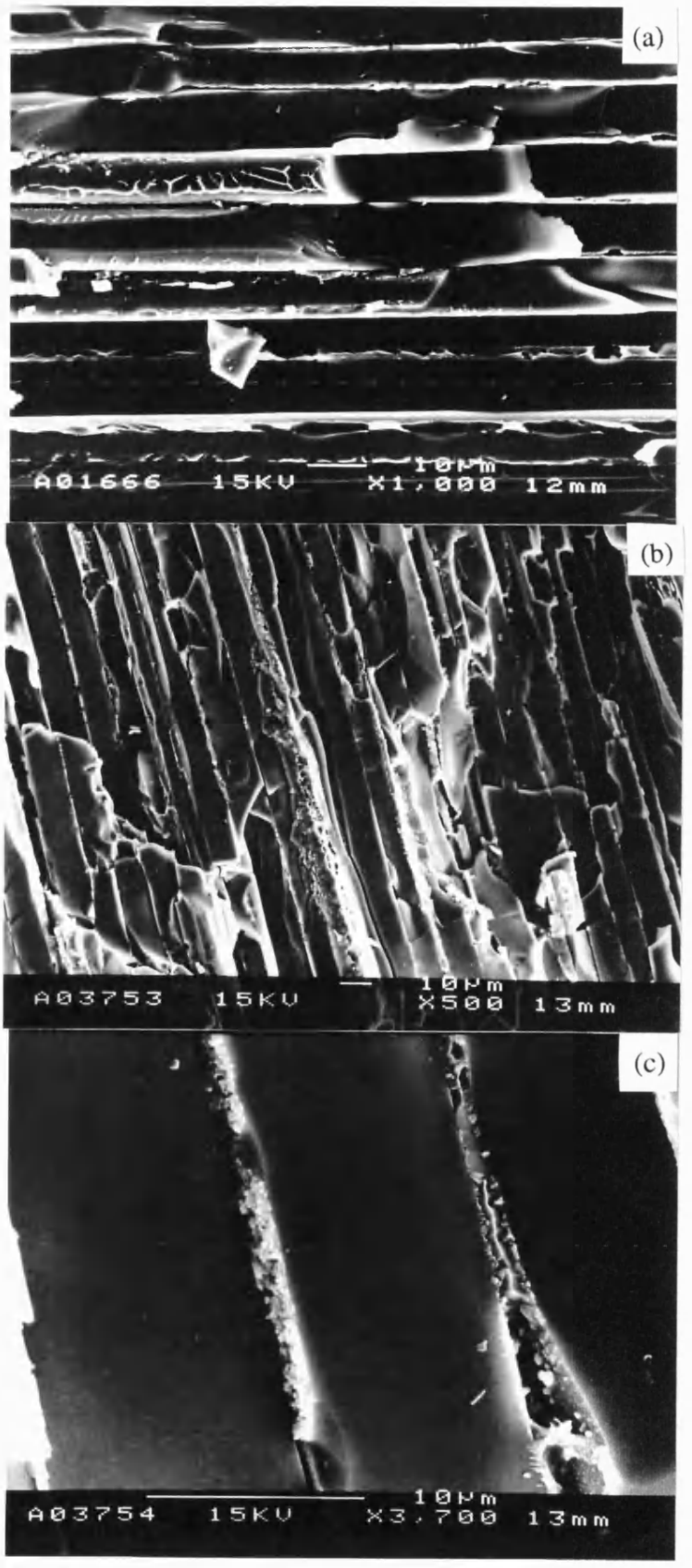

Figure 3.80 Transverse tensile failure of Nicalon/A201: (a) cast;

(b) and (c) peak-aged;

4.0 DISCUSSION

4.1 Microstructural Aspects

4.1.1 As-Received Fibres & Monofilament

4.1.1(a) Altex

The X-ray diffraction (XRD) traces for the Altex fibre, Figure 3.2, are not indicative of a single Al_2O_3 phase, but contain at least two separate Al_2O_3 phases. The phases most likely to be present are δ, γ or η. The evidence for δ-Al_2O_3 is as follows: The peak at 1.787Å is listed only for δ-Al_2O_3 and the peak at 2.739Å corresponds more closely to δ-Al_2O_3 (2.73Å) than either γ-Al_2O_3 (2.80Å) or η-Al_2O_3 (2.80Å). The reasons for believing phases other than δ-Al_2O_3 to be present are: The peak at 2.399Å does not correspond well with δ-Al_2O_3 (2.43Å), but does with γ-Al_2O_3 (2.39Å) and η-Al_2O_3 (2.40Å). δ-Al_2O_3 has many peaks which do not appear on the trace, e.g. 4.07Å, 2.87Å, 2.58Å, 1.95Å, 1.91Å, 1.49Å, 1.45Å. Altex fibre most probably contains some δ-Al_2O_3 with the majority being either γ-Al_2O_3, or η-Al_2O_3. The crystal structure for the δ form of alumina is tetragonal, while the γ and η forms are both cubic with different lattice parameters. No change in XRD trace was observed after thermal exposure in air at 1000°C, this shows that the fibre is thermally stable under these conditions.

Transmission electron microscopy (TEM), revealed the fibre to have a fine crystalline structure, with crystals ~10 nm in diameter. Selected area diffraction (SAD), of the fibre gave a diffuse central region and a series of concentric rings. The diffuse region indicates the presence of an amorphous phase, whilst the rings can be indexed to show a cubic structure, a = 0.79 nm, consistent with γ-Al_2O_3. Electron-probe microanalysis (EPMA) of the Altex fibre gave the composition to be 44.9 wt.% aluminium, 7.5 wt.% silicon and 47.6 wt.% oxygen. Assuming all the aluminium goes to form alumina, Al_2O_3, and all the silicon forms silica, SiO_2, it may be concluded that the fibre composition is 85.3 ± 0.9 wt.% Al_2O_3 and 15.3 ± 0.4 wt.% SiO_2. These results

concur with the manufacturer's data which quote an 85 wt.% γ-alumina fibre, the remainder silica.

The fibre exhibited a range of diameters from 6 to 23μm, averaging 16μm. The variation in fibre diameter is associated with the manufacturing route of melt spinning.

4.1.1(b) Nicalon

TEM and SAD of the fibre revealed very fine nm size crystals of β-SiC, a = 0.436 nm, and an amorphous phase. EPMA of the Nicalon fibre in this study, gave the composition to be 54.9 wt.% silicon, 31.6 wt.% carbon and 11.7 wt.% oxygen. Following Bleay [33] we shall assume the elements to be present as silicon carbide, silicon oxycarbide and free carbon, and that the oxycarbide phase consists of equal amounts of Si-C and Si-O bonding in accord with, $SiOC_{0.5}$. It may then be deduced that the fibre composition is 49.2 ± 0.3 wt.% silicon carbide, 36.5 ± 0.9 wt.% silicon oxycarbide, and 14.2 ± 0.6 wt.% C. This is in agreement with the work of Bleay, and Hicks [33, 112], where the composition can be calculated as 49.8 wt.% silicon carbide, 37.0 wt.% silicon oxycarbide, and 13.3 wt.% C.

Like the Altex fibre there was a range of diameters from 7 to 21μm, averaging 12 μm. The variation in fibre diameter is again associated with the manufacturing route.

4.1.1(c) *Sigma*

The Sigma monofilament consisted of silicon carbide on a tungsten core and unlike the other fibres had a binder present in the form of a tape. EDS confirmed the binder to contain silicon oxygen and carbon. The tungsten core was 10 μm in diameter with an overall monofilament diameter of 100 μm.

4.1.2 Fibre Reinforced Cast Composites

This section considers composites reinforced with Altex and Nicalon fibres, which share many similar characteristics.

4.1.2(a) Processing Parameters

In liquid metal infiltration (LMI) the most significant factors to consider are, the initial applied pressure, the temperature of the alloy on casting and the temperature of the preform prior to infiltration. It is also important to keep the time at temperature to a minimum. The processing parameters used in this study were optimised on the ARE415 alloy reinforced with either Nicalon or Altex, but apply equally to all systems.

(i)The Applied Pressure

The experiments showed that infiltration was incomplete at an initial pressure of 3 MPa, but was satisfactory at 7 MPa. The initial pressure was followed by consolidation at 25 MPa. A schematic of the changes in pressure with time is shown in Figure 4.1, and shows that solidification takes ~ 5 seconds. The pressure required for infiltration is slightly higher than that reported for Saffil reinforced aluminium alloys [71], where infiltration was successful using an initial pressure of 2.5 MPa rising to 35 MPa after ~ 4 seconds when solidification was complete.

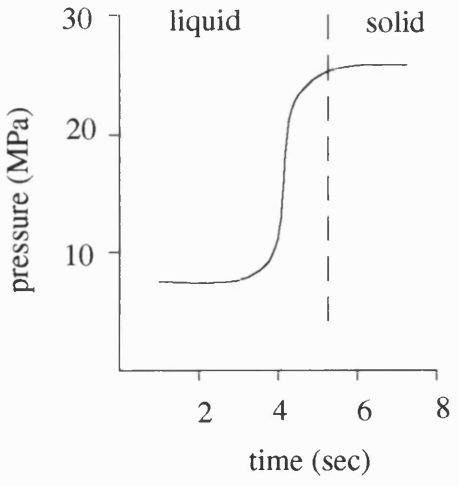

Figure 4.1 Schematic of pressure versus time during composite manufacture.

The theoretical pressure for infiltration may be calculated using the Blake-Kozeny equation [113] and the Kelvin equation. These model the pressure needed to overcome the resistance to viscous flow through the interstitial channels and the effect of enforced meniscus curvature at the melt front respectively.

(i) Blake-Kozeny

$$\frac{dP}{dZ} = 16.8v\mu\left[\frac{V_f}{2r(1-V_f)}\right]^2 \qquad \text{Eqn. 4.1}$$

where dP/dZ is the pressure gradient, v the fluid flow velocity ($\approx 0.03 ms^{-1}$), μ the dynamic viscosity ($\sim 10^{-3}$ Pas^{-1}), V_f the volume fraction and r the fibre radius. This equation assumes laminar flow for a fluid travelling transversely through a unidirectional bundle.

(ii) Kelvin

$$\Delta P = 2\gamma\Sigma\left(1/r_i\right) \qquad \text{Eqn. 4.2}$$

where ΔP is the pressure drop across surface with radius r_i, γ the surface energy (~ 0.84 Jm^{-2}). This equation assumes non-wetting of the reinforcements (contact angle >90°, which is the case for many ceramics in contact with aluminium), and as such r_i is half the interfibre spacing ($\sim 3x10^{-6}$ for Nicalon and Altex fibres in a square array).

Assuming the metal remains fluid, the theoretical pressure required for infiltration is calculated to be between 3 and 10 MPa, depending on fibre volume fraction and the geometry of packing. These values are in agreement with the experimental findings of this study.

Previous reports indicate that pressures as high as 100 MPa have been used for squeeze casting in order to effect infiltration before extensive solidification occurs [114]. However, such excessive pressures may damage the fibres if solidification has started, although no damage should be incurred if the fibres are enveloped fully with liquid metal. In commercial practice, pressures as high as 50-200 MPa are used for the production of alloy billets, in order to produce a fine grain structure by rapid freezing: following the Clapeyron equation,

$$\frac{dP}{dT} = \frac{\Delta H}{T\Delta \overline{V}} \qquad \text{Eqn. 4.3}$$

where ΔH is the change in enthalpy (~105 l.atm.mol^{-1}) and $\Delta \overline{V}$, is the change in molar volume (~1.3x10^{-3} l.mol^{-1}), the change in pressure causes the freezing point to be raised by 1°C per 10 MPa (200 MPa gives rise to a change of ~20°C). However in a composite the fibres act to constrain grain growth [115], and so the high pressures are not necessary.

(ii)The Alloy Melt Temperature

It was found that the using a temperature of 850°C complete infiltration was achieved. At 750°C, however, the central region of the composite remained uninfiltrated due, it is believed, to be a problem with premature freezing rather than wetting. Previous studies [71] utilising melt temperatures 150 - 200°C above the liquidus prior to casting, are comparable to the temperatures used in this study and report good infiltration. High temperatures are known to provide a reduction in the contact angle between the molten alloy and fibre [116] thus improving wetting.

Although high temperatures offer the best infiltration, the lowest temperature possible during processing should be used for the following reasons:

(i) chemical reaction should be minimised between the fibre and matrix.

(ii) problems associated with oxidation of magnesium or aluminium on melting/pouring, which can lead to changes in alloy composition, should be avoided.
(iii) the possibility of high levels of dissolved hydrogen from the atmosphere should be avoided.

The effects of (i) and (iii) are discussed in a later section. The problem of compositional changes during manufacture were studied by chemical analysis of the alloy prior and subsequent to infiltration. There was no difference in composition between the as-received and cast alloy, confirming that the high alloy melt temperature did not adversely affect the chemistry of the alloy.

(iii)Preform Preheat Temperature

When the preform preheat temperature was 400°C, there was a variation in fibre volume fraction from the billet top to bottom, as illustrated in Figure 3.10a. This presumably associated with premature freezing, such that when a pressure is applied, the areas that have partially solidified impinge on the fibres. Raising the temperature of the preform to 700°C prior to infiltration was found to avoid the problem, by eliminating freeze off in the vicinity of the fibres. Other workers report preforms preheated to temperatures of 700°C for die casting [117] and temperatures up to 500°C in squeeze casting [61], but make no mention of its effect on fibre distribution.

For the systems investigated the optimum processing conditions were found to be; a melt temperature of 850°C, an initial applied pressure of 7 MPa followed by consolidation at 25 MPa and a preform preheat temperature of 700°C.

Under the above conditions composites made from ARE415 and A201 alloys reinforced with Nicalon and Altex fibres shared many similar characteristics. The fibres were well infiltrated with metal and matrix porosity was less than 1vol%. Porosity was mainly found in places where fibres touch (see Figure 3.26b) and, in these cases,

infinite infiltration pressure would be required for complete infiltration [118]. The problem of voids can be overcome by improving the filament winding procedure so that the spacing between fibres can be controlled, or by promoting fibre wetting in these areas. Other workers have used discrete particles between the fibres [63], but this leads to a reduction in the matrix ductility. The distribution of fibres throughout the composite was fairly even, but could be improved, by reducing the number of touching fibres.

4.1.2(b) Effect of fibres on grain growth

The presence of fibres has been reported to constrain grain growth during solidification compared with that of the unreinforced alloy, the degree of restriction being dependent on fibre distribution (or spacing) [86, 116, 119]. This is the case for ARE415 reinforced with Nicalon and Altex, where the fibres are closely spaced the grain size is reduced from 200μm to 50μm, but neither reinforcement reduces the grain size of the A201 alloy, 300μm. Gungor [74] reports that if the dendrite arm spacing, DAS, controls the grain size and if it is less than the fibre spacing then the microstructure is not significantly affected by the fibres (often associated with short solidification times). For longer solidification times the fibres can act to constrain dendritic growth and modify the microstructure. For the unreinforced alloys the DAS was ~20μm for the ARE415 and ~10μm for the A201. In the case of the ARE415 composites there was constraint by the fibres, but for the A201 alloy the dendrite arm spacing was less than the fibre spacing and so there was no constraint. This is obviously a characteristic difference between the two alloys.

4.1.2(c) Solute Segregation

All of the Nicalon and Altex based composites revealed variations of solute concentration across a dendrite. This is evidenced by the back-scattered electron images of the matrix and EPMA data, as summarised in Table 4.1 for the copper distribution in ARE415 composites. This microsegregation is termed coring, and is

commonly observed in cast alloys. It is caused by freezing of the original dendrite arms as relatively pure metal, the liquid surrounding these dendrite arms becoming enriched in solute. When solidification occurs, the spaces between the dendrite arms become areas of high solute concentration, or eutectics. The fact that the solute elements are more soluble in the liquid state than the solid state accounts for segregation in the casting. Coring becomes more pronounced as the cooling rate increases.

Table 4.1 Distribution of copper (wt.%) for ARE415 composites.

	Altex	Nicalon	Unreinforced
mid dendrite	1.5	3.5	1.3
dendrite edge	3.5	3.6	2.8

In addition to coring, Table 4.1 also shows the difference in solute content in the reinforced regions of the ARE415 composites (although the results apply equally to the A201 composites). The variation in solute concentration gives an indication of how the billet solidifies. Thus solidification of matrix metal occurs first at the die walls and the preform as the melt comes into contact with a cooler phase. During this stage, solute is rejected ahead of the melt front and, as a consequence, there is a solute enriched-region at the last place to solidify. The EPMA data, Table 4.1, shows higher levels of solute present in the reinforced regions compared to the unreinforced alloy, indicating that it is the reinforced region that solidifies last, and is consistent with recent reviews [120, 121]. This also suggests that the second phases present around the fibres are there as a result of mass transfer and not due to nucleation or reaction. These observations also suggest that solidification of the matrix starts in the interfibre space and not at the fibre surface, which is in agreement with work by Lepetitcorps [73].

4.1.2(d) Fibre/Matrix Reactions

Examination of the Altex and Nicalon composite systems in the TEM gave no visual indication of a fibre/matrix interface reaction during processing, although some magnesium was located in surface regions of the fibre upto a depth of ~100 nm. EPMA of the cast composites revealed that the level of magnesium detected in the matrix was ~0.1 wt.% below the as-received specification of both ARE415 and A201 composites containing Altex fibres, and 0.2 wt.% below for Nicalon. The segregation of magnesium to the surface regions of the fibre has been found by a number of authors [38, 67, 85, 86, 122, 123]. With regard to wetting and improving infiltration, copper and magnesium additions to aluminium are known to reduce the contact angle between the molten alloy and fibre [116], in one or more of the following ways;

(a) by reducing the surface tension of the melt, γ_{LV},

(b) by reducing the interfacial energy, γ_{LS},

(c) by promoting a chemical reaction at the fibre/metal interface.

The reasons why magnesium segregates to the interface are unclear. It could be to reduce oxide, either in the fibre or on the surface of aluminium, or it may be that the magnesium has been rejected ahead of the melt front and is pushed towards the fibre surface, which remains hot longest.

Magnesium depletion in the matrix has been confirmed by EPMA and suggests a fibre/matrix reaction, as observed by a number of authors [124]. The likelihood of a reaction during processing may be discussed by reference to the appropriate Ellingham diagram, Figure 4.2, and reported energies of formation [84].

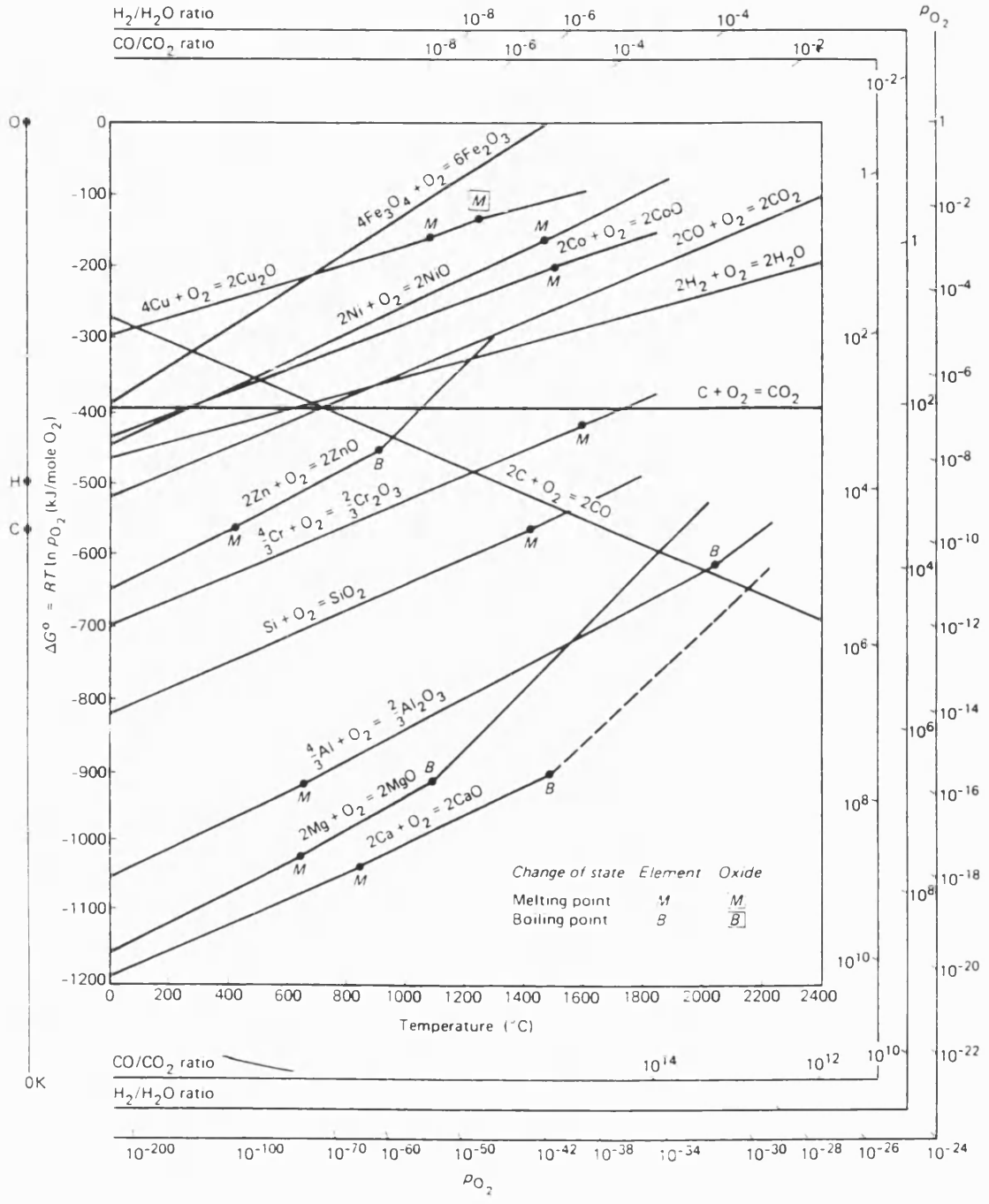

Figure 4.2 Ellingham diagram. After [125].

Altex

The Altex fibre, consists of alumina, Al_2O_3, and silica, SiO_2, and thus we may write;

$$3Mg + Al_2O_3 \rightarrow 3MgO + 2Al$$

where the free energy of formation, ΔG_f, is ~ -130 $KJmol^{-1}$

and for the silica component;

$$2Mg + SiO_2 \rightarrow 2MgO + Si$$

ΔG_f ~ -290 $KJmol^{-1}$

Both reactions have a large negative value for ΔG_f, indicating that they are thermodynamically possible, and both reactions lead to the formation of magnesium oxide, MgO. The reaction of magnesium with silica has a larger negative value of ΔG_f indicating that it is energetically more favourable. It is also possible for the magnesium oxide to react with both components of the fibre such that;

$$MgO + SiO_2 \rightarrow MgSiO_3$$

ΔG_f ~ -34 $KJmol^{-1}$

and

$$MgO + Al_2O_3 \rightarrow MgAl_2O_4$$

ΔG_f ~ -47 $KJmol^{-1}$

Neither of these complex oxides were, however, detected although it is possible that this is due to the small extent of reaction (processing times are short, solidification takes ~5 seconds, and so any reaction product would be small in size.). The reaction of magnesium with the silica is most favourable, but this yields silicon, which is likely to be ejected into the matrix, although none was found. Again this could be due to the small extent of reaction, as silicon is readily soluble in aluminium.

Nicalon

With regard to the Nicalon fibre, which consists of silicon carbide, silicon oxycarbide and free carbon, several reactions with magnesium may occur. Firstly we may write;

$$2Mg + SiC \rightarrow Mg_2Si + C$$

$\Delta G_f = -7\ Jmol^{-1}$

However, the small value of ΔG_f, indicates that the reaction will take place very slowly if at all. Secondly, reactions with carbon [126] may be expressed as;

$$2/3Mg + C \rightarrow 1/3Mg_2C_3$$

$\Delta G_f (\pm 552) = 15912 + 3.56T\ Jmol^{-1}K^{-1}$ (923-1150K)

and

$$1/2Mg + C \rightarrow 1/2MgC_2$$

$\Delta G_f (\pm 198) = 36056 + 0.5T\ Jmol^{-1}K^{-1}$ (923-1150K)

At the melt temperature (1123 K) values of ΔG_f are 19.9 $KJmol^{-1}$ and 36.6 $KJmol^{-1}$ respectively. The high positive values indicate that neither of these reactions are likely to occur.

Consider now the silicon oxycarbide phase. Work by Hicks [112] on Nicalon reinforced magnesium alloys found that extensive reaction occurred between the fibre and the metal. It was shown that the silicon in the reaction zone was bonded almost exclusively to carbon to give silicon carbide, and that the Si-O-C bonds could be readily broken. The following reaction was, therefore, proposed.

$$xMg + SiO_xC_y \rightarrow xMgO + Si + yC$$

Furthermore the oxycarbide phase is amorphous and is known to contain a large number of defects which would allow for easy diffusion (compare the densities of 2.6 gm^{-3} for Nicalon and 3.25 gm^{-3} for Altex). Thus it is likely that magnesium reacts

even more strongly with silicon oxycarbide than it does with silica. This could explain why more magnesium (0.2 wt.%) was lost from the matrix of the Nicalon composite than from the matrix of the Altex composite (0.1 wt.%). It is also possible that the aluminium could displace the silicon, but not to the same extent as the magnesium. A further point to consider is that the outer 200 nm of the Nicalon fibre is enriched with oxygen [33], which will also increase amount of reaction.

The oxycarbide reaction would imply the ejection of silicon and free carbon into the matrix, providing a further source of carbon for the formation of aluminium carbide according to [126].

$$4/3Al_{(l)} + C_{(s)} \rightarrow 1/3Al_4C_{3(s)}$$

$\Delta G_f (\pm 2800) = -88840 + 32.1T \text{ Jmol}^{-1}\text{K}^{-1}$ (933-2000K)

Whilst it is thermodynamically possible for a reaction to occur during processing of both Altex and Nicalon composites, $\Delta G_f \sim -53$ KJmol^{-1}, as observed by Chapman [124] when using the LMI route to manufacture Nicalon/aluminium composites, it is believed that the processing times involved in the manufacture of the ARE415 and A201 based composites are too short to cause a noticeable reaction.

4.1.2(e) Dislocations

Matrix dislocations were observed at the fibre interfaces for all of the Altex and Nicalon based composites and are associated with the difference between coefficients of thermal expansion (CTE) for the matrix and fibre. The CTE, α, for Nicalon is 3×10^{-6} K^{-1} and 23.6×10^{-6} K^{-1} for a strong aluminium alloy. Assuming a temperature change, ΔT, of 600 K on manufacture, the strain developed in the matrix, $\Delta\alpha\Delta T$, will be 1.2% for the Nicalon composite. This might be large enough to exceed the yield stress of the matrix and cause plastic deformation and a build up of dislocations and vacancies. Taking the Nicalon/A201 composite as an example the

estimated dislocation density of 9 x 10^{13} m^{-2} is in close agreement with work reported by Clyne and Withers [127], which records a density of ~8 x 10^{13} m^{-2}. The dislocation density was also observed to decrease with distance from the fibre/matrix interface in accordance with the above work and that of Cottu [128]. A prediction of the increase in dislocation density, $\Delta\rho$, may be made using the equation developed by Arsenault and Shi [129]

$$\Delta\rho = \frac{\Delta\alpha\Delta TNA}{b}$$

where N is the number of particles per unit volume, A the total surface area and b the Burgers vector. Assuming the number of particles to be 2.5 x 10^{9} m^{-3}, a total surface area of 5 x 10^{-5} m^2 and a Burgers vector of 2.5 x 10^{-10}m, the calculated dislocation density is 6 x 10^{-12} m^2. This is in agreement with the value estimated in this study.

4.1.2(f) Matrix precipitates

A non-uniform distribution of precipitate was observed in all of the Altex and Nicalon based composites. The LMI process takes the matrix regions to a high temperature followed by a quick solidification, unlike solution treatment though the alloy is heated above its liquidus. The actual mechanism of solidification from the casting process means that the solute elements were not homogeneously distributed, only certain areas would have the composition to form precipitates, accounting for the uneven distribution observed. The cooling stage of manufacture could be considered equivalent to ageing the composite at high temperature for a short time, for example 300°C for 10 - 30 minutes. If the precipitates nucleate at all stages in the cooling then a mixture of fine and coarse precipitates will be observed, the formation of Ω or θ being dependent on the localised solute levels. The high dislocation density would also give preferential sites for precipitation.

4.1.3 Monofilament Reinforced Cast Composite

The Sigma monofilament is significantly different to the Altex and Nicalon fibres with regard to diameter and composition. These differences will affect many microstructural aspects of the composite including grain size, dislocation density and interfacial reactions.

The Study of the Sigma/ARE415 composite was based on the initial hybrid composite, fabricated using the same conditions as the other systems except for a lower preform preheat temperature of 400°C. The composite was poorly infiltrated and showed that the polymeric binder had not been removed by preheating prior to infiltration. Thermogravimetric analysis (TGA) from an as-received fibre sample, gave two weight losses; the latter at ~525°C, indicated that the fibre must be heated in excess of 525°C to remove fully the binder. After TGA the Sigma fibres had a black appearance and EDS showed the presence of silicon and carbon, which may have provided an unwanted source of possibly reactive carbon at the fibre surface. Another problem when using this type of fibre preform arose when the tape was removed, resulting in a loss of fibre alignment. To wind the Sigma fibres in a similar way to the Altex and Nicalon fibres was not possible as the fibres cannot be bent to the same degree without fracture. Work on the Sigma fibre reinforced composites did not proceed further due to these difficulties.

4.1.4 The Effect of Heat-Treatment

The effects of heat-treatment are separated into solution treatment and artificial ageing.

4.1.4(a) Solution Treatment

All of the composites showed significant amounts of eutectic second phase and coring in the cast condition. To realise the full potential of the precipitation hardenable matrix alloy it is essential that the coring and second phases were removed, and a homogenised structure attained. This was achieved by a suitable solution treatment.

The solution treatment used for all composite systems, 500 ± 5°C for 6 hours and 530 ± 5°C for 18 hours, was developed on the ARE415 alloy. A two-stage solution treatment was used to prevent the burning of any low melting point magnesium phases which reportedly occurs at ~506-507°C [130]. The first stage takes the low melting point phases into solid solution, once this is done the temperature can be increased without being deleterious to the alloy. When applied to the composites the solution treatment gave two different results.

Altex reinforced composites

Solution treatment was effective on both matrices of the Altex reinforced composites, reducing levels of coring and second phase, with most of the second phase segregated around the fibres being dissolved. The matrix regions of the ARE415 matrix composite did, however, show the appearance of widespread porosity which was also observed in the unreinforced alloy.

Although there was no visible reaction at the interface between the Altex fibres and the matrix, the level of magnesium in the matrix was reduced when compared with the cast composite (~0.1 wt.%) and the unreinforced alloy (~0.2 wt.%). It may, therefore, be inferred that there has, to some extent, been a reaction, the thermodynamics of which are the same as discussed previously.

Assuming that the reaction layer is of uniform thickness, t, and is very small, then the volume fraction of reacted fibre is proportional to t / r, where, r, is the original radius of the fibre. Assuming a fibre radius of 6μm, a fibre volume fraction of 0.5 and a reaction thickness of 100nm, the volume fraction of reacted fibre can be estimated as ~0.018. If it is also assumed that there is 5wt.% of magnesium in the reacted zone (for EDS detection of a peak in the TEM there must be at least 5wt.% present) then a mass balance shows that ~0.2 wt.% of magnesium must have diffused into the fibre. This is consistent with the EPMA measurements which are ~ 0.2 wt.% below the as-received

alloy compositions. A high degree of confidence could be placed in the EPMA results as measurements were found to lie within ± 0.01 wt.% for magnesium.

Nicalon reinforced composites

Neither of the Nicalon-based composites were homogenised by solution treatment and both developed new second phases in the matrix and reaction products at the fibre/matrix interface. In addition the Nicalon/ARE415 composite exhibited widespread porosity to the same extent as the Altex/ARE415 composite and the unreinforced ARE415 alloy.

EPMA data from both composites after solution treatment revealed a decrease in the magnesium and aluminium content of the matrix and the presence of silicon. This is consistent with the reaction kinetics discussed in the previous section, i.e. diffusion of magnesium and aluminium into fibre and the ejection of silicon from fibre into matrix. Taking magnesium as an example, the level of this element was reduced by ~0.2 wt.% when the cast composites were compared to the compositions of both as-received alloys. Solution treatment has reduced the level of magnesium in the ARE415 matrix further by ~0.2 wt.% (~0.4 wt.% in total), and removed all traces in the A201 alloy matrix. Using the mass balance approach applied to the Altex composites a reaction thickness of ~150nm containing 10 wt.% of magnesium, constitutes to a loss of ~0.45 wt.% magnesium from the matrix, which is consistent with the EPMA data.

The new second phases formed in the composite matrices for the ARE415 and A201 alloy systems were slightly different, due to the difference in alloy compositions, but the reasons for their formation are the same. Consider the Al-Cu-Si phase diagram, Figure 4.3, which has a eutectic at 525°C. This eutectic lies inside the second stage solution treatment temperature. It is believed that the proximity of the $CuAl_2$ second phase to the fibre, coupled with the diffusion of silicon from the fibre into the matrix, promotes the formation of the previously mentioned Al-Cu-Si eutectic (found in the

A201 based composite matrix), which in turn leads to the other phases observed which are all Al-Cu-Si based (found in the ARE415 based composite which in addition to aluminium, copper and silicon contain zinc and or iron and manganese). The rounded morphology of the phases is consistent with some melting during the solution treatment.

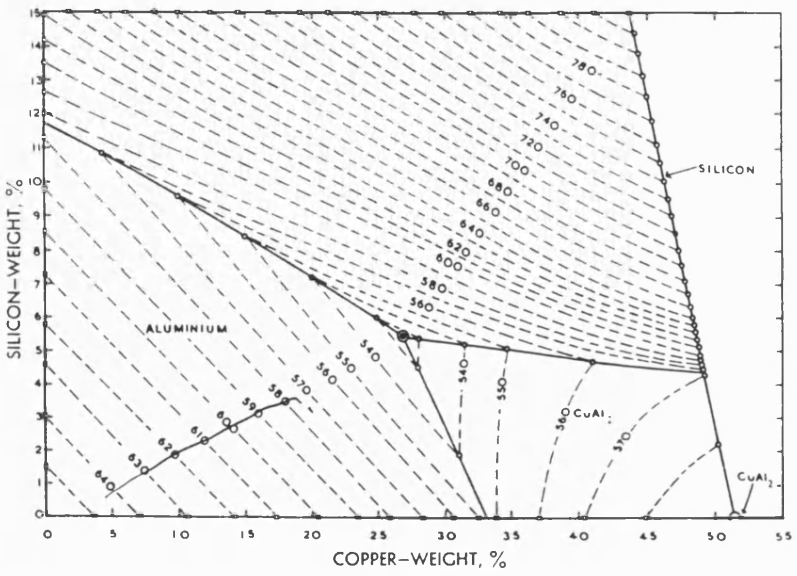

Figure 4.3 The Al-Cu-Si phase diagram. After [132].

Examination of both Nicalon-based composites in the TEM showed the reaction at the fibre/matrix interface to consist of two distinct features;

(i) a reaction layer of 100-200nm within the original fibre dimensions and

(ii) needles at the fibre matrix interface.

The reaction layer, (i), was larger in structural appearance that the polycrystalline nature of the unreacted fibre and EDS data showed the presence of magnesium and aluminium in addition to the fibre constituents of silicon, oxygen and carbon. Diffraction pattern analysis of the Nicalon/A201 composite in this region, indicated the

phase contained magnesium oxide, MgO, together with a magnesium-aluminium-oxygen phase, believed to be the $MgAl_2O_4$ spinel [124].

Diffraction pattern analysis from the Nicalon/ARE415 composite was less conclusive. Analysis of the reaction layer revealed the presence of some amorphous material, which did not correspond to the β-silicon carbide of the unreacted fibre; in fact aluminium was the closest match (a = 4.096). This evidence suggests that there is some diffusion of aluminium into the fibre, probably reacting with the oxycarbide phase. There is no conclusive evidence for the formation of MgO or $MgAl_2O_4$, but they cannot be discounted. The thermodynamics of formation are favourable, both MgO and $MgAl_2O_4$ are cubic (like aluminium), the lattice spacing for MgO, a = 4.12, is close to that of aluminium (a = 4.096) and the results from the Nicalon/A201 composite suggest the formation of the phases.

The needles growing from fibre into matrix can be accounted for by the reaction of aluminium with either the free carbon or the carbon released from the fibre by the reaction with magnesium. Similar carbide formations have been observed by other authors [86, 124] according to [126];

$$4/3Al_{(s)} + C_{(s)} \rightarrow 1/3Al_4C_{3(s)}$$

$$\Delta G_f (\pm 2800) = -71965 + 13.95T \text{ Jmol}^{-1}\text{K}^{-1} \quad (298\text{-}933\text{K})$$

giving a free energy of formation (ΔG_f), of ~ -61 $KJmol^{-1}$ for a temperature of 800K, showing that this reaction is highly favourable.

With regard to the possibility of a magnesium carbide reaction [126];

$$2/3Mg + C \rightarrow 1/3Mg_2C_3$$

$$\Delta G_f (\pm 140) = 27787 - 9.8T \text{ Jmol}^{-1}\text{K}^{-1} \quad (293\text{-}923\text{K}) \text{ and}$$

$$1/2Mg + C \rightarrow 1/2MgC_2$$

$\Delta G_f (\pm 170) = 45319 - 9.7T$ $Jmol^{-1}K^{-1}$ (293-923K)

thus the free energies of formation (ΔG_f) are ~20 $KJmol^{-1}$ and ~38 $KJmol^{-1}$ respectively, which are both large and positive indicating that the formation of these phases is unlikely.

Summarising the solution treatments, a number of features are apparent;

(a) the solution treatment is effective in removing coring and second phase from the Altex/ARE415 and Altex/A201 composites. Only a small amount of second phase is retained and this has been identified as an iron- and manganese- containing intermetallic, which is hard to remove by solution treatment because of its high melting point and slow diffusivity. There is a small reaction between the fibre and the matrix.

(b) The solution treatment is ineffective for the Nicalon composite systems, promoting reactions at the fibre/matrix interface and the development of new second phases in the matrix.

(c) All of the ARE415 based composites developed widespread porosity on solutionising, as did the unreinforced alloy.

The disturbing side-effect from solutionising the ARE415 based composites was high levels of matrix porosity, which were found to increase with increasing solution treatment temperature. The circular nature of the porosity indicated the release of trapped gas, and it is believed that hydrogen is dissolved by the alloy either during the LMI process or prior, since the thermal history of the alloy is unknown. The fast solidification time associated with the manufacture keeps the hydrogen in solution, super saturating the alloy; the gas bubbles are compressed but not eliminated. On

subsequent heating the hydrogen starts to diffuse, forming molecular hydrogen, and opening up pores and blisters on the surface of the alloy; this is supported by the work of Hess and Turnbull [132]. Since close control (±1°C) of the heat treatment temperature was possible during processing, the alloy remained below the eutectic temperature (no grain boundary liquation was observed on subsequent examination), indicating that porosity was not a result of accidental overheating. Degassing the ARE415 melt prior to infiltration was considered to alleviate the problem. Typical degassing agents are argon, chlorine and hydrochloroethane. Chlorine was ruled out as it removes magnesium from the melt and hydrochloroethane was also avoided from a safety point of view. An attempt was made to degas the melt with argon but this failed. Considering that the porosity would have had a deleterious effect on mechanical testing no further work was carried out using this alloy for composite fabrication.

4.1.4(b) *Ageing*

Ageing studies were performed at 175°C. This temperature was selected to promote the growth of Ω precipitates, as used in work by Kerry et al [43]. A summary of hardness and precipitation behaviour is presented in Table 4.2.

The precipitation response for both Altex and Nicalon composites was quite different to that of the unreinforced A201 alloy. In both cases θ' was formed, which is less effective with regards to strengthening and thermal stability compared with Ω. The change in precipitate type is considered to be related to the reduction of magnesium levels in the matrix caused by magnesium diffusion into the fibre. As a consequence the likelihood of Ω formation would be reduced and the proportion of θ' which is formed would be increased. This has been demonstrated in previous studies [46] where the magnesium content was varied and the precipitate densities measured; when the magnesium content was high (0.74 wt.%) the maximum precipitate densities were 2×10^{22} m^{-3} for θ' and 10×10^{22} m^{-3} for Ω, which compared to 12×10^{22} m^{-3} for θ'

Table 4.2 Summary of composite and alloy ageing characteristics.

condition		Hardness HV		time to peak	precipitate	precipitate size (nm)		precipitate density
			scatter	hours		thickness	diameter	x $10^{21}m^{-3}$
Altex/A201	**cast**	96			θ			
	peak-aged	160	± 10	2	Ω, θ'	3	20-50	1
	over-aged				Ω, θ'	10	60-100	0.1
Nicalon/A201	**cast**	86			-			
	peak-aged	104	± 5	2-4	θ'	10	100	0.3
	over-aged				θ'	10	>200	0.1
A201	**cast**	62			θ			
	peak-aged	150	± 4	7	θ'	10	50-100	1
	over-aged				θ'	10	100-150	2

and 6 x 10^{22} m^{-3} for Ω when the magnesium content was low (0.23 wt.%). A further factor governing the formation (and amount) of Ω is the Cu : Mg ratio for wt.% [40, 41]. Previous work has shown Ω will form when the ratio is 5 : 1 and that the optimum ratio is about 15 : 1, variations above or below this may produce only sparse amounts of Ω if any. Looking at the Altex composite the ratio is 52 : 1, clearly above the critical value and in the case of the Nicalon composite all of the magnesium had reacted with the fibre. The poor ageing response of the Nicalon composite was due to the reactions and the non-homogenisation of matrix prior to ageing. It was interesting to note that the density of precipitates in both composite systems was not significantly different from that in the alloy despite the presence of a high dislocation density associated with the residual stresses in the composites. In the case of Ω precipitation the Ag addition has been shown to increase the precipitate density [49, 133-135], this may also be the case for the θ' precipitates.

In addition to a change in precipitation, the ageing curves from both Altex and Nicalon composites showed three main differences compared with the unreinforced alloy

(i) time to peak-hardness,

(ii) stability of precipitation and

(iii) scatter of results.

The time to peak-hardness for both composites was less than that of the unreinforced alloy, attributed to the observed increase in dislocation density around the reinforcement produced by thermal expansion mismatch on cooling [136]. The dislocations act as preferential sites for nucleation sites.

The precipitation in the both Altex and Nicalon composites appeared to overage faster, with the hardness falling earlier than the unreinforced alloy this may have been due to the mode of precipitation. Both composites show only θ' type precipitates, while the unreinforced alloy produces Ω and θ' precipitates. The Ω precipitate is known to give a

greater hardening response and is thermally stable, where-as the θ'-type of precipitate will eventually coarsen and form the equilibrium θ precipitate. This was evidenced by TEM analysis which showed that even after 1000 hours (over-aged) there was little change in the Ω precipitate size compared to the peak-aged condition, changing from 50-100nm to 100-150nm in diameter in the over-aged condition. The θ' precipitates however, increased from 20-50nm up to 100nm in the over-aged Altex composite, and >200nm in the over-aged Nicalon composite. The precipitate sizes observed appeared slightly larger than those reported by Scott using an ageing temperature of 140°C [46], his work based on the ARE415 alloy shows θ' and Ω growing from ~10nm after 2 hours up to ~50nm after 1000 hours. Scott also reported precipitate densities of $3x10^{22}$ m^{-3} and $8x10^{22}$ m^{-3} for Ω and θ' respectively after 5 hours, falling to $1x10^{22}m^{-3}$ at 1000 hours. These results are a magnitude higher than those of this study, which may be due to a difference in ageing temperature, alloy composition or the method used to estimate the density.

The scatter of the hardness results was greater for both of the composite systems, which may be due to variations in the proximity of an indent relative to a fibre, although attempts were made to keep this constant. In the case of the Nicalon composite a homogenised structure was not obtained, which accounts for the variation in results. The validity of using microhardness measurements to assess the effects of reinforcement on the matrix have been questioned, but provided the indentor does not impinge on the fibres it can be used as a fair indication of the ageing response. In the case of unidirectional composites the use of sections transverse to the fibre reduces the chance of any sub-surface impingement on fibres giving erroneous readings.

The fact that the matrix hardness for both composite systems was less than the unreinforced alloy can partly be attributed to the change in precipitation mode, but it is generally considered that the presence of the reinforcement acts to increase the matrix hardness to some extent [38]). The degree to which the reinforcement increases the

matrix hardness will decrease the further away from a fibre an indent is made, and it will also decrease if the fibres are not closely spaced.

4.2 Mechanical Behaviour

The mechanical behaviour of all the composite systems is considered in two parts - elastic behaviour, and plastic behaviour leading to final fracture.

4.2.1 Elastic behaviour

The elastic properties were determined from the initial linear regions of the stress-strain curves for all composite systems in both longitudinal and transverse tension. A summary of the measured longitudinal and transverse composite modulus is presented in Table 4.3, with 'rule-of-mixtures' (ROM) predictions included for comparison.

Table 4.3 Summary of measured and calculated modulus.

Composite	**E_1 (GPa)**		**E_2 (GPa)**				
	Exp.	**4.4**	**Exp.**	**4.5**	**4.6**	**4.7i**	**4.7ii**
Altex/ARE415 cast	110 ± 20	119					
Altex/A201 cast	120 ± 14	136	70 ± 26	104	115	34	73
peak-aged	145 ± 19	134	64 ± 11	100	116	38	84
Nicalon/A201 cast	107 ± 12	126	90 ±4	100	110	33	66
peak-aged	128 ± 16	124	93 ± 10	95	105	31	64
over-aged			99 ± 10	106	116	35	70

4.2.1(a) Longitudinal Modulus

First consider the longitudinal modulus, E_1, taking the Altex/A201 system in the cast condition as an example. The measured modulus is 120 ± 14 GPa, and the ROM is given by

$$E_1 = E_f V_f + E_m (1-V_f) \qquad \text{Eqn. 4.4}$$

where E_f and E_m are Young's modulus for the fibre and matrix respectively, and V_f is the fibre volume fraction. Substituting the experimental value for E_m of 73 GPa, the manufacturer's figure of 210 GPa for E_f, and taking V_f equal to 0.46 gives a value of 136 GPa for E_1. The measured value is in close agreement with the ROM prediction, as is the case for all other composite systems. This indicates that the fibre and the matrix were contributing fully to the longitudinal modulus and that the interface bond produced was strong. Johnstan [137] reports that additions of magnesium to aluminium alloys provides a strong fibre/matrix bond, the strength of which increases with magnesium content. The experimental scatter in the results was due to the inherent variability of composite materials. There was no significant difference in the modulus after heat treatment, showing that any reaction is not detrimental to load transfer. Comparing the different fibres, which have approximately the same modulus, no obvious advantage was gained by using one fibre in preference to the other.

4.2.1(b) Transverse Modulus

The measured transverse modulus, E_2, for each composite was compared to several theoretical ROM predictions, Equations 4.5 - 4.7, and collated in Table 4.3. The measured values of modulus were different for the Altex and Nicalon based composite and so each system will be considered separately.

Altex reinforced composites

The first equation

$$E_2 = \frac{E_f E_m}{E_f(1-V_f)+E_m V_f} \qquad \text{Eqn. 4.5}$$

is based upon a 'plates in series' model by Reuss, where E_f and E_m are Young's modulus for the fibre and matrix respectively, and V_f is the fibre volume fraction. Taking the Altex/201 composite in the cast condition as an example the measured modulus is 70 ± 26 GPa. Substituting the experimental value for E_m of 73 GPa, the manufacturer's figure of 210 GPa for E_f, and taking V_f equal to 0.46 gives a value of 104 GPa for E_2, higher than the measured value. The interfacial bond strength of this composite has already been shown to be strong, and so the low modulus value measured was surprising. The reason for the low modulus can be accounted for when the voids present at touching fibres are considered. These reduce the surface area of interfacial bonding and reduce the efficiency of load transfer, thus reducing the modulus. The scatter present in both cast and peak-aged Altex/A201 composites was large and is an indication of the variability of touching fibres and voids within these composites.

The measured values of transverse modulus for the Altex composites are now compared to the second equation

$$E_2 = \frac{E_f E_{m'}}{E_f(1-V_f)+E_{m'}V_f} \qquad \text{Eqn. 4.6}$$

which is also based on the ROM model of Reuss, but accounts for Poisson's contraction effects in the matrix, $E_{m'}$, where

$$E_{m'} = \frac{E_m}{1-\upsilon_m^2}$$

and υ_m is the Poisson's ratio of the matrix. Using the values of E_f, E_m and V_f defined previously and taking the value of υ_m as 0.34 [81] gives a value of 115 GPa, which is again higher than the measured value of 70 GPa for Altex/201 in the cast condition. The reasons for the difference are the same as described previously and apply to all the Altex composites.

Finally the measured values of transverse modulus for the Altex composites can be compared to

$$\frac{E_2}{E_m} = \left[\frac{X}{\{1-X(1-R)\}+(1-X)}\right] \qquad \text{Eqn. 4.7}$$

which follows a geometric approach proposed by Phillips [90] assuming a uniform square array of fibres with square cross-section; where R = Em/Ef and X is the side of the square fibre. The upper and lower limits for X being d and $d/2^{1/2}$, where d is the fibre diameter. Again using the cast Altex/A201 as an example and substituting the previously defined values of E_m and E_f, R = 0.35 and X_L and X_U of 8.5μm and 12 μm respectively, gives upper and lower modulus predictions of 73 GPa and 34 GPa. The measured modulus 70 ± 26 GPa is in excess of the lower limit and in close agreement with the upper limit. This model assumes a uniform square array of fibres and so the fact that the upper limit provides a good prediction is one of chance.

Nicalon reinforced composites

Looking now at the transverse modulus for the Nicalon composites, which was on average higher than the measured values for the Altex composites. First compare the measured values with the value predicted by Equation 4.5. Taking the Nicalon/A201 composite in the cast condition as an example the measured modulus is 90 ± 4 GPa. Substituting the experimental value for E_m of 73 GPa, the manufacturer's figure of 200 GPa for E_f, and taking V_f equal to 0.42 gives a value of 100 GPa for E_2, this is in

close agreement with the measured value of 90 ± 4 GPa, inferring a strong interfacial bond. This is the case for all the Nicalon systems and suggests that there were less fibres touching and voids in these composites than the corresponding Altex/A201 composites.

When the measured transverse modulus of the Nicalon systems were compared to predictions incorporating Poisson contraction effects, Equation 4.6, the average modulus values were lower than the predicted values, for example in the peak-aged condition the measured modulus is 93 ± 10 GPa compared to a predicted value of 105 GPa. If the scatter is accounted for the measured values were in good agreement with the predictions. This model has been used in the past because Equation 4.4, generally provides an underestimate of the composite modulus. If the distribution of flaws and fibres can be improved (when using an LMI route) then this model will provide an accurate prediction for the transverse modulus.

Comparison with the geometric model, Equation 4.7, shows the measured values in excess of all the predictions. This suggests that the model is inadequate for predicting the transverse modulus for composites produced by LMI where the fibre distribution does not approximate to a uniform square array.

4.2.2 *Plastic behaviour*

The stress-strain curve for MMCs has in general been found to exhibit three stages [69, 138]. There is an initial linear region in which the fibres and matrix both behave elastically. This is followed by a reduction in gradient where the matrix behaves plastically and the fibres elastically. Finally there is a further reduction in gradient, which Piggott refers to as a small pseudo-elastic region, associated with the fibres breaking into short lengths.

4.2.2(a) *Yielding behaviour*

All of the composite systems studied, whether in the cast or peak-aged condition, exhibited knee-points in the longitudinal stress-strain curves. This behaviour is associated with the commencement of yield in the matrix [138], which has been confirmed by Chen [139] who found slip lines (an indication of plastic deformation) in the matrix above the knee-point, but not below the knee-point.

Since the knee-point is reported to occur at the matrix yield strain [138], a theoretical prediction of the knee point can be made by taking the point of intersection between a line representing ROM behaviour, Equation 4.8, and a line representing ROM behaviour after the matrix has yielded, Equation 4.9.

Line 1 $$\sigma_c = \varepsilon E_m(1-V_f) + \varepsilon E_f V_f$$ Eqn. 4.8

Line 2 $$\sigma_c = \sigma_y^m(1-V_f) + \varepsilon E_f V_f$$ Eqn. 4.9

Where σ_c is the composite stress at a strain ε, E_m and E_f are the Young's modulus of the matrix and fibre respectively, V_f is the fibre volume fraction and σ_y^m, is the stress level of the matrix at yielding.

The average experimental stress-strain response for the Altex/201 composites, in the cast and peak-aged conditions is plotted in Figure 4.4, together with values calculated using Equations 4.8 and 4.9. The other composite systems all followed the same trends and so comments referring to the yielding behaviour are equally applicable.

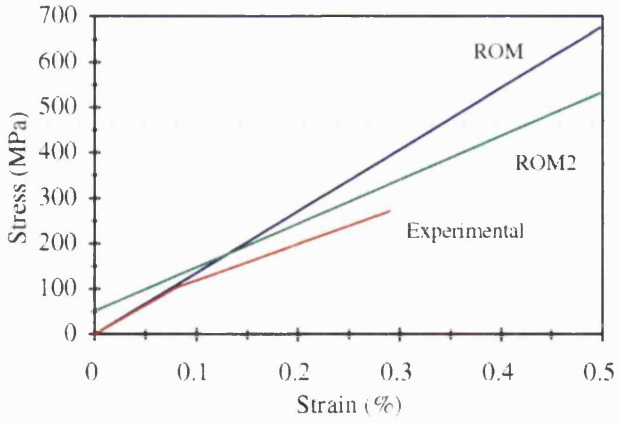

(a)

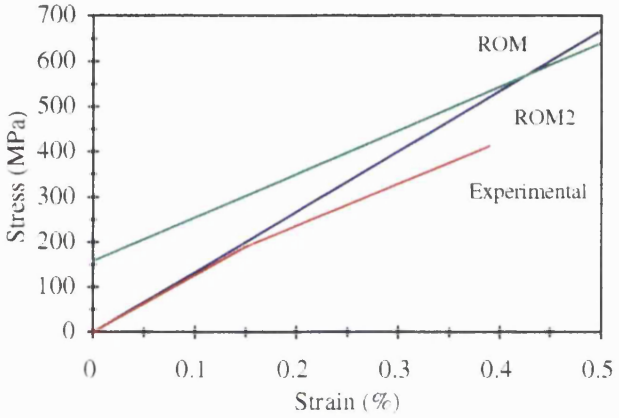

(b)

Figure 4.4 Comparison of experimental composite knee-point with theory, Altex/A201: (a) cast; (b) peak-aged.

It can be seen that the knee-point measured experimentally occurs at a reduced stress and strain when compared with the theoretical calculations and the experimental data for the unreinforced alloy. This has also been observed by Chen [100]. This can be due to (a) strain magnification occurring in the matrix causing the matrix to apparently yield prematurely, or (b) residual stresses in the matrix from manufacture act in addition to the apparent stresses. Some workers report that the residual stress has only a small contribution, ~20MPa, [140], but other workers have reported much larger stresses ~200MPa. After casting, the matrix will be in longitudinal tension and so the

yield stress will be lower than expected. In the peak-aged condition the difference between experimental and theoretical results is much greater. In this case the residual stress is likely to be relieved by the ageing stage and so should not be significant. The most probable reason for the discrepancies is that the composite contained θ' matrix precipitates rather than the Ω precipitates present in the unreinforced alloy and, as is well known [43], the hardening response of θ' is less than Ω. This is also evidenced by quoted proof-stress values of ~320 MPa and ~520 MPa for wrought alloys containing the respective precipitates [44]. The increase of yield stress on ageing is associated with precipitates in the matrix which hinder dislocation movement and raise the level of the stress-strain curve.

The transverse stress-strain curves for both Nicalon and Altex composites were similar, with evidence that the matrix yield stress increased with ageing, as would be expected. This is evidenced by comparing the yield stress for the Nicalon/A201 composite in the cast and over-aged condition, which are ~70 MPa and 100 MPa respectively.

4.2.2(b) Fracture

Longitudinal

Now consider the longitudinal tensile strength, σ_1, for the composites. Table 4.4, shows the measured values with the ROM value, Equation 4.10, for comparison.

$$\sigma_1 = \sigma_f V_f + \sigma_{m'} (1-V_f) \qquad \text{Eqn. 4.10}$$

Where σ_f is the fibre strength, $\sigma_{m'}$ the matrix stress level at fibre failure strain and V_f the fibre volume fraction. Although this equation is not an accurate prediction of the composite strength [9] it does provide an estimate for the upper bound. Taking the Altex/A201 composite in the cast condition as an example, using the manufacturer's value of 1.8 GPa for σ_f and measured values of 140 MPa for $\sigma_{m'}$ and 0.46 for V_f, gives a predicted strength of ~900 MPa. The measured value, 272 ± 31, falls well

below the ROM prediction. This was the case for all of the composite systems investigated, the measured composite strengths being no better than the unreinforced alloy strength. There are two possible explanations for the low strengths, (1) low fibre strength or (2) low resistance to crack propagation.

Table 4.4 Summary of measured and calculated strengths.

Composite	σ_1 (MPa)		σ_2 (MPa)		
	Exp.	4.10	Exp.	4.11	4.12
Altex/ARE415 cast	300 ± 10	918			
Altex/A201 cast	272 ± 31	904	105 ± 8	63	77
peak-aged	413 ± 66	977	85 ±26	105	129
Nicalon/A201 cast	227 ± 36	1257	125 ± 13	72	85
peak-aged	266 ± 31	1278	104 ± 12	120	143
over-aged			108 ± 18	113	134

With regard to the fibre strength, it is possible that this is below that quoted by the manufacturer, either due to damage during preforming or a reaction. Indeed, Chapman [141] found that the strength of Nicalon fibres extracted from aluminium based composites was only 740 MPa after casting and 280 MPa after heat-treatment, compared with manufacturer's data of 2.8 GPa. Yajima et al [99] quote the tensile strength of Nicalon to be 2450 MPa, and then in an LMI manufactured aluminium composite report the fibre strength to be 2000 MPa. Clearly there are large discrepancies associated with the strength of this fibre. The formation of reaction products such as carbide needles also causes problems, as these create stress

concentrations at both the surface of the fibre, due to pits formed by consumption, and at the sharp tip of the needles [82]. To the same extent the fibres may be expected to lose strength during filament winding. The values of strength measured would correspond to fibre strengths in the order of a few hundred MPa, and this is in agreement with the findings of Chapman.

It has been considered that the longitudinal composite strength can be described by the resistance to crack propagation. Two cases are proposed [142];
(1) Cracks formed by the breakage of weak fibres are arrested and the strength of the composite is determined by stress concentration factors.
(2) Cracks can propagate and the strength is determined by crack propagation.

The mechanism which operates depends mainly upon, (a) the work per unit volume required to fracture the matrix and (b) interfacial bond strength, τi. When the work per unit volume is high then cracks can be suppressed for both strong and weak interfacial bonding, but when the work per unit volume is low then cracks are suppressed by weak interfaces but not strong. This means that for low ductility matrices there is an optimum interfacial bond strength to achieve high composite strengths. The scatter of the strength of fibres must also be taken into account, firstly due to the inherent flaws present in the fibres, and secondly due to stress concentrations caused by reaction needles and other surface flaws.

The idea of fibre/matrix bonding being 'too-good', has been described by other authors [11, 96], and is considered to be the case for the composite systems looked at in this study. The reason for the high bond strength can be attributed to a chemical reaction at the interface due to the diffusion of magnesium. The effects of magnesium additions to aluminium alloys on tensile strengths have been reported to show that composite strength to falls with increasing magnesium levels [143, 123]. Zabolotsky [144] reports an optimum bond strength to achieve the best properties.

The scatter of the results is greatest for the strength measurements, and highlights the intrinsic variability of composite materials. Cook [67] reports that high levels of copper containing second phases at the fibre surface strongly influence the composite strength and produce a greater scatter in results. In this study there were large amounts of intermetallic $CuAl_2$ at the fibre surfaces in the cast condition, but when this was removed after solutionising there was no reduction in the scatter of results, for example the strength of Nicalon/A201 composite in the cast condition was 227 ± 36 MPa and in the peak-aged condition, 266 ± 31 MPa. This suggests that intermetallic segregation was not an important factor in the failure strength.

Low strength seems unavoidable for these composite systems and it must be decided whether high tensile strength is an important objective or if properties such as yield strength, elastic modulus and toughness are more desirable.

The low measured strain to failure is close to that reported in the manufacturer's specifications for the fibre. Hu [97] Reports that for longitudinal properties, flaw propagation within fibre bundles results in a low failure strain.

Transverse

The measured values for the transverse strength, σ_2, are summarised in Table 4.4, with ROM predictions, Equations 4.11 and 4.12, included for comparison. The equations used to predict, σ_2, are based on the assumption of a weak interfacial bond such that the fibres are treated as a series of holes and the effective load bearing cross-section of the matrix is calculated. For fibres in a uniform square array we may write

$$\sigma_2 = \sigma_m\left(1-\sqrt{\left[\frac{4V_f}{\pi}\right]}\right) \qquad \text{Eqn. 4.11}$$

and for fibres in a uniform hexagonal array

$$\sigma_2 = \sigma_m\left(1-\sqrt{\left(\frac{2\sqrt{3}V_f}{\pi}\right)}\right) \qquad \text{Eqn. 4.12}$$

where σ_m is the matrix failure strength and V_f the fibre volume fraction. An estimate for the upper value of transverse strength is given by the strength of the matrix.

Consider first at how the measured values of transverse strength for the Altex/201 composites compare with the values predicted by Equations 4.11 and 4.12. Using values of 267 MPa for σ_m, and 0.46 for V_f as measured on the cast alloy and composite respectively, we obtain a strength of 63 MPa for a square array and 77 MPa for an hexagonal array (Equations 4.11 and 4.12 respectively). The measured value 105 ± 8 MPa was greater than both the predicted values inferring some degree of interfacial bonding. Substituting a value of 448 MPa for σ_m in the peak-aged condition, gives predicted values of 105 MPa and 129 MPa for a square and hexagonal array of fibres respectively. The measured value 85 ± 26 MPa was lower than the predicted values, a possible explanation being weak interfacial bonding. Analysis of the fracture surfaces shows, however, strong interfacial bonding for both conditions. This suggests that the transverse strength is controlled more by the distribution of flaws, such as touching fibres and voids in the matrix. Similar conclusions can be drawn from the Nicalon/A201 composites.

For both the Altex and Nicalon composites the average values in the cast condition were higher than the values in the peak-aged condition. Owing to the large scatter of the results it is hard to ascertain if this was a genuine result due to the interfacial reactions, or a measure of the variability of composite integrity.

It has been determined earlier that the type of the precipitation found in the composite matrix was different from that in unreinforced alloy. This makes comparisons difficult because essentially the materials are different, but the presence of θ' precipitates should

provide some increase in the strength. The fact that it does not also supports the belief that it is the distribution of flaws, such as porosity, touching fibres and reaction products, which dominates the strength. This means that the composite integrity was not as high as anticipated, the transverse behaviour being much more susceptible to flaws than the longitudinal behaviour.

The failure strain was much lower than that of the unreinforced alloy, Hu [97] reports that transverse failure is low because of high hydrostatic stresses in the matrix coupled with void nucleation at the fibre/matrix interface.

Comparing the measured values for the mechanical properties with those reported in the literature, Table 1.2, shows the modulus and strength values to be in close accord with similar systems. For example the Al-4Mg reinforced with 0.44 V_f alumina, has a longitudinal tensile strength of 570 MPa, which falls to 400 MPa at V_f of 0.3, with a transverse strength of 140 MPa. These values compare to longitudinal and transverse strengths of 413 ± 66 MPa and 85 ± 26 MPa respectively for Altex/201 in the peak-aged condition.

The values for the longitudinal strength may not be as disappointing as they first appear, since it may not be right to compare the failure strength of the composite with that of the alloy when they fail at widely different strains (e.g. 0.3% and 4% in the peak-aged condition). Indeed, if the strength of the alloy at the composite failure strain is compared with the composite strength then there would appear to have been significant improvement, see Table 4.5.

Table 4.5 Comparison of composite strength with alloy strength at composite failure strain.

composite	composite strength (MPa)	alloy strength at composite failure strain (MPa)
Altex/ARE415 (L), cast	300 ± 10	225
Altex/A201 (L), cast	272 ± 31	140
Altex/A201 (L), peak	413 ± 66	275
Nicalon/A201 (L), cast	227 ± 36	140
Nicalon/A201 (L), peak	266 ± 31	175
average transverse	100-125 ± 15	100

A further factor to consider is the importance of the yield strength. If designing a composite for use in a structural application is it wise to exceed the yield strength? Below the yield strength the composite is approximately as strong as the unreinforced alloy, but twice as stiff (depending on V_f). Böhm [145], however, suggests that long fibre composites must be designed for use in the plastic range of the matrix to take advantage of the potential of composite properties.

4.3 Future Prospects

4.3.1 Fibres

Of the three fibres initially considered in this project only Altex and Nicalon were fully investigated. Both of these fibres had similar mechanical properties but different chemical compositions. The Altex fibre was less reactive and was, therefore a better candidate for the particular alloys investigated. It may however, be argued that neither the Altex or the Nicalon fibre were suitable and that more stable fibres should be sought, preferably without the SiO_2 phase which is a problem for reactions. Indeed, attempts have been made to reduce the amount of oxycarbide phase in the Nicalon

fibres. A better fibre would probably have been the Sigma monofilament, since this should have given increased thermal stability remaining inert to magnesium, but the composite manufacturing problems need to be overcome. It may also be possible to use carbon fibres as recent work reports that pitch-based fibres do not react during composite fabrication [146].

4.3.2 The Matrix

The choice of matrix has been shown to be important and evidenced by the similarities and differences found between ARE415 and A201.

(i) Composition

Although both alloys form the required Ω precipitate, they have significantly different compositions. The A201 does not contain zinc and has higher levels of copper and silver, but less magnesium. Silver is important to increase the density of precipitates of Ω and the copper : magnesium level is important in its formation. So these alloys may yield different precipitation results.

(ii) Mechanical properties

Although ARE415 was studied only in the cast condition, a comparison of properties can still be made. Both alloys had a similar modulus ~70 GPa and strength ~270 MPa, but the ARE415 had a higher yield stress at 165 MPa compared with 96 MPa for the A201. The ARE415 was also more brittle failing at 1.1% compared with 14% for A201.

Both matrices reacted with both Altex and Nicalon fibres, the latter being the least stable. The A201 composites failed to develop Ω, but with higher levels of magnesium present in the ARE415 composites some Ω precipitation may have occurred after heat treatment. Although Ω is required for its thermal stability the presence of magnesium (required for its formation) may not be a good thing. The magnesium aids infiltration

and gives a strong chemical bond at the interface, but it is likely that this is also the reason for the low tensile strengths. Recent work [123, 143] has shown the tensile strength of aluminium based composites decreases with increasing amounts of magnesium additions. It must therefore be decided if a high tensile strength is what is really required. If so a different matrix may be needed.

Out of the systems looked at the one with the best potential is probably A201 combined with Sigma fibres.

5.0 CONCLUSIONS & FURTHER WORK

Liquid metal infiltration provides well consolidated composites, <1% porosity and volume fraction up to ~0.5, when either Altex or Nicalon fibres are used in conjunction with ARE415 (4 wt.% Cu -1 wt.% Mg-0.5 wt.% Ag) and A201 (4 wt.% Cu-0.3 wt.% Mg-0.7 wt.% Ag) aluminium alloys. The important parameters for success with these systems are a superheated alloy melt temperature of 850°C, an initial applied pressure of 7 MPa followed by consolidation at 25 MPa, with the ram and die preheated to 450°C and the preform to 700°C.

The Sigma monofilament was not successfully infiltrated due to the incomplete removal of the polymeric tape binder prior to infiltration. The preheating left a charred carbon residue on the fibres. Further work was prevented because of the difficulty in producing a preform of suitable dimensions for the equipment available; this was due to the large diameter and brittle nature of the fibre.

The Altex and Nicalon reinforced composites exhibited a typical cast structure with coring and interdendritic $CuAl_2$ segregated to the fibre surfaces. Magnesium diffused into the outer 100-200 nm of the fibres during the metal infiltration stage, the thermodynamics inferring a reaction. The Nicalon fibre was more receptive to magnesium than the Altex fibre, depleting the matrix by ~ 0.2 wt.% compared with ~ 0.1 wt.% for Altex reinforced matrices.

The solution treatment, 500 ± 5°C for 6 hours followed by 530 ± 5°C for 18 hours, reduced further the level of magnesium in both matrices as a consequence of diffusion into the fibres. For both matrices the solution treatment was effective for the Altex composites, but not for the Nicalon reinforced composites where silicon containing phases were formed in the matrix. In addition the Nicalon composites showed a noticeable change in structure in the outer 200nm of the fibres and the formation of

needles of aluminium carbide, Al_4C_3, at the fibre surface. This is attributed to reaction with the silicon oxycarbide constituent of the fibres.

The ARE415 alloy composites developed widespread porosity due to the release of trapped hydrogen gas, which halted further use of the alloy for composite fabrication. Further studies used only the A201 matrix composites.

The presence of fibres caused accelerated ageing in the composites compared with the unreinforced A201 alloy, reducing the time to peak hardness. The depletion of magnesium from the matrix, caused the formation of the θ' precipitate instead of the desired Ω precipitate. The effect of magnesium on the ageing response and mechanical properties of the composite is the major area to consider in future work. It should be investigated if supplementing the magnesium content of the A201 alloy, or using ARE415 alloy will promote the formation of Ω precipitates in the peak aged composite. The properties developed using these composites should then be compared with the those which develop only θ' precipitates.

The longitudinal stress-strain curves for the composites exhibited two stages. The curves remain linear up to a knee-point, followed by a linear region of reduced gradient until final fracture. The longitudinal modulus for both Altex and Nicalon systems, taken from the initial linear region of the stress-strain curve, was in accordance with the 'rule-of-mixtures' calculation, showing good load transfer and a strong interfacial bond. This may be associated with the magnesium in the matrix which promotes a chemical reaction at the fibre/matrix interface. The transverse modulus for all composites was strongly influenced by porosity and touching fibres, which made comparisons with theoretical predictions hard.

The knee-point in the stress strain curves was characteristic of the onset of matrix yielding. The yielding of all composite systems occurred at a reduced stress and strain

compared with the unreinforced alloy, due to the effects of residual stress in the matrix. The yield stress increased after ageing due to precipitates hindering dislocation movement, this increase was not to the extent expected because of the formation of the θ' precipitate rather than the Ω precipitate.

The longitudinal strength was lower than a 'rule-of-mixtures' calculation due to low fibre strength and a combination of high interfacial bond strength and low matrix ductility, causing brittle failure. The longitudinal strength of the Nicalon composite in the peak-aged condition was reduced by the presence of aluminium carbide needles, which acted as stress concentrators. Further work should be done in this area to see if the level of magnesium does indeed have a deleterious effect on the tensile strength of the composite. Efforts should also be made to minimise damage induced in the fibres during winding the preform.

The transverse strength of the Nicalon composites was greater than that for the corresponding Altex composites, although the presence of flaws makes comparison with theoretical calculations difficult. Improving the fibre spacing to eliminate touching fibres and voids is the key area for study in order to improve the transverse properties of the composites. In order to obtain better predictions for the longitudinal and transverse strengths the interfacial bond strength and toughness parameters should be measured in future studies.

Work should be carried out on the composite in the over-aged condition, as recent work has shown that the peak-aged condition is not always the best condition for the composite. Over-ageing the composite can lead to improved strength, compared with the peak-aged condition, and a higher level of ductility in the matrix.

Both Altex and Nicalon fibres have oxygen containing phases which react with the magnesium in the matrix. The oxycarbide constituent of the Nicalon fibre makes it

thermodynamically less stable than the Altex fibre. In order to reduce the chemical reactions and confer an element of toughness to the composites, work should be carried out on the use of coatings for these fibres. The Sigma monofilament does not contain oxygen and, if the problems associated with its manufacture can be overcome, this fibre may provide the greatest potential for a chemically stable reinforcement using the matrix alloys studied.

6.0 REFERENCES

(1) Ashby M. F., 'Criteria for selecting the components of composites', Proc. Metal Matrix Composites IV - Design & innovation (1993)pp2, The Institute of Materials, London.

(2) Brown A., 'Metal matrix composites on the road', Materials World, **1**(1) (1993) 20-21.

(3) Fukunaga H., 'Exploration of new application of MMCs manufactured by squeeze casting process', Proc. ICCM 9 (1993)pp355-362, Woodhead Publishing, Cambridge.

(4) Kelly A., 'Metal matrix composites - An overview, Cast reinforced metal composites', Proc. Int. Symp. on advances in cast reinforced metal composites (1988)pp1-5, Edited by Fishman S. G., Dhingra A. K., ASM International, Pennsylvania.

(5) Feest E. A., 'Metal matrix composites for industrial application', Materials & Design **7**(2) (1986) 58-64.

(6) Cantor B., 'Optimising microstructure in spray-formed and squeeze-cast metal-matrix composites', Journal of Microscopy **169**(2) (1993) 97-108.

(7) Ibrahim I. A., Mohamed F. A., Lavernia E. J., 'Particulate reinforced metal matrix composites - a review', J. Mater. Sci. **26** (1991) 1137-1156.

(8) Feest E. A., 'Exploitation of the metal matrix composites concept', Composite Materials **4**(5) (1988) 273-278.

(9) Chou T. W., Kelly A., Okura A., 'Fibre-reinforced metal-matrix composites', Composites **16**(3) (1985) 187-206.

(10) Chawla K. K., 'Metal matrix composites', chapter 4 in Materials Science and Technology, Vol.13: Structure and properties of composites, edited by Cahn, VCH Verlagsgesellschaft mbH, Weinheim, Germany (1993) 121 182.

(11) Harris S. J., 'Cast metal matrix composites', Mater. Sci. & Tech. **4**(3) (1988) 231-239.

(12) Harris S. J., 'Metal Matrix Composites', Comp. Sci. & Tech. **35** (1989) 99-103.

(13) Bader M. G., 'Reinforcing fibres: The strength behind composites', Materials World **1**(1) (1993)22-26.

(14) Bunsell A. R., Simon G., 'Ceramic fibres', Chapter 9, Fibre reinforcements for composite materials, Ed. A. R. Bunsell, Composite materials series Vol.2, Elsevier (1988) 427-478.

(15) Harris B., 'A perspective view of composite materials development', Materials & Design **12**(5) (1991)259-272.

(16) Kelly A., Rabotnov Y. N., 'Handbook of composites, Volume 1 - Strong fibres', North-Holland, Amsterdam (1985).

(17) Yajima S., Okumura K., Hayashi J., Omari M., 'Synthesis of continuous SiC fibers with high tensile strength', J. Am. Ceram. Soc. **59** (1976) 324-327.

(18) Altex data sheet, Sumitomo Chemicals, Japan.

(19) Yajima S., Hasegawa J., Hayashi J., Iimura M., 'Synthesis of continuous silicon carbide fibre with high tensile strength and high Young's modulus' J. Mater. Sci. **13** (1978)2569-2576.

(20) Hasegawa Y., Iimura M., Yajima S., Synthesis of continuous silicon carbide fibre, J. Mater. Sci. **15** (1980) 20-728.

(21) Hasegawa Y., Okamura K., 'Synthesis of continuous silicon carbide fibre', J. Mater. Sci. **18** (1983) 3633-3648.

(22) Hasegawa Y., Okamura K., 'Synthesis of continuous silicon carbide fibre', J. of Mater. Sci. **21** (1986) 321-328.

(23) Ichikawa H., Okamura K., Hasegawa Y., 'Synthesis of continuous silicon carbide fibre', J. Mater. Sci. **21** (1986) 4352-4358.

(24) Hasegawa Y., 'Synthesis of continuous silicon carbide fibre', J. Mater. Sci. **24** (1989) 1177-1190.

(25) Porte L., Sartre A., 'Evidence for a silicon oxycarbide phase in the Nicalon silicon carbide fibre', J. Mater. Sci. **24** (1989) 271-275.

(26) Laffon C., Flank A. M., Lagarde P., Laridjani M., Hagege R., Olry P., Cotteret J., Dixmier J., Miquel J. L., Hommel H., Legrand A. P., 'Study of Nicalon-based ceramic fibres and powders by EXAFS spectrometry, x-ray diffractometry and some additional methods', J. Mater. Sci. **24** (1989) 1503-1512.

(27) Schreck P., Vix-Guterl C., Ehrburger P., Lahaye J., 'Reactivity and molecular structure of silicon carbide fibres derived from polycarbosilanes', J. Mater. Sci. **27** (1992) 4237-4242.

(28) Maniette Y., Oberlin A., 'TEM characterisation of some crude or air heat-treated SiC Nicalon fibres', J. Mater. Sci. **24** (1989) 3361-3370.

(29) Pysher D. J., Goretta C., Hodder R. S., Tressler R. E., 'Strengths of ceramic fibers at elevated temperatures', J. Am. Ceram. Soc. **72**(2) (1989) 284-288.

(30) Mah T., Hecht N. L., McMullum D. E., Hoenigman J. R., Kim H. M., Katz A. P. Lipsitt H. A., 'Thermal stability of SiC fibres (Nicalon)', J. Mater. Sci. **19** (1984) 1191-1201.

(31) Simon G., Bunsell A. R., 'Mechanical and structural characterisation of the Nicalon silicon carbide fibre', J. Mater. Sci. **19** (1984) 3649-3657.

(32) Sawyer L. C., Arons R., Haimbach F., Jaffe M., Rappaport K. D., 'Characterisation of Nicalon: strength, structure, and fractography', Ceramic Engineering & Science Proc. (1985)pp567-575.

(33) Bleay S. M., Chapman A. R., Love G., Scott V. D., 'Electron probe microanalysis of Nicalon fibres', J. Mater. Sci. **27** (1992) 5389-5396.

(34) Scott V. D., Bleay S. M., Chapman A. R., Love G., 'Interface compatibility in Nicalon-fibre reinforced metal and ceramic composites', Journal of Microscopy **169**(2) (1993) 119-129.

(35) Warwick C. M., Smith J. E., 'Interfacial reactions in titanium alloys reinforced with C/TiB2- coated SiC Monofilament', Proc. 12th Risø Int. Symp. on Metal matrix composites - Processing, microstructure and properties (1991)pp735-740.

(36) Polmear I. J., 'Light alloys - Metallurgy of the light metals 2nd Ed.', Edward Arnold (1981), London 2nd Ed. (1989).

(37) Ahmed S., Gopinathan V., Ramakrishnan P., 'Squeeze casting and property evaluation of alumina fibre reinforced aluminium-silicon alloy matrix composites, Cast reinforced metal composites', Proc. Int. Symp. on advances in cast reinforced metal composites (1988)pp149-153, Edited by Fishman S. G., Dhingra A. K., ASM International, Pennsylvania.

(38) Shamsul J. B., Jomin N., Bushby R. S., Scott V. D., Fabrication, microstructure and ageing characteristics of aluminium alloy (6061) reinforced with Altex fibre, RAMM 94, Malaysia (1994) 289-298.

(39) Vietz J. T., Polmear I. J., 'The influence of small additions of silver on the ageing of aluminium alloys: Observations on Al-Cu-Mg alloys', J. Inst. Met. **94** (1966) 410-419.

(40) Taylor J. A., Parker B. A., Polmear I. J., 'Precipitation in Al-Cu-Mg-Ag casting alloy', Metal Science October (1978) 478-482.

(41) Chester R. J., Polmear I. J., 'TEM investigation of precipitates in Al-Cu-Mg-Ag and Al-Cu-Mg alloys', Micron **11** (1980) 311-312.

(42) Chester R. J., Polmear I. J., 'Relationships between microstructure and properties in the high-strength casting alloy 201', Proc 7th Int. Light Metals Congress, Aluminium -Verlag GmbH (1981)pp58.

(43) Kerry S., Scott V. D., 'Structure and orientation relationship of precipitates formed in Al-Cu-Mg-Ag alloys', Metal Science **18** (1984) 289-294.

(44) Polmear I. J., Couper M. J., 'Design and development of an experimental wrought aluminium alloy for use at evaluated temperature', Metall. Trans. **19A** (1988) 1027-1035.

(45) Auld J. H., 'Structure of metastable precipitate in some Al-Cu-Mg-Ag alloys', Mater. Sci. and Tech. **2** (1986) 784-787.

(46) Scott V. D., Kerry S., Trumper R. L., 'Nucleation and growth of precipitates in Al-Cu-Mg-Ag alloys', Mater. Sci. and Tech. **3** (1987) 827-835.

(47) Knowles K. M., Stobbs W. M., 'The structure of {111} age-hardening precipitates in Al-Cu-Mg-Ag alloys', Acta Cryst. **B44** (1988) 207-227.

(48) Muddle B. C., Polmear I. J., 'The precipitate Ω phase in Al-Cu-Mg-Ag alloys', Acta Metall. **37**(3) (1989) 777-789.

(49) Fonda R. W., Cassada W. A., Shiflet G. J., 'Accommodation of the misfit strain surrounding {111} precipitates (Ω) in Al-Cu-Mg-(Ag)', Acta Metall. Mater. **40**(11) (1992) 2539-2546.

(50) Garg A., Howe J. M., 'Convergent-beam electron diffraction analysis of the Ω phase in an Al-4.0Cu-0.5Mg-0.5Ag alloy', Acta Metall. Mater. **39**(8) (1991) 1939-1946.

(51) Garg A., Howe J. M., 'Grain-boundary precipitation in an Al-4.0Cu-0.5Mg-0.5Ag alloy', Acta Metall. Mater. **40**(9) (1992) 2451-2462.

(52) Chang Y. C., Howe J. M., 'Composition and stability of Ω phase in an Al-Cu-Mg-Ag alloy', Metall. Trans. **24A** (1993) 1461-1470.

(53) Hono K., Sano N., Babu S. S., Okano R., Sakurai T., 'Atom probe study of the precipitation process in Al-Cu-Mg-Ag alloys', Acta Metall. Mater. **41**(3) (1993) 829-838.

(54) Partridge P. G., Ward-Close C. M., 'Processing of advanced continuous fibre composites: Current practise and potential developments', International Materials reviews **38**(1) (1993) 1-24.

(55) Bushby R., Scott V. D., Trumper R. L., 'Diffusion bonding of fibre-reinforced aluminium', Proc. ECCM5, (1992)pp645, European Association for Composite Materials, Bordeaux.

(56) Mykura N., 'Liquid pressure forming of engineered metal matrix composites, Cast reinforced metal composites', Proc. Int. Symp. on advances in cast reinforced metal composites (1988)pp173-178, Edited by Fishman S. G., Dhingra A. K., ASM International, Pennsylvania.

(57) Zhu Z., 'A literature survey on fabrication methods of cast reinforced metal composites, Cast reinforced metal composites', Proc. Int. Symp. on advances in cast reinforced metal composites (1988)pp93-99, Edited by Fishman S. G., Dhingra A. K., ASM International, Pennsylvania.

(58) Cornie J. A., 'Advanced pressure infiltration casting technology produces near-absolute net-shape metal matrix composite components cost competitively', Mat. Tech. **10**(3/4) (1995) 43-58.

(59) Yang J., Chung D. D. L., 'Casting particulate and fibrous metal-matrix composites by vacuum infiltration of a liquid metal under an inert gas pressure', Proc. ICCM7 (1989)pp153-158, China, Pergamon Press, Beijing.

(60) Das A. A., Clegg A. J., Zantout B., Yakoub M. M., 'Solidification under pressure : Aluminium and Zinc alloys containing discontinuous SiC fibre', ibid. (1988) 139-47.

(61) Kang H. G., Zhang D. L., Cantor B., 'The microstructures of locally reinforced squeeze-cast Al-alloy metal-matrix composites', Journal of Microscopy **169**(2) (1993) 239-245.

(62) Lee G. G., Kim J., 'Mechanical behaviour of squeeze casted continuous SiC/Al composites', ICCM7 (1989)pp447-449, China, Pergamon Press, Beijing.

(63) Yamada S. I., Towata S. I., Ikuno H., 'Mechanical properties of aluminium alloys reinforced with continuous fibres and dispersoids, Cast reinforced metal composites', Proc. Int. Symp. on advances in cast reinforced metal composites (1988)pp109-114, Edited by Fishman S. G., Dhingra A. K., ASM International, Pennsylvania.

(64) Sample R. J., Bhagat R. B., Amateau M. F., 'High pressure squeeze casting of unidirectional graphite fibre reinforced aluminium matrix composites, Cast reinforced metal composites', Proc. Int. Symp. on advances in cast reinforced metal composites (1988)pp179, Edited by Fishman S. G., Dhingra A. K., ASM International, Pennsylvania.

(65) Fukunaga H., 'Squeeze casting processes for fibre reinforced metals and their mechanical properties, Cast reinforced metal composites', Proc. Int. Symp. on advances in cast reinforced metal composites (1988)pp101-107, Edited by Fishman S. G., Dhingra A. K., ASM International, Pennsylvania.

(66) Verma S. K., Dorcic J. L., 'Manufacturing of composites by squeeze casting, Cast reinforced metal composites', Proc. Int. Symp. on advances in cast reinforced metal composites (1988)pp115-125, Edited by Fishman S. G., Dhingra A. K., ASM International, Pennsylvania.

(67) Cook C. R., Yun D. I., Hunt W. H., 'System optimisation for squeeze cast composites, Cast reinforced metal composites', Proc. Int. Symp. on advances in cast reinforced metal composites (1988)pp195-204, Edited by Fishman S. G., Dhingra A. K., ASM International, Pennsylvania.

(68) Charbonnier J., Dermatker S., Santarini M., Fages J., Sabatie M., 'High performance metal-matrix components manufactured by squeeze-casting', Proc. Int. Symp. on advances in cast reinforced metal composites (1988)pp127, Edited by Fishman S. G., Dhingra A. K., ASM International, Pennsylvania.

(69) Taya M., Arsenault R. J., 'Metal matrix composites - Thermomechanical behaviour', Pergamon Press, Oxford (1989).

(70) Le Petitcorps Y., Stephonson T., Girot F., Naslain R., 'Chemical analysis and bonding at the fibre-matrix interface in model aluminium matrix composites, Cast reinforced metal composites', Proc. Int. Symp. on advances in cast reinforced metal composites (1988)pp67, Edited by Fishman S. G., Dhingra A. K., ASM International, Pennsylvania.

(71) Bader M. G., Clyne T. W., Cappleman G. R., Hubert P. A., 'The fabrication and properties of metal matrix composites based on aluminium alloy infiltrated alumina fibre preforms', Comp. Sci. & Tech. **23** (1985) 287-301.

(72) Quenisset J. M., Fedou R., Girot F., Le Petitcorps Y., 'Effect of squeeze casting conditions on infiltration of ceramic preforms, Cast reinforced metal composites', Proc. Int. Symp. on advances in cast reinforced metal composites (1988)pp133-138, Edited by Fishman S. G., Dhingra A. K., ASM International, Pennsylvania.

(73) Le Petitcorps Y., Leborgne G., Quenisset J. M., Barthole M., Stephenson T., Rouaux Y., Moore R., 'An overview of the damage effects related to the processing af aluminium matrix composites by liquid infiltration', Proc. ECCM5 (1992)pp657-663, European Association for Composite Materials, Bordeaux.

(74) Gungor M. N., Cornie J. A., Flemings M. C., 'Solidification processing of an aluminium/alumina composite, Cast reinforced metal composites', Proc. Int. Symp. on advances in cast reinforced metal composites (1988)pp39, Edited by Fishman S. G., Dhingra A. K., ASM International, Pennsylvania.

(75) Chiou J. M., Chung D. D. L., 'Characterisation of metal-matrix composites fabricated by vacuum infiltration of a liquid metal under an inert gas pressure', J. Mater. Sci. **26** (1991) 2583-2589.

(76) Lee H. I., Oh K. H., Kim T. S., Kim T. H., 'Precipitation characteristics of Sic Whisker reinforced Al-Cu and Al-Cu-Mg alloys', Proc. ICCM7 (1989)pp541-548, China, Pergamon Press, Beijing.

(77) Arsenault R. J., Taya M., 'Thermal residual stress in metal matrix composite', Acta Metall. **35**(3) (1987) 651-659.

(78) Dutta I., 'The nature and effect of thermal residual stresses in discontinuous fiber reinforced metal matrix composites', Comp. Sci. and Tech. 41(2) (1991) 193-213.

(79) Shetty D. K., 'Shear-lag analysis of fiber push-out (indentation) tests for estimating interfacial friction stress in ceramic-matrix composites', J. Am. Ceram. Soc. **71**(2) (1988) C-107-C-109.

(80) Phillips D. C., Sambell R. A. J., Bowen D. H., 'The mechanical properties of carbon fibre reinforced pyrex glass', J. Mater. Sci. **7** (1972) 1454-1464.

(81) Tennent R. M., 'Science data book', Oliver & Boyd, Edinburough (1987).

(82) Brown L. D., Maruyama B., Cheong Y. M., Rabenberg L. K., Marcus H. L., 'Metal matrix interfaces and their impact on the mechanical behaviour of composites', Composite Interfaces, Elsevier, London (1986) 27-35.

(83) Wang N., Wang Z., Weatherly G. C., 'Formation of magnesium aluminate (spinel) in cast SiC particulate-reinforced Al(A356) metal matrix composites', Metall. Trans. **23A** (1992) 1423-1430.

(84) Hallstedt B., Liu Z. K., Agren J., 'Fibre-matrix interactions during fabrication of Al_2O_3-Mg metal matrix composites', Mater. Sci. and Eng. **A129** (1990) 135-145.

(85) Levi C. G., Abbaschian G. J., Mehrabian R., 'Interface interactions during fabrication of aluminium alloy-alumina fiber composites', Metall. Trans. **9A** (1978) 697-711.

(86) Yang M., Scott V. D., 'Microstructural studies of aluminium-silicon alloy reinforced with alumina fibres', J. Mater. Sci. **26** (1991) 2245-2254.

(87) McLeod A. D., Gabryel C. M., 'Kinetics of the growth of spinel, $MgAl_2O_4$, on alumina particulate in aluminium alloys containing magnesium', Metall. Trans. **23A** (1992) 1279-1283.

(88) Hull D., 'An introduction to composite materials', Cambrindge University Press, Cambridge (1985).

(89) Harris B., 'Engineering composite materials', The Institute of Metals, London (1986).

(90) Phillips M. G., 'Simple geometrical models for Young's modulus of fibrous and particulate composites', Comp. Sci. and Tech. **43** (1992) 95-100.

(91) Kiess J. A., US Naval Research Laboratory Report NRL5752 (1962).

(92) Girardi M. A., 'Microstructure and properties of polyester/urethane acrylate thermosetting blends, and their use as composite matrices', J. Mater. Sci. **28** (1993) 3116-3124.

(93) Rice J. R., Wang J. S., 'Embrittlement of interfaces by solute segregation', Mater. Sci. and Eng. **A107** (1989) 23-40.

(94) Cooper G. A., Kelly A., 'Interfaces in composites', ASTM special technical publication 452, American Society for Testing and Evaluation, Philadelphia, PA. (1969) 90-106.

(95) Greszczuk L. B., Proc. 21st Annual Technical Conference, Plastics/Composites Institute, Society of the Plastics Industry, New York, (1966) Section 8A.

(96) Schulte K., 'The failure process in continuous fibre reinforced metal matrix composites', Proc. ICCM 9 (1993)pp603-609, Woodhead Publishing, Cambridge.

(97) Hu M. S., Yang J., Cao H. C., Evans A. G., Mehrabian R., 'The mechanical properties of Al alloys reinforced with continuous Al2O3 fibers', Acta Metall. Mater. **40**(9) (1992) 2315-2326.

(98) Vasudevan A. K., Doherty R. D., 'Aluminum alloys - Contemporary research and applications', Treatise on materials science and technology, Vol.31, Academic Press, Inc., London (1989).

(99) Yajima S., Okamura K., Matsuzawa T., Tanaka J., Hayase T., 'Continuous SiC fiber reinforced aluminum', Composite Materials, K. Kawata & T Akasaka, Ed., Proc. Japan-U.S. Conference, Tokyo (1981).

(100) Chen A. S., Bushby R. S., Phillips M. G., Scott V. D., 'A study of the mechanical properties and microstructure of fibre-reinforced aluminium alloy', Proc. R. Soc. Lond. A **450** (1995) 537-552.

(101) 'The properties of aluminium and its alloys', The Aluminium Federation, Birmingham (1983).

(102) Smallman R. E., 'Modern physical metallurgy, Fourth Edition', Butterworths, London (1988).

(103) Brown M. E., 'Introduction to thermal analysis- Techniques and applications', Chapman and Hall, London (1988).

(104) Guild F. J., Summerscales J., 'Microstructural image analysis applied to fibre composite materials: a review', Composites **24**(5) (1993) 383-393.

(105) Chandler J. A., 'Methods of analysis in the electron microscope', Proc. RMS (2) (1980) 117-122.

(106) Scott V. D., Love G., 'Quantitative electron-probe microanalysis', Ellis Horwood Limited, Chichester (1983).

(107) Goodhew P.J., Humphreys F. J., 'Electron microscopy and analysis, 2nd Edition', Taylor & Francis, London (1988).

(108) ASTM D3552, 'Standard test method for tensile properties of fiber-reinforced metal matrix composites'.

(109) Roebuck B., 'Code for practice of tensile test of particulate reinforced MMCs', NPL technical report (1993).

(110) BS EN 10 002-1, 'Tensile testing of metallic materials' (1990).

(111) Chen A. S., Smith J., Bushby R. S., Phillips M. G., Scott V. D., 'Tensile property evaluation of contiuous fibre MMC" Advanced Composite Letters **3**(3) (1994) 99-102.

(112) Hicks K. P., PhD Thesis, School of Materials Science, University of Bath (1994).

(113) Granger R. A., 'Fluid Mechanics', Holt, Rinehart & Winston, London (1985).

(114) Delannay F., Froyen L., Deruyttere A., 'Wetting of solids by liquid metals in relation to squeeze casting of MMCs, Cast reinforced metal composites', Proc. Int. Symp. on advances in cast reinforced metal composites(1988)pp81, Edited by Fishman S. G., Dhingra A. K., ASM International, Pennsylvania.

(115) Mortensen A., Michaud V. J., Cornie J. A., Flemings M. C., Masur L., 'Kinetics of fibre preform infiltration, Cast reinforced metal composites', Proc. Int. Symp. on advances in cast reinforced metal composites (1988)pp7, Edited by Fishman S. G., Dhingra A. K., ASM International, Pennsylvania.

(116) Do-Suck Han, Jones H., Atkinson H. V., 'The wettability of silicon carbide by liquid aluminium: the effect of free silicon in the carbide and of magnesium , silicon and copper alloy additions to the aluminium', J. Mater. Sci. **28** (1993) 2654-2658.

(117) Kang C. G., Yun K. S., 'The production of metal matrix composites by die casting processes and its mechanical properties', Proc. ICCM 9 (1993) pp739-746, Woodhead Publishing, Cambridge.

(118) Mortensen A., Cornie J. A., 'On the infiltration of metal matrix composites', Met. Trans. **18A** (1987) 1160-1163.

(119) Friend C. M., 'The effect of matrix properties on reinforcement in short alumina fibre-aluminium metal matrix composites', J. Mater. Sci. **22** (1987) 3005-3010.

(120) Mortensen A., Jin I., 'Solidification processing of metal matrix composites', International Materials Reviews **37**(31) (1992) 101-128.

(121) Scott V. D., Trumper R. L., Yang M., 'Interface microstructures in fibre-reinforced aluminium alloys', Comp. Sci. and Tech. **42**(1-3) (1991) 251-273.

(122) Cappleman G. R., Watts, Clyne T. W., 'The interface region in squeeze-infiltrated composites containing δ-alumina fibres in an aluminium matrix', J. Mater. Sci. **20** (1985) 2159-2168.

(123) Dahl N., Johnson T. E., 'The effect of magnesium and nickel as alloying elements in AlCu-SiC composites', Mater. Sci. and Eng., **A135** (1991) 151-155.

(124) Chapman A. R., PhD Thesis, School of Materials Science, University of Bath (1991).

(125) Birks N., Meier G. H., 'Introduction to high temperature oxidation of metals', Edward Arnold, London (1983).

(126) Coltters R. G., 'Thermodynamics of binary metallic carbides: A review', Mater. Sci. and Eng., **76** (1985) 1-50.

(127) Clyne T. W., Withers P. J., 'An introduction to metal matrix composites', Cambridge University Press (1993) 374.

(128) Cottu J. P., Couderc J. J., 'Thermal expansion stress in a metallic matrix composite: in situ TEM observations', J. Mater. Sci. **26** (1991) 2985-2990.

(129) Clyne T. W., Withers P. J., 'An introduction to metal matrix composites', Cambridge University Press (1993) 84.

(130) Decomps F., Gardaix N., Bader M. G., Barbedo de Magalhaes A., 'Heat treatment optimisation and improvement of tensile properties of fibre-reinforced aluminium alloys', Proc. ECCM5 (1992)pp723-728, European Association for Composite Materials, Bordeaux.

(131) 'Equilibrium diagrams of aluminium alloy systems', The Aluminium Development Association, London (1961).

(132) Hess P. D., Turnbull G. K., 'Effects of hydrogen on properties of aluminum alloys, Hydrogen in metals', Proc. International Conference on the Effects of Hydrogen on Materials, Properties and selection and structural design, Ed. Bernstein I. M., Thompson, A. W. (1974)pp277-287, Champion, New York.

(133) Pragnell P. B., Stobbs W. M., 'The effect of SiC particulate reinforcement on the ageing behaviour of aluminium based matrix alloys', Proc. ICCM7 (1989)pp573-578, China, Pergamon Press, Beijing.

(134) Cottu J. P., Couderc J. J., Viguier B., Bernard L., 'Influence of SiC reinforcement on precipitation and hardening of a metal matrix composite', J. Mater. Sci. **27** (1992) 3068-3074.

(135) Abis S., Donzelli G., 'Effect of reinforcements on the ageing process of an Al-Cu/SiO2Al2O3 metal matrix composite', J. Mater. Sci. Lett. **7** (1988) 51-52.

(136) Hadianfard M. J., Yiu-Wing Mai, Healy J. C., 'Effect of ceramic reinforcement on the ageing behaviour of an aluminium allloy', J. Mater. Sci. **28** (1993) 3665-3669.

(137) Johnston W. D., Greenfiled I. G., 'Effect of magnesium concentration on the shear strength of alpha-alumina/aluminium composites', Cast reinforced metal composites, Proc. Int. Symp. on advances in cast reinforced metal composites (1988)pp335-340, Edited by Fishman S. G., Dhingra A. K., ASM International, Pennsylvania.

(138) Piggot M. R., 'Load bearing fibre composites', Pergamon, Oxford (1980) 199-200.

(139) Chen A. S., Bushby R. S., Scott V. D., 'Tensile property evaluation of continuous fibre-reinforced aluminium alloy', Proc. ICCM 10 (1995)ppII-497-504, Woodhead Publishing Limited, Cambridge.

(140) Withers P. J., Stobbs W. M., Pedersen O. B., 'The application of Eshelby method of internal stress determination of short fibre metal matrix composites', Acta Metall. **37** (1989) 3061-3084.

(141) Chapman A. R., Bleay S. M., Scott V. D., 'Influence of microstructure on the strength of Nicalon-reinforced aluminium metal-matrix composites', J. Mater. Sci. **29** (1994) 4523-4534.

(142) Ochiai S., Osamura K., 'Influences of matrix ductility, interfacial bonding strength, and fiber volume fraction on tensile strength of unidirectional metal matrix composites', Metall. Trans. **21A** (1990) 971-977.

(143) Kuroki Y., Kuroda T., Yunoki N., Tanaka T., 'Effect of casting parameters on the mechanical properties of aluminum alloy matrix composites fabricated by the LPF method', Proc. ICCM 10 (1995)ppII-11-18, Woodhead Publishing Limited, Cambridge.

(144) Zabolotsky A. A., 'Structure and properties formation of metal matrix composites', Comp. Sci. and Tech. **45** (1992) 233-240.

(145) Böhm H. J., Rammerstorfer F. G., 'Micromechanical investigation of the processing and loading of fibre-reinforced metal matrix composites', Mater. Sci. and Eng. **A135** (1991) 185-188.

(146) Bushby R. S., Scott V. D., Ibbotson A. R., Lindsay N. J., 'Manufacture and evaluation of carbon fibre reinforced aluminium alloy', Proc. ICCM 10 (1995)ppII-3-10, Woodhead Publishing Limited, Cambridge.

APPENDIX

Electron-Probe Microanalysis (EPMA)

X-ray generation

X-rays can be generated from a specimen by focusing a small electron probe onto its surface. The volume from which x-rays are generated is about $1\mu m^3$. Each element has its own x-ray spectrum, and so the elements present in a given material can be identified by the analysis of these characteristic x-rays. The analysis involves the accurate measurement of the x-ray wavelengths (or energies) and intensities. Two methods are employed:

Wavelength Dispersive Spectroscopy (WDS)

This method utilises an x-ray spectrometer, in which the x-ray emission is dispersed by an analysing crystal via Bragg diffraction from its crystal lattice planes. Thus for a crystal of known d spacing x-rays will be diffracted by the angle θ, such that the Bragg equation is satisfied.

$$n\lambda = 2d\sin\theta$$

where n is an integer, λ is the wavelength, d the lattice spacing, and θ the Bragg angle. Therefore different wavelengths and hence different elements can be selected by varying θ. The wavelength for carbon is 44 Å, and the wavelength for copper is 1.5 Å, a difference of 30x, therefore a range of analysing crystals are required to cover a range of wavelengths. Commonly used crystals are LiF, PET and TAP. A gas flow proportional counter is commonly used to record the intensity of the diffracted x-rays.

WDS has good spectral resolution and high sensitivity, and can measure down to light elements such as Be (Z=4), but can only measure one particular x-ray wavelength at a time.

Energy Dispersive Spectroscopy (EDS)

ED systems use a solid state (Li-drifted silicon) detector which produces a voltage pulse proportional to the x-ray energy. An x-ray enters through a thin berylium window in the detector, and produces electron hole pairs in the Si-Li. The charge produced by a typical x-ray can then be amplified to give a measure of the energy of the incident x-ray. The data is collected using a multi-channel analyser, such that all the elements (down to C, Z=6) present can be displayed at once as a function of intensity versus energy.

The advantages of this system are:

(1) speed of analysis

(2) good collection efficiency

(3) insensitive to specimen geometry

(4) qualitative analysis

EDS can also show the whole spectrum at the same time, whereas WDS does one element after another.

Quantitative data

To obtain quantitative data the measured intensity of a particular characteristic x-ray line from the spectrum is compared with that from a reference standard of known composition. Electron and x-ray behaviour is different in the specimen and the standard and so a number of correction factors must be considered.

Z, Atomic Number Correction

Electrons loose energy when they enter a target due to interactions with the constituent atoms. In addition to being dependent upon electron energy, the rate of energy loss is a function of the mean atomic number of the material. Hence differences in behaviour between the specimen and the standard.

A, Absorption Correction

The absorption of x-rays can occur by a number of processes:

Compton scattering, in which the x-ray energy is reduced by an inelastic collision with an atom.

Rayleigh scattering, where there is no exchange of energy with the atom.

The photoelastic effect, where the x-ray photon is completely absorbed by the atom and an electron is ejected.

F, Fluorescence

The x-rays may produce secondary x-rays from within the target as well as primary x-rays produced directly by the electron beam. The x-ray spectrometer cannot distinguish between the primary and secondary x-rays of the same energy, and so misleading results may arise.